Investigating Metabolism-Based Pharmacologic and Dietary Strategies of Nutrient

Restriction to Impact Health and Disease

by

Annamarie Elizabeth Allen

Department of Pharmacology and Cancer Biology
Duke University

Date:_____

Approved:

_____

Jason Locasale, Supervisor

_____

Cynthia Kuhn

_____

Matthew Hirschey

_____

Christopher Newgard

_____

Nancie MacIver

Dissertation submitted in partial fulfillment of
the requirements for the degree of Doctor
of Philosophy in the Department of
Pharmacology and Cancer Biology in the Graduate School
of Duke University

2022

ABSTRACT

Investigating Metabolism-Based Pharmacologic and Dietary Strategies of Nutrient

Restriction to Impact Health and Disease

by

Annamarie Elizabeth Allen

Department of Pharmacology and Cancer Biology
Duke University

Date:_____
Approved:

_____

Jason Locasale, Supervisor

_____

Cynthia Kuhn

_____

Matthew Hirschey

_____

Nancie MacIver

An abstract of a dissertation submitted in partial
fulfillment of the requirements for the degree
of Doctor of Philosophy in the Department of
Pharmacology and Cancer Biology in the Graduate School of
Duke University

2022

Abstract

Metabolism is essential for life and is involved in disease. By studying metabolism, we can understand basic cellular and organismal physiology, and try to modulate metabolism to treat diseases where it is implicated. Nutrient restriction, through both pharmacologic and dietary methods, is one way metabolism can be modulated because nutrients feed metabolism. In this dissertation, I examine both pharmacologic and dietary strategies of limiting different nutrients, and the impact on metabolism, physiology, and on models of disease. I use different model systems including mammalian cell culture, flies, and mice and examine their overall health and/or growth under different types of nutrient restriction. I examine metabolism using a liquid chromatography-mass spectrometry-based metabolomics method, which allows the simultaneous measurement of the relative levels of hundreds of polar and semi-polar metabolites. By using pharmacologic inhibitors that target glycolysis and connected pathways, my colleagues and I found that cancer cell viability and growth are reduced and showed how these metabolic pathways are used to benefit cancer growth. I also used pharmacologic and dietary strategies to target cysteine metabolism and found an unexpected connection with altered nucleotide metabolism when cysteine was limited in cancer cells and flies. Finally, I examined the impact of restrictive diets in mice, and my preliminary findings show that glucose metabolism is altered in these

mice. This work collectively shows how metabolism can be altered by different methods

of nutrient restriction, and how these strategies could be useful for treating diseases like

cancer and promoting health and longevity.

Dedication

To my husband Jeff,

And my daughter Lila

Contents

List of Tables

List of Figures

Acknowledgements

First and foremost, I would like to express my gratitude to my PhD advisor, Dr. Jason Locasale. Jason has exposed me to so many interesting scientific projects and ideas throughout my time working for him that I otherwise never would have encountered. He has changed the way I think about metabolism and approach science and made me laugh a lot through the long process of completing a PhD. Without Jason's mentorship, I never would have gotten to this point in my PhD, as he encouraged me and stopped me from doubting myself. I would also like to thank my committee members, Dr. Matthew Hirschey, Dr. Cynthia Kuhn, Dr. Nancie MacIver, and Dr. Christopher Newgard, who were also instrumental in my success, providing invaluable feedback on my work and encouragement. Additionally, I am very thankful for Dr. David Kirsch, who served as my co-mentor for my training grant and allowed me to learn mouse work in his lab.

Throughout my PhD, I also worked with and received mentorship from several outstanding colleagues in the Locasale Lab and Kirsch Lab. I worked with Michael Reid and Maria Liberti extensively in my first year, and I am incredibly grateful for the many hours they spent training me and their welcoming and patient attitude towards me as I learned. I am also grateful for the time Daniel Cooper spent teaching me mouse surgery techniques, and all the times Juan Lui was available for mass spec troubleshooting and advice. I especially want to thank Ziwei Dai, who was not only a mentor but also a great

I am also incredibly grateful for the love and support my friends and family has given me throughout my PhD. I would not have gotten to this point without my amazing parents, who supported my education before I came to Duke and helped me move and transition to life in North Carolina and who have remained incredibly

supportive since. I am additionally grateful for my best friend Taylor, who always kept

my spirits up through countless hours spent on phone and zoom calls, and who seemed

to believe in me more than I believed in myself.

Finally, the person who I need to thank most for their support though all the

highs and lows I went through as I worked towards my PhD, is my husband Jeff. You

were the first person I came to with my joy and my frustration. You encouraged me in

every way possible, and I mean it when I say that I couldn't have done it without you. I

am so looking forward to the next chapter of our lives that we now get to build together.

1. Introduction

1.1 Overview of Metabolism and Nutrition

Metabolism is the set of chemical reactions within living organisms that build

and break down molecules to sustain life. Metabolism serves three main purposes:

energy generation, breaking down large and complex molecules into smaller and

simpler molecules (catabolism), and building up small and simple molecules into larger

and more complex ones (anabolism). Energy is required for life because according to the

second law of thermodynamics, entropy, or randomness, cannot decrease without the

input of energy. Living organisms are highly ordered and are constantly combatting

entropy, for example using energy to pump sodium ions against their concentration

gradient out of cells. All energy-generating metabolic pathways are catabolic, but

catabolism also serves a separate purpose of breaking down large molecules such as

polysaccharides, lipids, proteins, and nucleic acids into smaller and simpler molecules

such as monosaccharides, fatty acids, amino acids, and nucleotides, which can then be

used as building blocks for anabolic metabolism or excreted. Anabolism creates the

molecules that constitute all cellular structures such as DNA, proteins, lipid membranes,

and can be used to store energy in large molecules such as glycogen. It is also now

recognized that metabolism can serve purposes outside of these three main functions by

generating metabolites which affect cellular signaling and gene transcription.

Metabolism plays a large or small role in every biological process, and therefore

understanding metabolism allows us to not only understand basic biology, but also to devise ways in which biological systems can be manipulated through metabolism to serve human interests such as improving health and treating diseases.

Metabolism and nutrition are essentially intertwined. Metabolism could not function without an input of molecular material to act on. Nutrients are the molecules that are consumed by cells and organisms which feed into metabolic pathways and sustain life, growth, and specialized biological functions. Nutrients are divided into two categories: micronutrients and macronutrients. Micronutrients are nutrients including vitamins and minerals which are required in relatively small quantities compared to macronutrients. The purpose of micronutrients is not to provide organisms with energy or large quantities of material to feed into many different anabolic pathways. Most micronutrients either act as metabolic coenzymes or cofactors, act as a specialized metabolic precursor that cannot be synthesized by the organism, or in the case of minerals such as sodium or potassium, are required for ion homeostasis and signaling. Macronutrients are divided into three classes: carbohydrates, proteins, and lipids, and are, by contrast, are used for energy generation and biomass production. Overall, adequate intake of macro- and micronutrients is important for health. However, there are circumstances in which restricting certain nutrients can be beneficial for promoting health or treating disease.

1.2 Nutrient Restriction

Nutrient restriction can have a large impact on metabolism, which can then affect cellular and whole-body physiology and health. This will be discussed more in the subsequent subsections. Nutrients can be restricted through dietary and pharmacologic methods, among others. Dietary nutrient restriction simply involves depleting the nutrient of interest or its precursor in the food or media of an organism. Pharmacologic nutrient restriction can be achieved by using chemical agents to blockade nutrient transporters, increase nutrient excretion, or inhibit metabolic enzymes to limit nutrient metabolism. Pharmacologic nutrient restriction has benefits in clinical settings, where prescribed dietary nutrient restriction may be hard to adhere to as opposed to a prescribed pill. Pharmacologic nutrient restriction can also have more specific effects than dietary, as inhibitors can be designed to target a specific metabolic pathway downstream of a nutrient that feeds many different metabolic pathways. Dietary methods of nutrient restriction also have advantages in certain situations. Sometimes pharmacologic methods for nutrient restriction are not available, could have off-target effects, or could cause safety issues by restricting a nutrient and its metabolism too much. Additionally, there are circumstances in which one may want to simultaneously alter the many metabolic pathways a nutrient feeds into, and therefore the lack of specificity when using dietary restriction could be advantageous. This dissertation

discusses uses of both dietary and pharmacologic-based nutrient restriction and their effects on metabolism, health, and on diseases such as cancer.

1.3 Cancer

Cancer is a disease of uncontrolled cell proliferation, and cancer cells exhibit unique metabolic alterations and increased nutrient uptake to satisfy the biosynthetic, bioenergetic, and signaling demands of uncontrolled growth. Metabolic inhibitors and nutrient restriction can deprive cancer cells of some of the molecular building blocks needed for cellular replication and rewire metabolism to inhibit growth or promote cell death. The limitation of many different nutrients and their metabolism have been studied as anti-cancer strategies, a selection of which will be further discussed.

1.3.1 Glucose and The Warburg Effect

Almost a century ago Otto Warburg made the discovery that tumors take up significantly more glucose than normal non-proliferating tissues[1]. He also noted that tumors convert much of the glucose to lactate whereas normal cells completely oxidize glucose to carbon dioxide in the presence of oxygen and functional mitochondria. This phenomenon has been termed the 'Warburg Effect'. That cancers tend to utilize Warburg Effect (WE) to metabolize glucose is paradoxical because most of the lactate that is produced is secreted from the cell, which precludes the glucose-derived carbons from being used for biosynthesis. Additionally, during WE cells produce approximately 90% less ATP per molecule of glucose compared to what could be generated if glucose

were completely oxidized to carbon dioxide in mitochondria. Warburg later

hypothesized that defective mitochondria gave rise to this phenomenon[2], but it is known

that cancers cells do in fact have functional mitochondria and even cancers that display

WE still use respiration to varying extents[3]. Proposed functions for the WE include more

rapid (although less efficient) ATP synthesis, promotion of biosynthesis through NAD+

regeneration and glucose flux into biosynthetic pathways, generation of a favorable

tumor microenvironment through lactate-mediated acidification and signaling functions

through altered redox homeostasis or altered histone acetylation [4,5]. While the

advantages the WE are still debated, the strategy of targeting WE and glucose

metabolism through dietary or pharmacologic methods as the basis of cancer prevention

and treatment strategies has shown promise.

1.3.1.1 Pharmacologic Warburg Effect Targets

Pharmacologically, glucose transporters and several glycolytic enzymes have

been seen as potential anti-WE drug targets. The glucose transporter GLUT1 is

overexpressed in many cancers[6], and there are a number of compounds which can

inhibit it either directly or indirectly[7,8]. The HK2 isoform of hexokinase, which catalyzes

the first step of glycolysis, has been of interest due to its lack of expression in most non-

cancer cells, but its structural similarity with the HK1 isoform makes it difficult to

target[9]. The pyruvate kinase M isozymes PKM1 and PKM2, which catalyze the last step

of glycolysis, have also been studied as potential anti-cancer targets[10]. However, it is

unclear how to best target this step of the pathway to block WE and achieve anti-cancer effects, as there have been conflicting reports as to which isozyme benefits cancers[11]. Previous studies have shown that PKM2, the less active isozyme, was beneficial to cancer growth by promoting anabolic metabolism and WE[12-14], but a more recent study showed that PKM1expression favors cancer growth, WE, and anabolic metabolism[15].

Previous work done by my colleagues has established that pharmacologically targeting a different glycolytic enzyme, glyceraldehyde 3-phosphate dehydrogenase (GAPDH), which catalyzes the sixth step of glycolysis, can be a selective way of targeting the WE and cancers that display high WE. Their work showed that the GAPDH step serves as a bottleneck and controls flux through glycolysis and lactate production more than any other glycolytic enzyme when the levels of upper glycolytic intermediates are high[16]. Subsequent work confirmed that GAPDH exerts different regulatory control over glycolysis depending on the state of glycolysis and showed that inhibition of GAPDH reduces glycolytic flux more in cells displaying high WE than in those with low WE[17], suggesting that GAPDH inhibitors could be selective cancer therapies. This study also showed that a natural product, koningic acid (KA), acts as a selective GAPDH inhibitor, selectively kills high-WE cancer cells, and reduces tumor growth in mice at tolerable doses. These studies show that pharmacologically targeting WE through GAPDH inhibition could be a viable treatment option in some cancers.

1.3.1.2 Targeting Warburg Effect and Glucose Metabolism through Diet[i]

Dietary strategies that seek to limit WE and glucose metabolism have also been explored with some success. In general, the goal of diets that target WE and glucose metabolism in cancer is to lower blood glucose levels, thus depriving cancer cells of glucose and limiting its metabolism. However, diets that lower blood glucose also elicit a host of other beneficial anti-cancer effects such as altered hormone levels and signaling[18]. These diets also affect more metabolic pathways than just glycolysis, which can also play a role in the anti-cancer effect of the diet. This lack of specificity can make it difficult to study how one physiological effect of the diet, such as altered glucose metabolism, affects cancer, but therapeutically, the combination of these many physiological and metabolic effects is partially what makes dietary strategies against cancer so appealing. Calorie restriction and ketogenic diets are the two best-studied diets which can affect glucose metabolism, which will be further discussed.

1.3.1.2.1 Calorie Restriction and Cancer

Calorie restriction (CR) is a dietary strategy which involves reducing the overall caloric intake of an organism by approximately 20-50% without inducing malnutrition. CR has been shown to extend lifespan and delay the onset of age-related diseases, including cancer. This phenomenon has been widely studied in rodents and the anti-

---

[i] This chapter subsection was partially adapted and modified from a published review: Bose S, Allen A.E, and Locasale J.W. "The Molecular Link from Diet to Cancer Cell Metabolism". *Molecular Cell* (2020). This text was reproduced in accordance with the CC-BY license. All text included in this section was originally written by A.E.A.

cancer and longevity-promoting effects of CR appear to be conserved across species ranging from worms to non-human primates[19,20]. Numerous animal studies show that CR can prevent many cancers, as well as restrict progression and metastasis[21]. These positive effects have been shown in cancers from diverse tissues including mammary, lung, prostate, brain, bladder, pancreatic, hepatic, skin, colorectal, and ovarian[21,22]. Calorie restriction lowers blood glucose levels, which can limit glycolysis through reduced glucose availability and by reducing circulating insulin and bioavailable insulin-like growth factor-1 (IGF-1) levels[23]. Insulin and IGF-1 activate proliferative signaling pathways which increase glucose metabolism[23,24]. In addition to its effects on glucose metabolism and proliferative signaling, CR has been shown to have antiangiogenic and proapoptotic effects on tumors in mice, as well as systemic anti-inflammatory effects[24], slow basal metabolic rate[25], and to alter other metabolic pathways including fatty acid metabolism[26], the carnitine shuttle pathway, sphingosine metabolism, and methionine metabolism[27]. Calorie restriction can therefore impact cancer growth through multiple mechanisms including altered glucose metabolism.

1.3.1.2.2 Ketogenic Diet and Cancer

Ketogenic diet (KD) is another dietary strategy that has been studied as a potential way to reduce WE metabolism and cancer growth. The classical ketogenic diet is used to treat epilepsy and is defined as a "high-fat, moderate-protein, low-carbohydrate diet", with a specified 4:1 or 3:1 weight ratio of fat to combined protein

and carbohydrates[28]. Ketogenic diets result in lower blood glucose levels which leads to ketosis involving reduced glycolysis and increased β-oxidation[29]. The production of ketone bodies from fatty acids in the liver provides energy-producing substrates for the brain and other organs. This causes a number of effects on central carbon metabolism including altered glucose and central carbon metabolism which tumors are known to require[4,30,31]. Additionally, some cancers have lower expression of ketone-metabolizing enzymes, suggesting that these cancers could be highly sensitive to KD[23,32,33]. Ketogenic diets have also been hypothesized to work through mechanisms similar to those postulated in caloric restriction, including reducing anabolic hormones like IGF-1 and insulin and increasing oxidative stress in tumors[30,34]. However, there is less evidence that KD is effective at treating or preventing cancer than there is for CR. Mouse studies on ketogenic diets as interventions in xenograft models have shown mixed results, with some reports of reduced tumor growth[35,36], others showing effects on tumor growth in combination with chemotherapy or radiotherapy[37], and others reporting no benefit of KD[38]. It should be noted that these studies have considerable differences in the macronutrient compositions of their control and ketogenic diets, and in most of these studies, protein intake was lower in KD groups. Because protein intake has been shown to influence cancer[39], this is a major confounding factor. However, two of these studies kept protein intake consistent between groups and still saw a beneficial effect of KD and low-carbohydrate diets in prostate cancer xenograft models[35], suggesting low-

carbohydrate or ketogenic diets could be beneficial in some cancer settings. It is known

that tumors can vary widely as to their dependence on glucose metabolism[17]. However,

it is unknown whether a tumor's preference for glucose metabolism predicts its

responsiveness to diets that alter blood glucose levels. Currently there is no rigorous

evidence that low-carbohydrate or ketogenic diets decrease cancer incidence or improve

outcomes in humans[40] but much remains to be studied.

1.3.2 Methionine and Cancer

Methionine is an essential sulfur-containing amino acid involved in numerous

biological processes including modulation of gene expression through chromatin and

nucleic acid methylation, polyamine biosynthesis, nucleotide biosynthesis, and redox

balance, among others[41]. Most of these biological processes can be altered or upregulated

to benefit cancer growth in some way, which requires increased methionine uptake and

metabolism[42-45]. In fact, increased tumor methionine uptake has shown considerable

clinical prognostic utility through measuring L-[methyl-11C] methionine (MET)

uptake[46,47].

Dietary and pharmacologic strategies have been tested to exploit altered

methionine metabolism in cancer. Dietary methionine restriction has shown efficacy in

reducing tumor growth and sensitizing tumors to radiation and chemotherapy in

numerous and diverse rodent cancer models[48-53], and in suppressing metastasis in a

triple negative breast cancer xenograft mouse model[54]. Dietary methionine restriction

can also be achieved in humans and are well tolerated over a 3-week period with no

significant side effects in healthy individuals[53]. However, a restrictive diet must be used

to achieve dietary methionine restriction in humans[41,53], and therefore pharmacological

methods of targeting methionine may be more feasible clinically. A methionine

analogue, ethionine, was tested and showed preclinical efficacy[55], but ultimately found

to be toxic. Administration of an enzyme that degrades methionine, methioninase and

its more stable recombinant form rMETase, has shown preclinical anti-cancer efficacy in

various mouse models[56-59], and phase I clinical trials have shown its ability to lower

serum methionine levels without toxicity[60-62]. Inhibitors have also been developed for the

enzyme MAT2A[63-65], which converts methionine to the universal methyl donor S-

adenosyl- methionine (SAM). One of these inhibitors has moved into phase I clinical

trials with initial positive results [66]. Other approaches have been to target downstream

processes that methionine metabolism feeds, such as polyamine metabolism[41].

1.3.3 Cysteine and Cancer[ii]

Cysteine is the other major sulfur-containing amino acid and can be synthesized

from methionine via the transsulfuration pathway[67] or taken up in its oxidized form

cystine via the system x_c^- amino acid antiporter. However, many cancer cells cannot

meet their requirements for cysteine through the transsulfuration pathway[68], and certain

---

[ii] This chapter subsection was partially adapted and modified from a published review: Bose S, Allen A.E, and Locasale J.W. "The Molecular Link from Diet to Cancer Cell Metabolism". *Molecular Cell* (2020). This text was reproduced in accordance with the CC-BY license. All text included in this section was originally written by A.E.A.

cancers have been shown increased reliance on the system x_c^- transporter[69-72]. Cysteine is limiting for glutathione production and therefore critical for cellular redox homeostasis[73,74]. Intracellular cysteine depletion can lead to an oxidative, iron-dependent form of non-apoptotic cell death termed ferroptosis[75], which is discussed in more detail in Section 1.5. Cancer cells often have higher basal levels of reactive oxygen species generation and can display increased iron uptake, therefore it has been proposed that pharmacological induction of ferroptosis could be a selective strategy to treat cancer[76]. Although interesting, it remains for future study to investigate whether dietary strategies such as cysteine/cystine limitation, alterations in antioxidant consumption, or iron supplementation could influence tumor responsiveness to ferroptosis and redox processes[77,78].

Several inhibitors for system x_c^- exist and are being explored for use in cancer treatment. Sulfasalazine is a system x_c^- inhibitor that is already used clinically for treatment of arthritis and shows efficacy in several preclinical cancer models[79-81]. Erastin and its analogs also target system x_c^- and have also shown preclinical efficacy against a range of cancer types[76,82-84]. Erastin treatment can also enhance the effectiveness of chemotherapy and radiotherapy[85-90]. A different approach to target cysteine metabolism in cancer involves the administration of a cysteine and cystine-degrading enzyme. This cyst(e)inase enzyme was capable of reducing the growth of breast and prostate cancer xenografts and doubled the survival of mice in a chronic lymphocytic leukemia model[91].

Pharmacological strategies which bypass cysteine metabolism and lead to ferroptosis through other means are also being explored[76].

1.3.4 Serine and Cancer

Serine is a nonessential amino acid which can be up taken through several amino acid transporters or synthesized *de novo* from glucose through the serine synthesis pathway. Serine metabolism is critically important to a number of cellular processes which are often dysregulated in cancer in order to increase survival and cell growth[92]. Through the folate cycle, serine donates one-carbon units which are used for nucleotide synthesis and to generate reducing power in the form of NADPH and NADH[93]. Serine is converted to glycine through this process, and along with methionine is used for cysteine production through the transsulfuration pathway, which can impact glutathione levels. The folate cycle also interfaces with methionine metabolism, allowing regeneration of methionine from S-adenosyl-homocysteine through carbon donation. Together, the folate cycle and methionine metabolism are defined as a larger metabolic pathway called one-carbon metabolism, which can be thought of as a metabolic integrator of nutrient status, impacting lipid, nucleotide, and protein biosynthesis, redox status, and epigenetics[93].

Dietary serine and glycine restriction, inhibition of the serine synthesis pathway, and interfering with metabolic pathways downstream of serine are all ways altered serine metabolism can be targeted in cancer. In fact, inhibitors of folate metabolism

("antifolates" such as methotrexate) and nucleotide synthesis inhibitors are some of the oldest cancer therapies and are still used today[94,95]. While circulating serine levels can be maintained to some extent by synthesis in the liver and other organs[92,96], dietary serine and glycine restriction can effectively lower the circulating levels of these amino acids by about 50%[97,98] and shows success in reducing tumor growth in various mouse models[98-101]. However, dietary serine restriction may be limited in its effectiveness, as many cancers can adapt to exogenous serine limitation by increasing *de novo* serine synthesis through the serine synthesis pathway[92,98,101], and certain cancers amplify or increase expression of the enzyme phosphoglycerate dehydrogenase (PHGDH)[102-106], which routes carbon from glycolysis into serine synthesis. Inhibitors of PHGDH have been developed and show anti-cancer activity *in vitro* and *in vivo*[107-109]. Interestingly, cancers that overexpress PHGDH still respond to its inhibition in the presence of abundant exogenous serine[103,105,109,110], which has prompted investigation as to why these cancers are so reliant on the serine synthesis pathway[92].

1.4 Diet and Aging

1.4.1 Calorie Restriction

In addition to its effects on cancer, calorie restriction is the best-studied and most rigorously documented intervention to extend lifespan. This effect was first described in the 1930s by McCay and colleagues, who showed that restricting calories without inducing malnutrition in rats prolonged mean and maximal lifespan[111,112]. Since then,

14

lifespan extension through CR has been shown in numerous and taxonomically diverse

species including yeast, worms, fish, and mice[19,113,114]. In mice, CR prevents or delays

many age-related diseases including type 2 diabetes, cancer, nephropathies,

cardiomyopathy, and neurodegeneration[115]. Additionally, the effects of CR in non-

human primates have been investigated in three separate studies of rhesus monkeys.

The overall results from these studies show decreases in age-related diseases in CR

monkeys, and two of the studies also found increased survival in CR monkeys[20,116-120].

Natural experiments and observational studies in humans offer some evidence that the

beneficial effects of CR are conserved in humans[121]. This is further supported by

randomized controlled trials of calorie restriction which show similar CR-induced

metabolic and physiological changes that have been observed and mechanistically

linked to the beneficial effects of CR in animal studies[121,122]. These alterations include

reductions in energy expenditure and basal metabolic rate, reduced levels of circulating

insulin, IGF-1, leptin, thyroid hormones, decreased body temperature, improved

mitochondrial efficiency and reduced oxidative stress, reduced inflammation, increased

autophagy, changes in multiple signaling pathways, reduced blood glucose levels, and

changes in several metabolic pathways including those discussed in Section 1.3.1.2[122-128].

1.4.2 Protein Restriction

It has been argued that in some species, the effects of calorie restriction are due to

reductions in specific nutrients including protein and certain amino acids as opposed to

overall calorie reduction[129-132]. Protein restriction shows many of the same beneficial effects as calorie restriction including improvements in health and longevity in animal models[133-136]. There is also evidence that this effect is conserved in humans, with one study finding that 50-65-year-old American men and women who reported higher protein intake had significantly higher risks of all-cause and cancer mortality, but the trend was reversed for those over age 65, indicating that higher dietary protein levels may promote cancer and mortality in middle age, but be protective in old age[39]. Interestingly, this effect was significantly reduced or eliminated for respondents whose main source of protein came from plant rather than animal sources, which can have markedly different amino acid content. Another study examining over 100,000 American men and women found similar results, with animal protein intake increasing the risk of cardiovascular mortality, and increased plant protein intake reducing the risk of all-cause mortality[137], and a similar trend was also found in a Japanese cohort[138]. Possible mechanisms for the health-promoting effects of a low-protein diet include reduced mechanistic target of rapamycin complex1 (mTORC1) signaling, increased circulating fibroblast growth factor 21 (FGF21) levels, decreased growth hormone (GH) and IGF-1 signaling, increased autophagy, reduced oxidative stress, and lower methionine and branched chain amino acid levels, lower intake of which are independently associated with health and longevity[133,134,139-141].

1.4.3 Methionine Restriction

Restriction of a single amino acid, methionine, can increase lifespan independent of calorie consumption. This effect was first demonstrated in Fischer 344 rats, where the reduction of dietary methionine from 0.86 to 0.17% resulted in a 30% longer lifespan[142]. Lifespan-prolonging effects of restricted dietary methionine (MR), have since been demonstrated in most major model organisms, including yeast, worms, flies, and rodents[143]. Human studies on this effect are limited, but show that MR causes in increase in fat oxidation in obese adults[144], that long-term, high dietary methionine intake was associated with an increased risk of acute coronary events in middle-aged Finnish men[145], and that fasting plasma concentrations of SAM was positively correlated with adiposity, fasting insulin, homeostasis model assessment of insulin resistance (HOMA-IR), and tumour necrosis factor-α[146]. As previously noted, many of the detrimental effects of a high-protein diet are eliminated if plant-based protein rather than animal is consumed. Methionine is lower in plant-based protein[41,147], and this may partially explain the observed health benefits of plant-based diets[148-150]. Mechanisms which have been associated with MR-induced lifespan extension are similar to those proposed for protein and calorie restriction and included reduced mitochondrial reactive oxygen species generation, altered GCN2 and mTOR signaling, elevated hydrogen sulfide production, and reduced levels of circulating IGF-1, insulin, and glucose[141,143]. Additionally, MR affects histone methylation by altering SAM levels, and changes in

histone methylation have been connected to aging[151]. MR may also act by influencing

metabolic pathways connected to methionine metabolism such as polyamine

metabolism, which has been shown to influence lifespan[151,152].

1.4.4 Ketogenic Diet

A ketogenic diet (KD) has also been shown to influence lifespan under certain

conditions, but there is much less literature on this effect compared to the other lifespan-

extending diets discussed. It is hypothesized that in addition to its metabolic effects, the

elevated levels of ketone bodies sustained during a ketogenic diet might promote health

and increased longevity through signaling functions, as the ketone body beta-

hydroxybutyrate has been shown to inhibit histone deacetylases and the NLRP3

inflammasome, among others[153-155]. Two recent mouse studies showed that a ketogenic

diet can increase median lifespan, but does not alter maximal lifespan[156,157], and a third

study found no effect on lifespan[158]. Different studies on the ketogenic diet also have

conflicting results on how the diet influences metabolic health, including whether KD

improves or worsens glucose tolerance and whether it causes weight loss or gain[159-161].

The KD and control diets used in these studies often have very different macronutrient

compositions and feeding regimens, which can partially explain conflicting results.

However, there is no consensus on the "correct" way to implement a ketogenic diet-

while the classic ketogenic diet used in the treatment of epilepsy is defined as a "high-

fat, moderate-protein, low-carbohydrate diet"[28], as long as sustained ketosis is observed,

a low-carbohydrate diet is considered ketogenic. As previously mentioned, often studies

of ketogenic diets have lower protein content than the control diet they are compared

to[156,158,161]. Given the strong effect of protein content on lifespan, this can make it difficult

to disentangle the ketosis-specific effects from those related to protein restriction. One

study found that the beneficial metabolic effects of KD were lost when methionine was

supplemented into the diet to levels in the control diet[162]. Human studies on KD

generally show beneficial metabolic effects and weight loss[163-166], but it is unclear

whether these effects could be attributed to lower caloric intake in KD groups, and

safety concerns over long-term KD have arisen over reports of liver steatosis, increased

inflammation, increased low-density lipoprotein cholesterol, and decreased bone

mineral density [164,167-169]. In conclusion, more work needs to be done to determine how

ketogenic diets impact not just longevity, but overall health.

1.5 Ferroptosis

Ferroptosis was discovered over ten years ago as an oxidative, iron-dependent

form of cell death that was induced by the small molecule erastin, and which did not

share features of any other known types of regulated cell death such as apoptosis[75].

Erastin inhibits system x_c^-, which imports extracellular cystine at the expense of

intracellular glutamate[75,86,170]. After uptake, cystine is reduced to cysteine, which is

essential for glutathione biosynthesis[73,74,171]. Because glutathione is a cofactor for the

glutathione peroxidase enzyme GPX4, decreased levels of glutathione can diminish the

ability of GPX4 to detoxify potentially destructive lipid peroxide species[172]. Ferroptosis is defined as the cell death that occurs when cells are unable to adequately detoxify these species, whether that be due to glutathione depletion or direct loss of GPX4 function.

Ferroptosis contributes to pathological cell death in numerous disease models including those of glutamate-induced neurotoxicity, Huntington's disease, periventricular leukomalacia, renal tubular injury and acute renal failure, ischemia/reperfusion injury, and liver damage[75,173-179]. Additionally, ferroptosis has shown considerable significance in the context of cancer[76,180,181]. This is partially due to studies showing many drug-resistant cell types are sensitive to erastin and the GPX4 inhibitor RSL3, or that erastin can enhance the effectiveness of chemotherapy and radiotherapy [86-90,180,182,183]. There are also data which suggests certain cancers have increased reliance on system x_c^-[69-71], prompting the investigation of whether its blockade could be a selective cancer therapy[184].

Numerous metabolic pathways have been shown to influence ferroptosis[185,186], but there remains a lack of understanding on what type of cellular damage occurs during ferroptosis, and how cells undergoing ferroptosis ultimately die[187]. Metabolic profiling of cells undergoing ferroptosis can point to specific cellular dysfunctions and lead to a better understanding of these outstanding questions.

2. Serine synthesis through PHGDH coordinates nucleotide levels by maintaining central carbon metabolism[iii]

2.1 Background and Context

As discussed in Chapter 1.3.4, serine contributes to numerous cellular processes which are often dysregulated in cancer to promote cell survival and growth, and inhibiting serine metabolism pharmacologically or through dietary serine and glycine restriction are two potential methods to treat cancer. Pharmacological inhibitors targeting the first enzyme of the serine synthesis pathway, phosphoglycerate dehydrogenase (PHGDH), have been developed and shown preclinical success in slowing cancer growth. The use of these inhibitors along with genetic PHGDH depletion has also allowed for investigation of the outstanding question of why the serine synthesis pathway is so important to certain cancers even when extracellular serine is abundant. To examine this question, my colleagues and I used an allosteric PHGDH inhibitor, WQ-2101[109], and investigated how global metabolism and cellular fitness were affected under PHGDH inhibition. We found that PHGDH inhibition caused defects in

the pentose phosphate pathway and the citric acid cycle, both of which impacted

nucleotide synthesis and cellular proliferation. Our study offers an explanation as to

why many cancers rely on PHGDH and the serine synthesis pathway despite sufficient

environmental serine.

2.2 Results

2.2.1 Inhibition of PHGDH induces broad changes to metabolism

A previous study identified and validated the selectivity of compounds with

PHGDH inhibitory activity and nominated WQ-2101 as a specific, allosteric inhibitor of

PHGDH[109] (Fig. 1a). In agreement, cells cultured with increasing concentrations of WQ-

2101 displayed dose-dependent reduction in cell proliferation (Fig. 1b). Consistent with

other approaches targeting the serine synthesis pathway[103,105,108,109], cells with *PHGDH*

amplification or high expression of PHGDH were more sensitive to WQ-2101 due to

higher reliance on this pathway (Fig. 1c). We then sought to examine how acute PHGDH

inhibition affected global cellular metabolism, which has not to our knowledge been

previously reported. To test this, we used Liquid Chromatography coupled to High-

Resolution Mass Spectrometry (LC-HRMS) to generate a metabolite profile of HCT116

cells treated either with PHGDH inhibitor WQ-2101 or an siRNA targeting *PHGDH*. In

addition to reducing de novo serine synthesis (Fig. 2a,b), we observed large-scale

metabolomic changes in response to PHGDH inhibition (Fig. 1d). A pathway analysis

revealed that the pathways most affected were related to serine-glycine-one carbon

(SGOC) metabolism, central carbon metabolism (glycolysis and the TCA cycle), and

nucleotide metabolism (Fig. 1e). Although the inhibitory kinetics of a small molecule

and siRNA are inherently different and thus we would not expect complete concordance

between the genetic and pharmacological approaches, a statistical analysis

demonstrated that a majority of the metabolic pathways affected by PHGDH inhibition

were consistent among the two approaches, further validating the overall specificity of

WQ-2101 and defining the global changes to metabolism upon inhibition of PHGDH

(Fig. 1f).
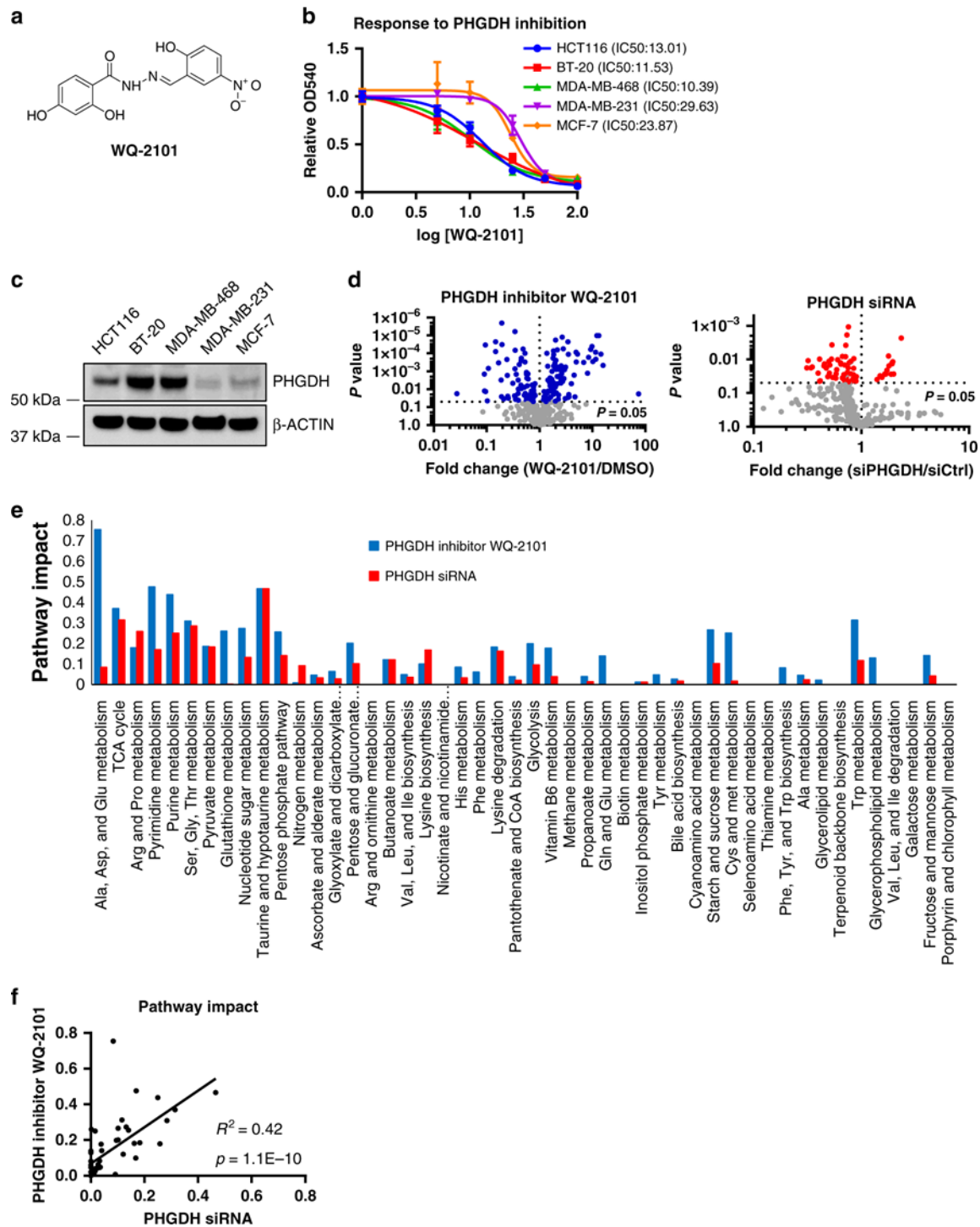
Figure 1: Inhibition of PHGDH induces broad changes in metabolism.

a) Chemical structure of PHGDH inhibitor WQ-2101. b) Dose-dependent response of cell lines treated with PHGDH inhibitor WQ-2101 for 72 h. Data are the mean of three biological replicates, and error bars represent s.e.m. c) Immunoblot demonstrating the expression level of PHGDH in cell lines. d) Volcano plots of metabolites in response to cells treated with 25 μM PHGDH inhibitor WQ-2101 for 24 h (left), or 20 nM siRNA targeting PHGDH 72 h post-transfection (right). Colored dots represent metabolites significantly changed between control and treated conditions (P < 0.05). Data are mean of three biological replicates. e) Network-based pathway analysis of statistically significant metabolites altered in each condition. f) Scatter plot for correlation of metabolic pathway impact scores between WQ-2101 and siRNA targeting PHGDH.
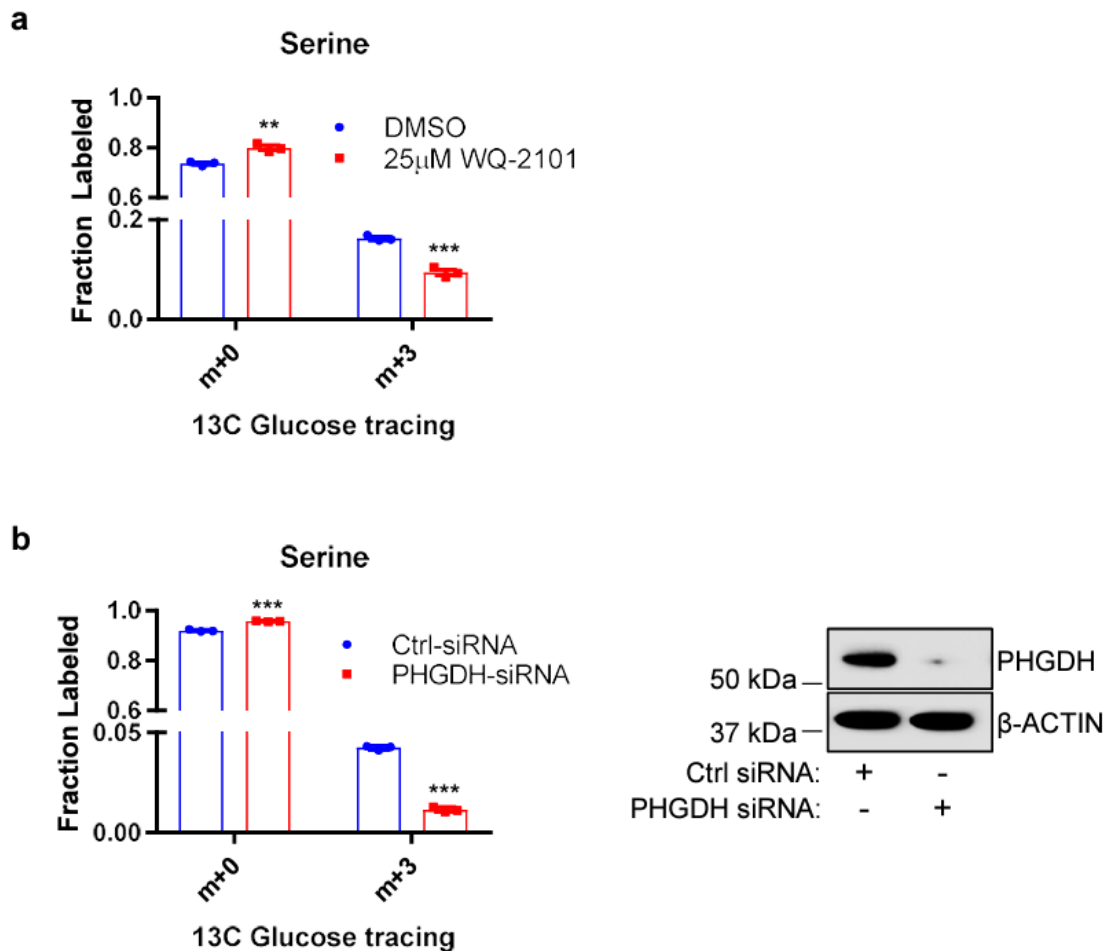
Figure 2: Serine synthesis under WQ-2101 treatment and PHGDH siRNA.

a) Cells were pre-treated with DMSO control or WQ-2101 for 4h followed by 13C-glucose tracing for 20h in the presence of DMSO or WQ-2101. Data are the mean of

three biological replicates, and error bars represent s.e.m. P < 0.01 [**], P < 0.005 [***], Student's t-test. b) Cells were transfected with 20 nM control siRNA or 20nM siRNA targeting PHGDH and 72h post-transfection 13C-glucose tracing was performed for 6h. Data are the mean of three biological replicates, and error bars represent s.e.m. P < 0.005 [***], Student's t-test.

2.2.2 PHGDH regulates central carbon and nucleotide metabolism

The observation that PHGDH inhibition affected central carbon and nucleotide

metabolism promoted us to look more deeply into the mechanism. Indeed, we found

HCT116 and BT-20 cells treated with WQ-2101 displayed alterations in glycolysis, TCA

cycle, pentose phosphate pathway, and both purine and pyrimidine biosynthesis

compared to control (Fig. 3a–e, Fig. 4a–e). Alterations in these metabolic pathways were

also observed in cells with *PHGDH* knocked down (Fig. 5). Numerous metabolic

processes are located both upstream and downstream of PHGDH activity (Fig. 3f). These

include other pathways connected to and involving glycolysis including NADH/NAD+

redox balance, pentose phosphate pathway, the TCA cycle and the network downstream

of serine that involves redox and nucleotide metabolism. To determine which metabolic

processes may be involved in the effects of PHGDH inhibition, we supplemented cells

with various metabolites related to PHGDH metabolism in the presence of WQ-2101

including pyruvate, lactate, α-ketobutyrate[188], N-acetyl-L-cysteine[189], cell-permeable α-

ketoglutarate, ribose, and nucleosides (Fig. 3g). Only the addition of nucleosides was

sufficient to rescue cells from PHGDH inhibition (Fig. 3g, h, Fig. 4f,g), confirming the

major function of PHGDH is to promote nucleotide synthesis as has been reported[108].
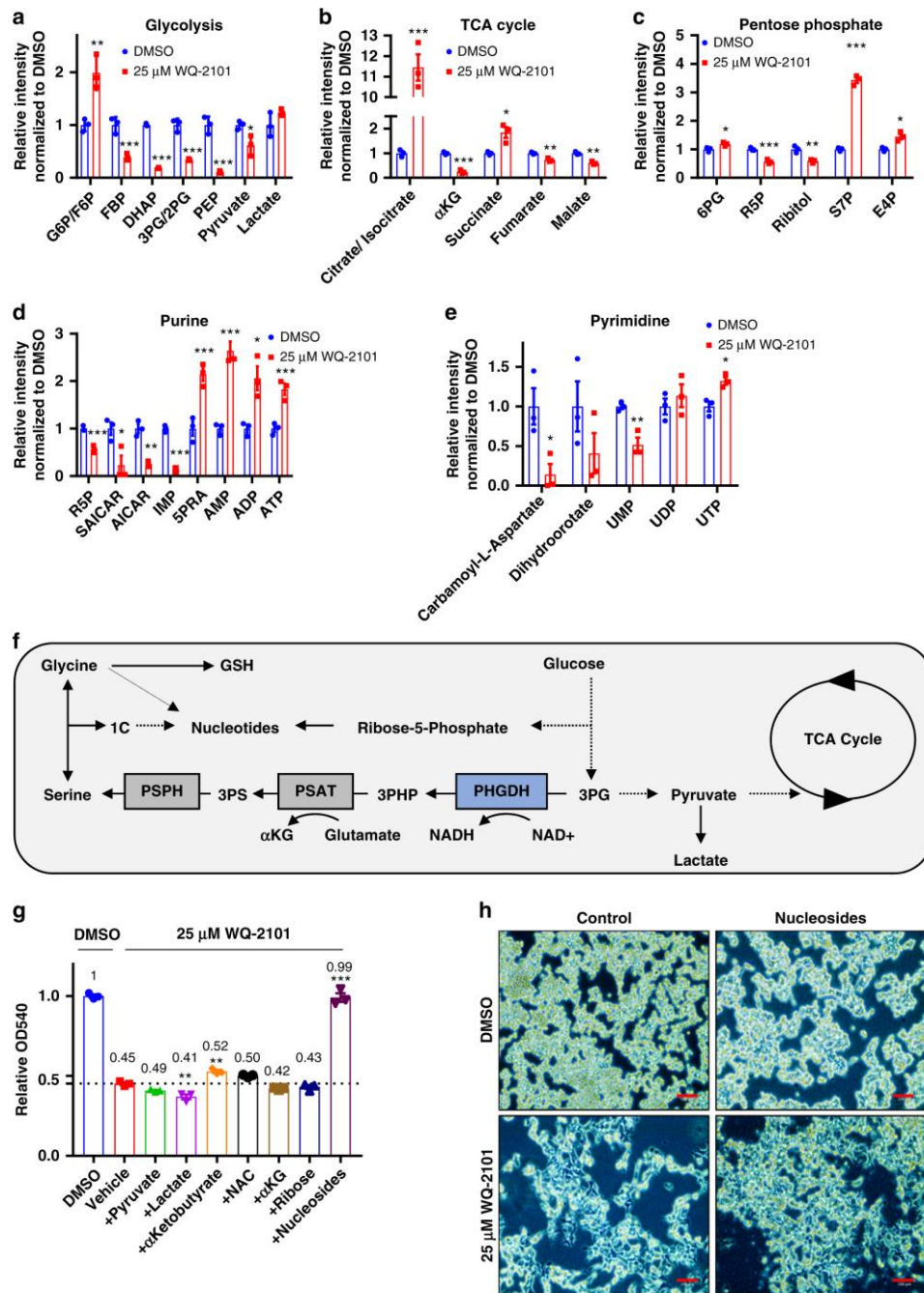
Figure 3: PHGDH inhibition disrupts central carbon and nucleotide metabolism.

a) Relative integrated peak intensities for glycolysis-related metabolites. G6P/F6P (glucose-6-phosphate/fructose-6-phosphate); FBP (fructose-1,6-bisphosphate); DHAP (dihydroxyacetone-phosphate); 3PG/2PG (3-phosphoglycerate/2-phosphoglycerate); PEP

(phosphoenolpyruvate). Data are the mean of three biological replicates, and error bars represent s.e.m. $P < 0.05$ [*], $P < 0.01$ [**], $P < 0.005$ [***], Student's t-test. **b)** Relative integrated peak intensities for TCA cycle-related metabolites. (αKG) α-ketoglutarate. Data are the mean of three biological replicates, and error bars represent s.e.m. $P < 0.05$ [*], $P < 0.01$ [**], $P < 0.005$ [***], Student's t-test. **c)** Relative integrated peak intensities for pentose phosphate pathway-related metabolites. 6PG (6-phosphogluconic acid); R5P (ribose-5-phosphate); S7P (sedoheptulose-7-phosphate); E4P (erythrose-4-phosphate). Data are the mean of three biological replicates, and error bars represent s.e.m. $P < 0.05$ [*], $P < 0.01$ [**], $P < 0.005$ [***], Student's t-test. **d)** Relative integrated peak intensities for purine biosynthetic precursors. R5P (ribose-5-phosphate); SAICAR ((S)-2-[5-Amino-1-(5-phospho-D-ribosyl)imidazole-4-carboxamido]succinate); AICAR (5-amino-1-[3,4-dihydroxy-5-(hydroxymethyl)oxolan-2-yl]imidazole-4-carboxamide); IMP (inosine monophosphate); AMP (adenosine monophosphate); ADP (adenosine diphosphate); ATP (adenosine triphosphate). Data are the mean of three biological replicates, and error bars represent s.e.m. $P < 0.05$ [*], $P < 0.01$ [**], $P < 0.005$ [***], Student's t-test. **e)** Relative integrated peak intensities for pyrimidine biosynthetic precursors. UMP (uridine monophosphate); UDP (uridine diphosphate); UTP (uridine triphosphate). Cells were treated with 25 µM WQ-2101 for 24 h. Integrated peak intensities were normalized to DMSO control. Data are the mean of three biological replicates, and error bars represent s.e.m. $P < 0.05$ [*], $P < 0.01$ [**], Student's t-test. **f)** Schematic of the PHGDH metabolic network. 3PHP (3-phosphohydroxypyruvate); 3PS (3-phosphoserine); 1C (one-carbon unit); GSH (reduced glutathione); PHGDH (phosphoglycerate dehydrogenase); PSAT (phosphoserine aminotransferase); PSPH (phosphoserine phosphatase). **g)** MTT assay of cells treated with DMSO control, 25 µM WQ-2101, or 25 µM WQ-2101 supplemented with reagents as indicated for 72 h. OD540 values are relative to DMSO control. Numbers indicate fold change relative to DMSO control. $P < 0.005$ [***], one-way ANOVA. **h)** Representative image of cells upon nucleoside rescue. Scale bar = 100 µm
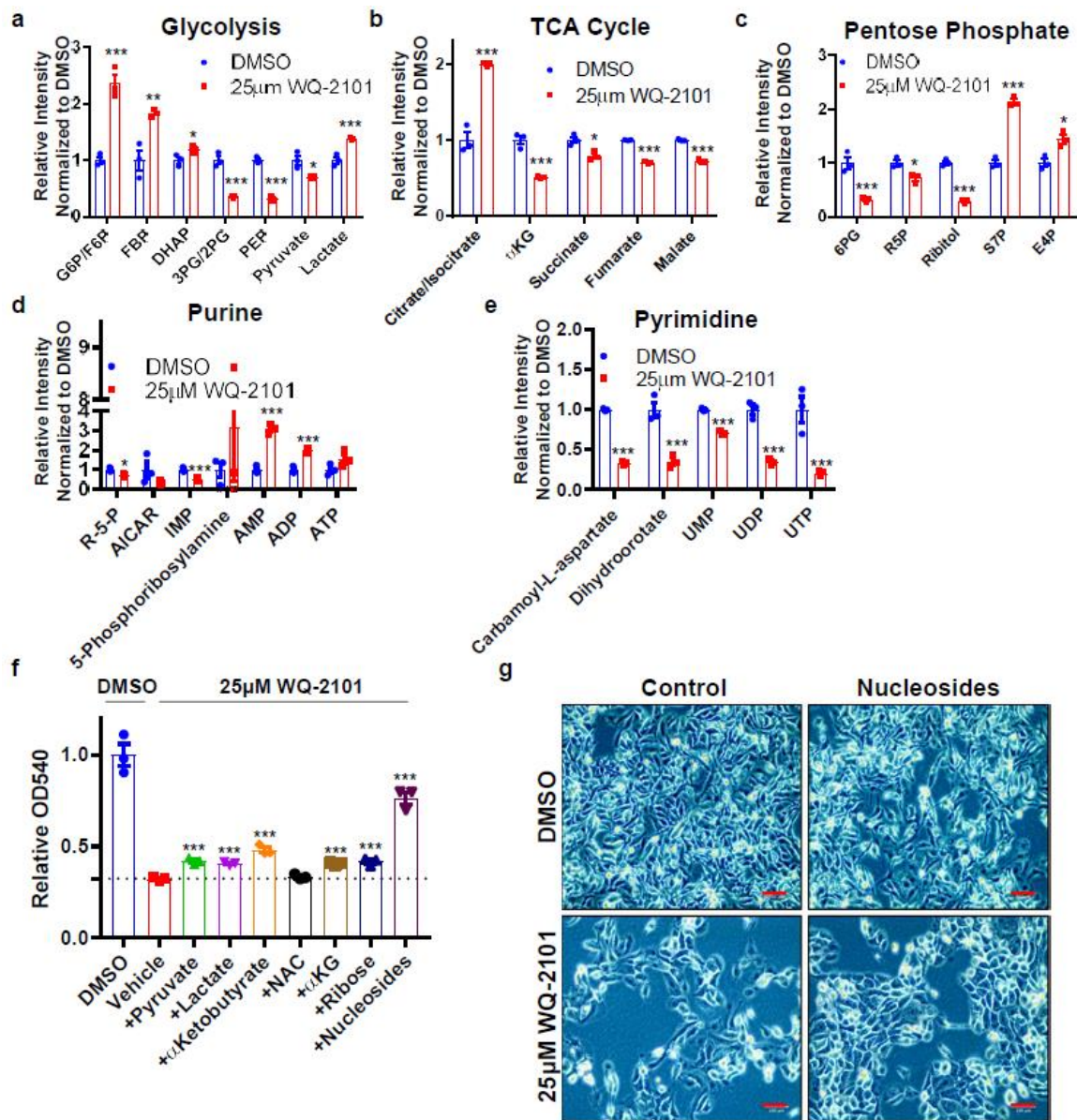
Figure 4: BT-20 central carbon and nucleotide metabolism.

a) Relative integrated peak intensities for glycolysis-related metabolites. G6P/F6P (glucose-6-phosphate/fructose-6-phosphate); FBP (fructose-1,6-bisphosphate); DHAP (dihydroxyacetonephosphate); 3PG/2PG (3-phosphoglycerate/2-phosphoglycerate); PEP (phosphoenolpyruvate). Data are the mean of three biological replicates, and error bars represent s.e.m. P < 0.05 [*], P <0.01 [**], P < 0.005 [***], Student's t-test. b) Relative integrated peak intensities for TCA cycle related metabolites. (αKG) α-ketoglutarate. Data are the mean of three biological replicates, and error bars represent s.e.m. P < 0.05 [*], P < 0.005 [***], Student's t-test. c) Relative integrated peak intensities for pentose

phosphate pathway-related metabolites. 6PG (6-phosphogluconic acid); R5P (ribose-5-phosphate); S7P (sedoheptulose-7-phosphate); E4P (erythrose-4-phosphate). Data are the mean of three biological replicates, and error bars represent s.e.m. $P < 0.05$ [*], $P < 0.005$ [***], Student's t-test. d) Relative integrated peak intensities for purine biosynthetic precursors. R5P (ribose-5-phosphate); AICAR (5-amino-1-[3,4-dihydroxy-5-(hydroxymethyl)oxolan-2-yl]imidazole-4-carboxamide); IMP (inosine monophosphate); AMP(adenosine monophosphate); ADP (adenosine diphosphate); ATP (adenosine triphosphate). Data are the mean of three biological replicates, and error bars represent s.e.m. $P < 0.05$ [*], $P < 0.005$[***], Student's t-test. e) Relative integrated peak intensities for pyrimidine biosynthetic precursors. UMP (uridine monophosphate); UDP (uridine diphosphate); UTP (uridine triphosphate). Cells were treated with 25μM WQ-2101 for 24h. Integrated peak intensities were normalized to DMSO control. Data are the mean of three biological replicates, and error bars represent s.e.m. $P < 0.005$ [***], Student's t-test. f) MTT assay of cells treated with DMSO control, 25μM WQ-2101, or 25μM WQ-2101 supplemented with reagents as indicated for 72h. OD540 values are relative to DMSO control. $P < 0.005$ [***], one-way ANOVA. g) Representative image of cells upon nucleoside rescue. Scale bar = 100μm.
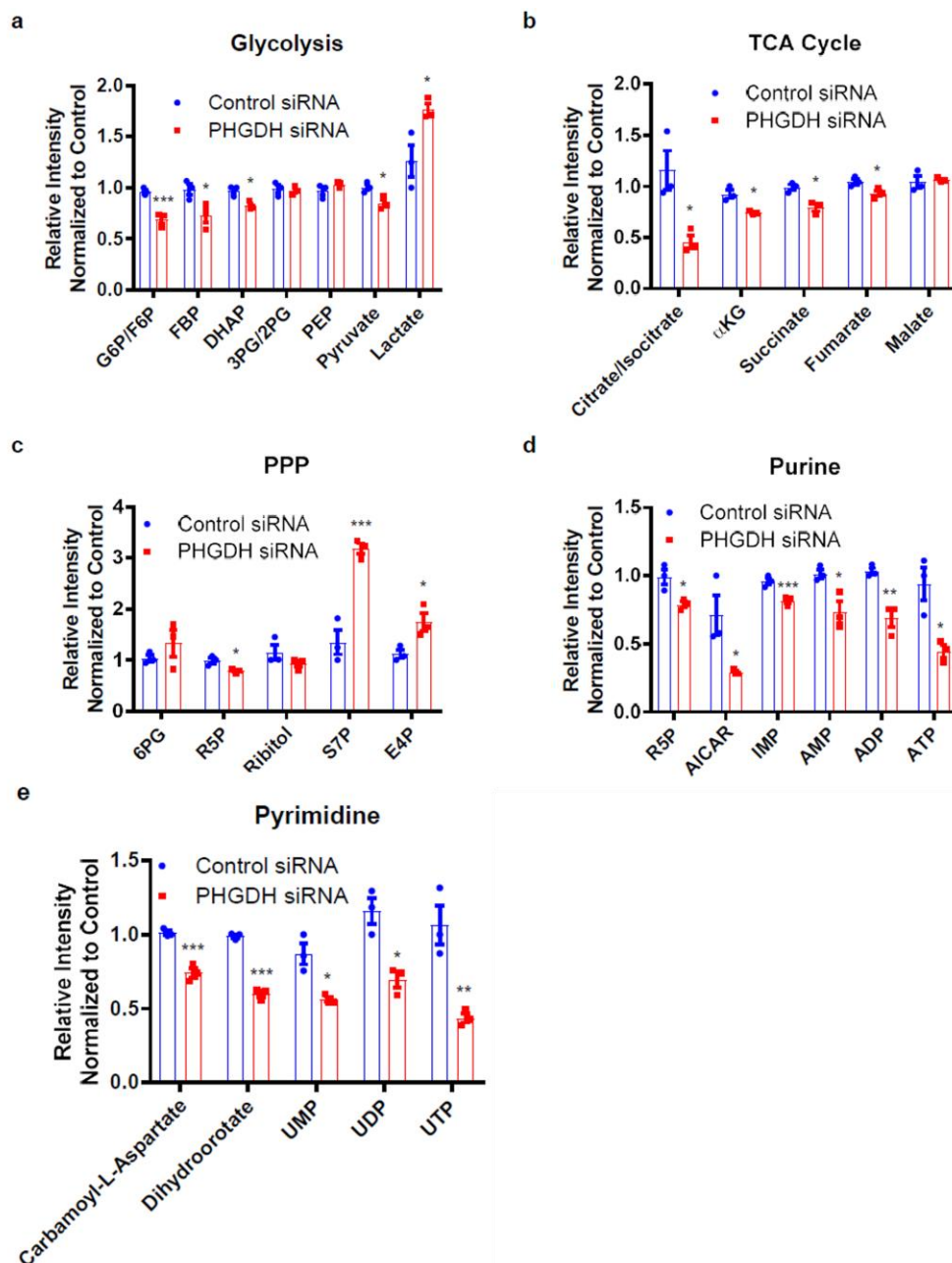
Figure 5: PHGDH knockdown central carbon and nucleotide metabolism.

a) Relative integrated peak intensities for glycolysis-related metabolites. G6P/F6P (glucose-6-phosphate/fructose-6-phosphate); FBP (fructose-1,6-bisphosphate); DHAP (dihydroxyacetonephosphate); 3PG/2PG (3-phosphoglycerate/2-phosphoglycerate); PEP (phosphoenolpyruvate). Data are the mean of three biological replicates, and error bars represent s.e.m. P < 0.05 [*], P< 0.005 [***], Student's t-test. b) Relative integrated peak

intensities for TCA cycle-related metabolites. (αKG) α-ketoglutarate. Data are the mean of three biological replicates, and error bars represent s.e.m. P < 0.05 [*], Student's t-test. c) Relative integrated peak intensities for pentose phosphate pathway-related metabolites. 6PG (6-phosphogluconic acid); R5P (ribose-5-phosphate); S7P (sedoheptulose-7-phosphate); E4P (erythrose-4-phosphate). Data are the mean of three biological replicates, and error bars represent s.e.m. P < 0.05 [*], P < 0.005 [***], Student's t-test. d) Relative integrated peak intensities for purine biosynthetic precursors. R5P (ribose-5-phosphate); AICAR (5-amino-1-[3,4-dihydroxy-5-(hydroxymethyl)oxolan-2-yl]imidazole-4-carboxamide); IMP (inosine monophosphate); AMP (adenosine monophosphate); ADP (adenosine diphosphate); ATP (adenosine triphosphate). Data are the mean of three biological replicates, and error bars represent s.e.m. P < 0.05 [*], P < 0.01 [**], P < 0.005 [***] Student's t-test. e) Relative integrated peak intensities for pyrimidine biosynthetic precursors. UMP (uridine monophosphate); UDP (uridine diphosphate); UTP (uridine triphosphate). Data are the mean of three biological replicates, and error bars represent s.e.m. P < 0.05 [*], P < 0.01 [**], P< 0.005 [***], Student's t-test. For all panels, cells were transfected with 20 nM control siRNA or 20nM siRNA targeting PHGDH and assayed 72h post-transfection. Integrated peak intensities were normalized to control siRNA.

2.2.3 De novo nucleotide synthesis is altered by PHGDH inhibition

It is thought that the major mechanism of how PHGDH regulates nucleotide synthesis in proliferating cells is by maintaining folate pools and providing glycine for the purine backbone[108]. However, from global metabolite profiling, our results indicate that simultaneous alterations of many other pathways and metabolic processes may contribute to reduced nucleotide synthesis. To study how PHGDH regulates nucleotide metabolism, we used stable isotope tracing by culturing cells in medium supplemented with uniformly labeled glucose ([U-^{13}C] glucose), and measured glucose incorporation into numerous pathways that are involved in purine and pyrimidine synthesis with and without PHGDH inhibition via LC-HRMS. Glucose contributes carbons to the purine precursor IMP through ribose-5-phosphate generation in the pentose phosphate

pathway, and through glycine and 10-formyl-tetrahydrafolate from the serine synthesis

pathway (Fig. 6a). Interestingly, HCT116 cells treated with PHGDH inhibitor WQ-2101

displayed altered isotopomer distributions of IMP (Fig. 6b). For the pyrimidine

intermediate UMP, in addition to ribose-5-phosphate, glucose can contribute carbons via

aspartate derived from the TCA cycle (Fig. 6c). As with IMP, HCT116 cells treated with

WQ-2101 also resulted in altered isotopomer distributions of the pyrimidine

intermediate UMP (Fig. 6d). Similar results were obtained in BT-20 cells treated with

WQ-2101 and cells treated with a different PHGDH inhibitor compound, NCT-5035 (Fig.

7). Of particular significance, the m+5 isotopomers of IMP and UMP were reduced,

demonstrating a reduction in ribose-5-phosphate incorporation from glucose.

Importantly, the altered labeling patterns were not the consequence of off-target effects

of WQ-2101 as cells with CRISPR-Cas9-mediated knockout of *PHGDH*[109] treated with

WQ-2101 showed labeling patterns consistent with vehicle control treated cells (Fig. 8).

Together, the observed isotope labeling patterns along with our findings that PHGDH

ablation affected other glycolysis-related pathways such as the TCA cycle and pentose

phosphate pathway show that PHGDH inhibition alters de novo synthesis of both

purine and pyrimidine nucleotides through a mechanism that may occur independent of

serine-dependent one carbon metabolism.
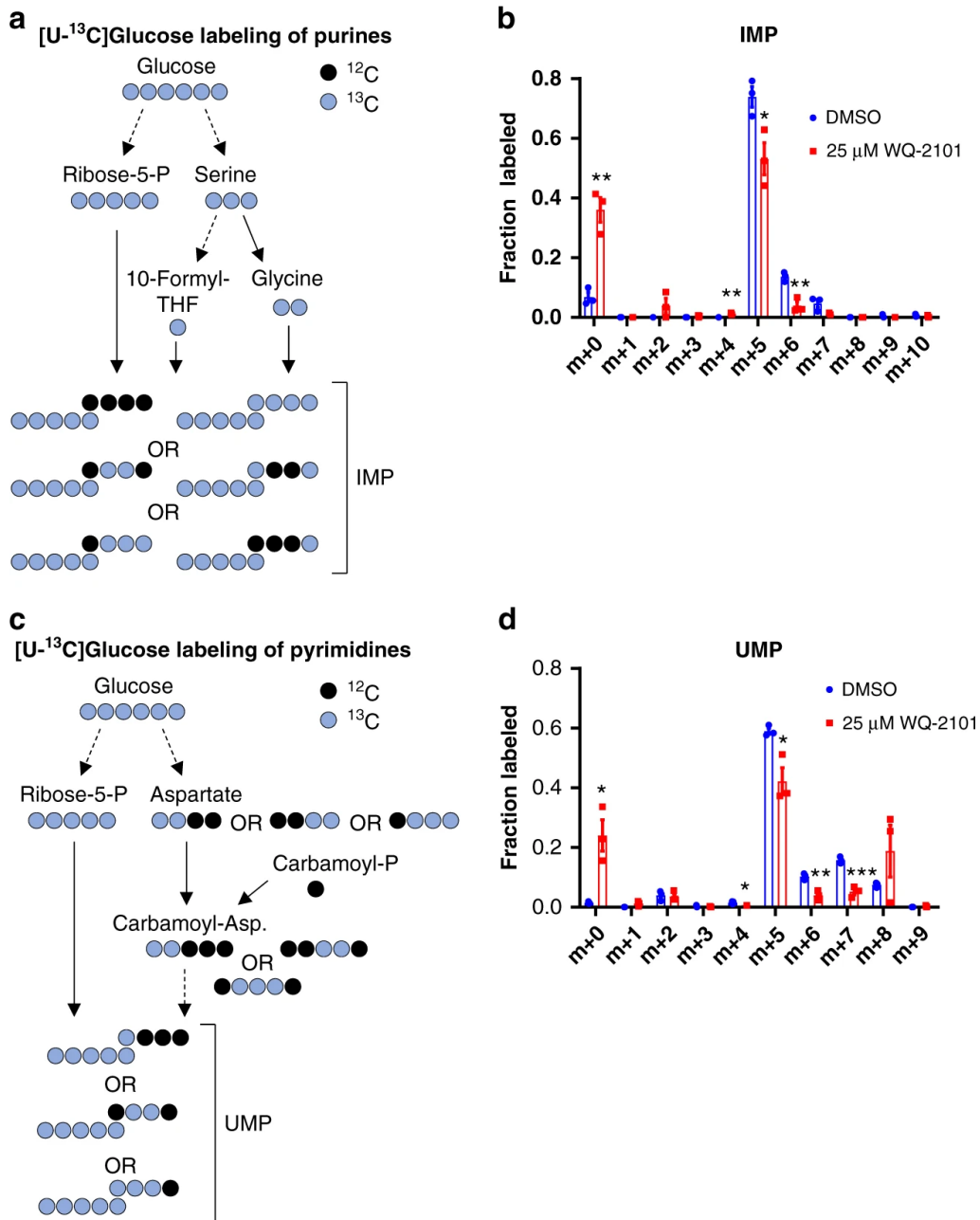
Figure 6 Glucose incorporation into nucleotides is altered upon PHGDH inhibition.

a) Schematic of [U-13C] glucose labeling of purines. **b)** Mass-isotopomer distribution (MID) of IMP (inosine monophosphate) from [U-13C] glucose in cells treated with 25 μM WQ-2101. Data are the mean of three biological replicates, and error bars represent s.e.m. $P < 0.05$ [*], $P < 0.01$ [**], Student's *t*-test. **c)** Schematic of [U-13C] glucose labeling of pyrimidines. **d)** Mass-isotopomer distribution (MID) of UMP (uridine monophosphate)

from [U-^{13}C] glucose in cells treated with 25 μM WQ-2101. Data are the mean of three biological replicates, and error bars represent s.e.m. $P < 0.05$ [*], $P < 0.01$ [**], $P < 0.005$ [***], Student's t-test. For labeling experiments, cells were pre-treated with inhibitors for 4 h followed by introduction of [U-^{13}C] glucose-containing medium including inhibitors for 20 h.
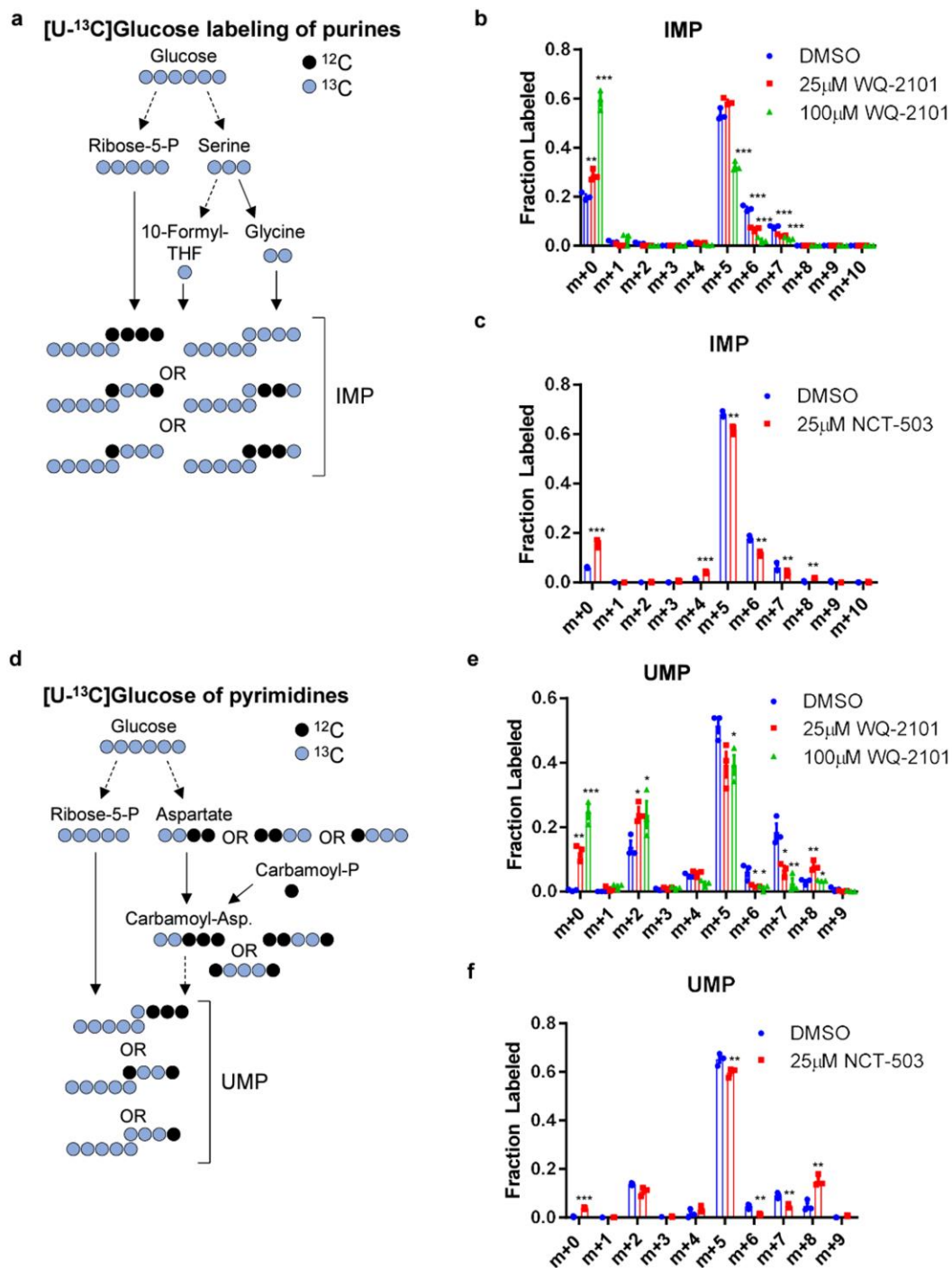
Figure 7: Supplementary [U-¹³C]Glucose labeling of nucleotides.

a) Schematic of [U-¹³C] glucose labeling of purines. b,c) Mass-isotopomer distribution (MID) of IMP (inosine monophosphate) from [U-¹³C] glucose in BT-20 cells

treated with 25μM WQ-2101 b) and HCT116 cells treated with 25μM NCT-503 c). Data are the mean of three biological replicates, and error bars represent s.e.m. P < 0.01 [**], P < 0.005 [***], Student's t-test. d) Schematic of [U-13C] glucose labeling of pyrimidines. e,f) Mass-isotopomer distribution (MID) of UMP (uridine monophosphate) from [U-13C] glucose in BT-20 cells treated with 25μM WQ-2101 (e) and HCT116 cells treated with 25μM NCT-503 f). Data are the mean of three biological replicates, and error bars represent s.e.m. P < 0.05 [*], P < 0.01 [**], P < 0.005 [***], Student's t-test. For labeling experiments, cells were pre-treated with inhibitors for 4h followed by introduction of [U-13C] glucose-containing medium including inhibitors for 20h.
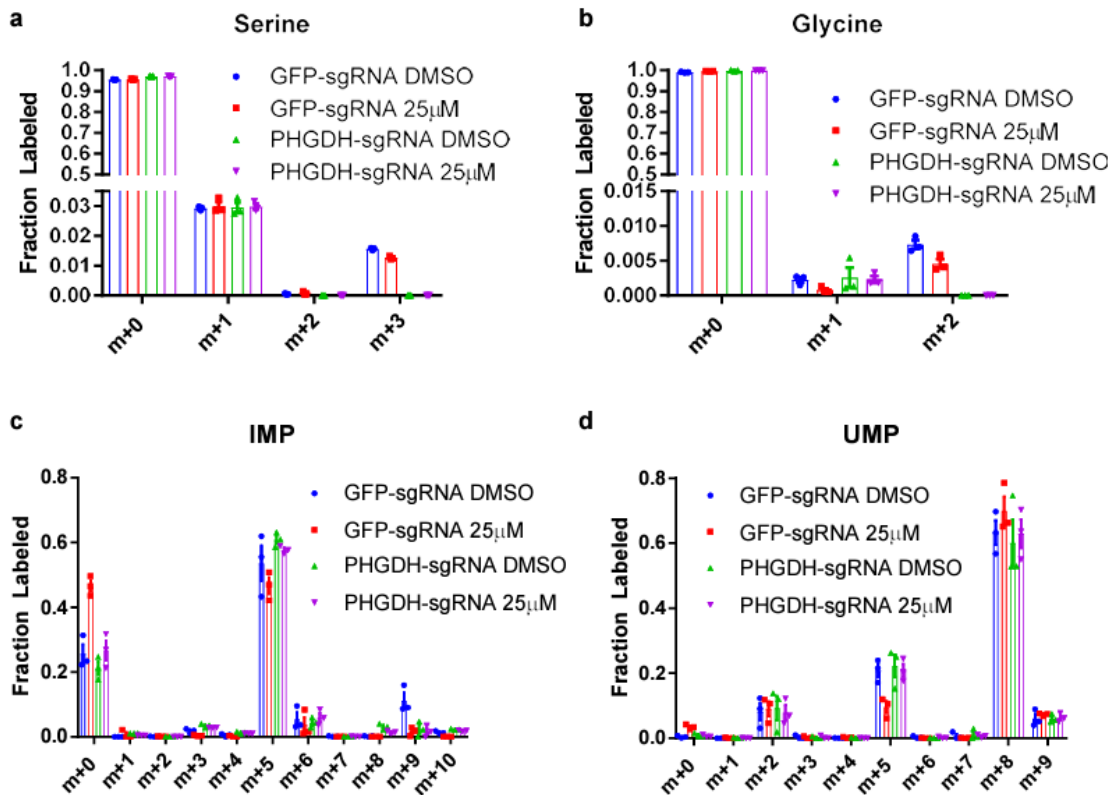
Figure 8: WT and PHGDH KO [U-13C]Glucose labeling of nucleotides.

a) Mass-isotopomerdistribution (MID) of serine from [U-13C] glucose in cells treated with 25μM WQ2101. Data are the mean of three biological replicates, and error bars represent s.e.m. b) Mass isotopomer distribution (MID) of glycine from [U-13C] glucose in cells treated with 25μM WQ-2101. Data are the mean of three biological replicates, and error bars represent s.e.m. c) Mass isotopomer distribution (MID) of IMP (inosine monophosphate) from [U-13C] glucose in cells treated with 25μM WQ-2101. Data are the

mean of three biological replicates, and error bars represent s.e.m. d) Mass-isotopomer distribution (MID) of UMP (uridine monophosphate) from [U-13C] glucose in cells treated with 25µM WQ-2101. Data are the mean of three biological replicates, and error bars represent s.e.m. For labeling experiments, cells were pre-treated with inhibitors for 4h followed by introduction of [U-13C] glucose-containing medium including inhibitors for 20h.

2.2.4 Quantitative flux analysis of nucleotide metabolism

In general, isotope labeling patterns are not sufficient to infer the extent of metabolic flux through a given pathway[190-194]. Therefore, we developed and applied a quantitative model that computes carbon fluxes into nucleotides with and without PHGDH inhibition from the mass-isotopomer distributions (MIDs) obtained from experiments in Fig. 6. The metabolic network includes flux estimates for 3PG to serine, serine to glycine, glucose-6-phosphate (G6P) to R5P, pyruvate to acetyl-coA, pyruvate to oxaloacetate, exogenous serine input, exogenous glycine input, exogenous aspartate uptake, IMP synthesis, IMP salvage, UMP synthesis, and UMP salvage (Fig. 9a). As expected, our calculations found that PHGDH inhibition reduced carbon flux to nucleotides from the serine synthesis pathway (3PG to serine), although this was a relatively small flux in general (Fig. 9b). Of significance, we found fluxes into nucleotides from the TCA cycle (Pyruvate to Acetyl-CoA and Pyruvate to OAA) and the pentose phosphate pathway (G6P to R5P) were with greater magnitude reduced by PHGDH inhibition relative to the decrease in flux to the serine synthesis pathway (Fig. 9b). Interestingly, the serine to glycine flux into nucleotides was relatively unchanged, suggesting folate availability is uncompromised when the serine synthesis pathway is

inhibited (Fig. 9b). These results demonstrate that PHGDH activity is critical for supporting central carbon metabolism through mass balance. Thus, the results demonstrate that carbon fluxes into nucleotides from the pentose phosphate pathway and TCA cycle were reduced to a greater extent than those in the serine synthesis pathway. In addition, the magnitude of these fluxes were larger than those in the serine synthesis pathway suggesting that disruption of these carbon fluxes may be more detrimental to overall de novo nucleotide synthesis.
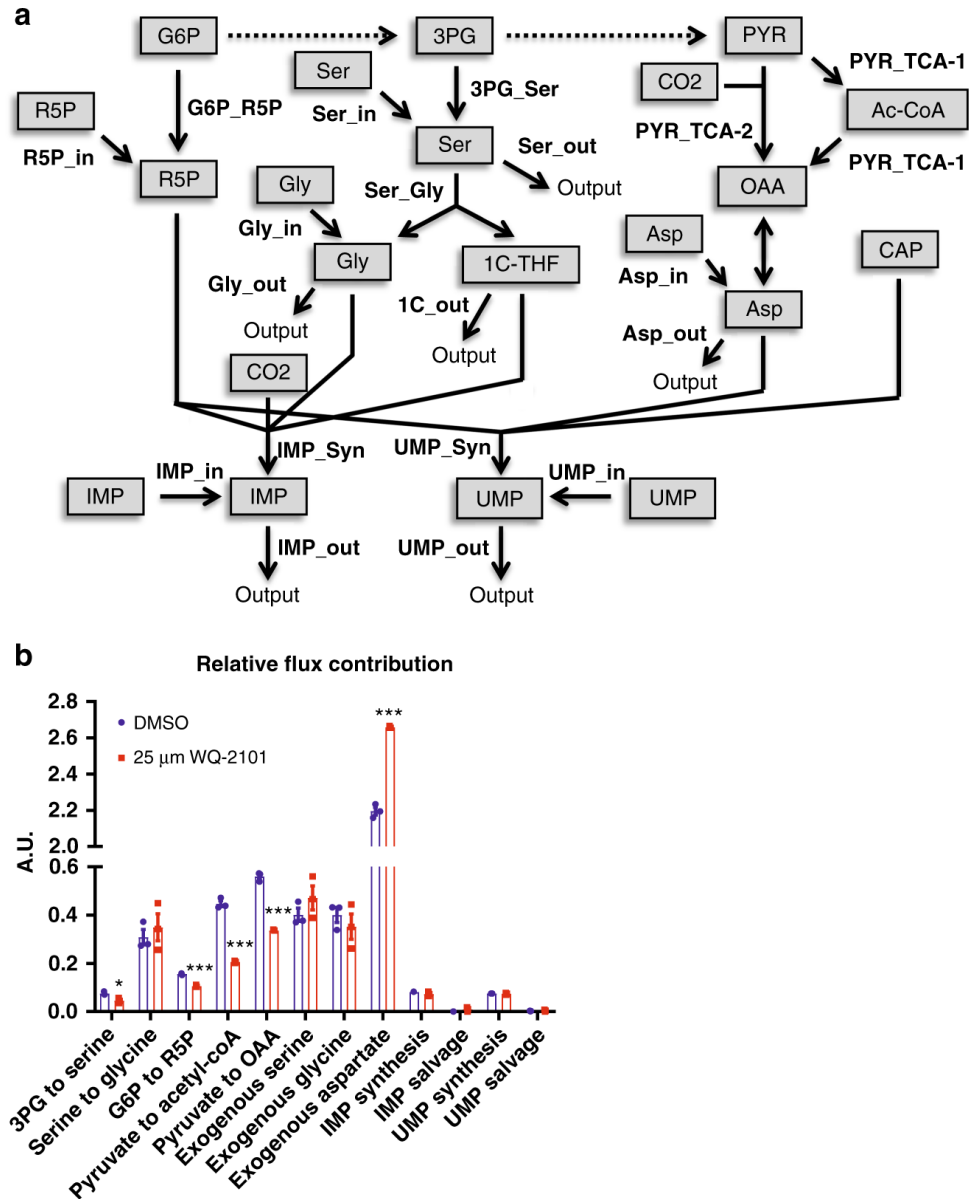
Figure 9: Quantitative flux analysis reveals that PHGDH supports central carbon metabolism.

a) Schematic of metabolic flux analysis model. R5P (ribose-5-phosphate); G6P (glucose-6-phosphate); Ser (serine); Gly (glycine), 3PG (3-phosphoglycerate); CO_2 (carbon dioxide); PYR (pyruvate); Ac-CoA (acetyl-coA); OAA (oxaloacetate); Asp (aspartate); CAP (carbamoyl phosphate); UMP (uridine monophosphate); IMP (inosine monophosphate). **b)** Relative flux rate of metabolic pathways in cells treated with 25 μM

WQ-2101. Data are the mean of three biological replicates, and error bars represent s.e.m. $P < 0.01$ [**], $P < 0.005$ [***], Student's t-test.

2.2.5 Kinetic profiling of central carbon metabolism

Given the complexities of flux estimation, we next considered an alternative approach aimed to directly measure flux into metabolic pathways using kinetic flux profiling[195-199] to further confirm the mechanism. We cultured HCT116 cells in the presence of DMSO or WQ-2101 for 24h in 12C glucose-containing medium, then fed cells [U-^{13}C] glucose-containing medium (with the same treatments) and extracted metabolites at numerous time points. We then used LC-HRMS and examined glucose incorporation over time at three different branch points of glycolysis important for nucleotide synthesis: the pentose phosphate pathway (ribose-5-phosphate), serine synthesis pathway (3PG, serine, glycine), and the TCA cycle (citrate/isocitrate, αKG, succinate, fumarate, malate, aspartate) (Fig. 10a). Strikingly, we observed flux through the serine synthesis pathway was largely unchanged in response to PHGDH inhibition (Fig. 10b–d). In contrast, there was a dramatic reduction in flux through the pentose phosphate pathway (Fig. 5e) and the TCA cycle (Fig. 10f–k). Similar reductions in flux through the pentose phosphate pathway and the TCA cycle were found in BT-20 cells treated with WQ-2101 and in cells treated a different PHGDH inhibitor compound, NCT-5035 (Fig. 11). Moreover, [U-^{13}C] glutamine tracing of cells treated with DMSO or WQ-2101 revealed labeling patterns consistent with reduced TCA cycle flux upon PHGDH inhibition (Fig. 12). Taken together, the metabolic flux analysis and kinetic flux

profiling reveal that PHGDH inhibition has a larger effect on central carbon flux than the serine synthesis pathway, and that the mechanism of how PHGDH inhibition leads to reduced nucleotide synthesis is through the loss of mass balance from altered anabolic central carbon flux.
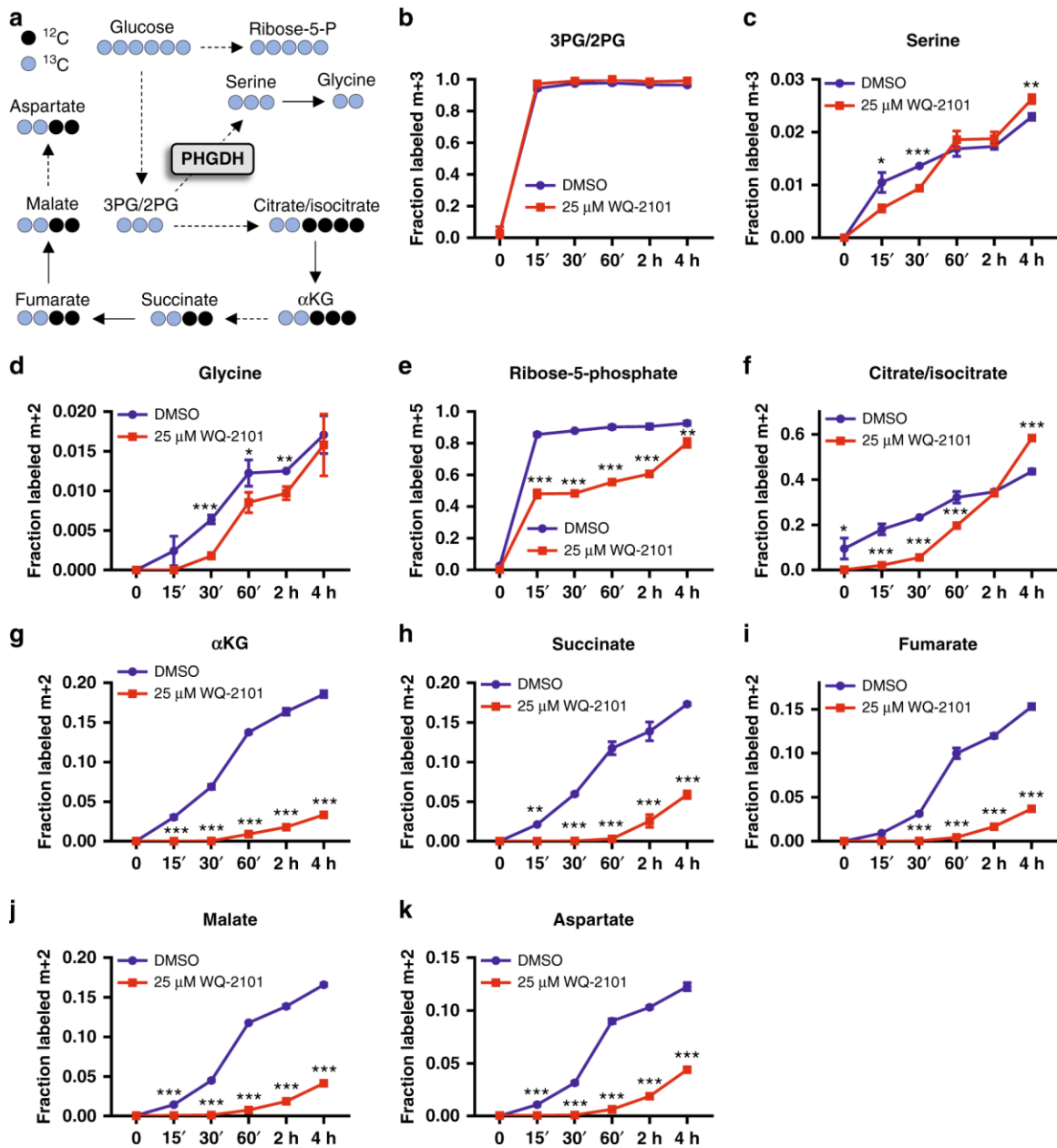
Figure 10 Kinetic profiling confirms reduced flux into the TCA cycle and PPP upon PHGDH inhibition.

a) Schematic of [U-13C] glucose labeling of serine, glycine, and central carbon metabolites. **b)** Fraction of the m + 3 isotopomer of 3PG/2PG (3-phosphoglycerate/2-phosphoglycerate) labeled in the presence (red) or absence (blue) of 25 μM WQ-2101. 3PG/2PG (3-phosphoglycerate/2-phosphoglycerate). Data are the mean of three biological replicates, and error bars represent s.e.m. **c)** Fraction of the m + 3 isotopomer of serine labeled in the presence (red) or absence (blue) of 25 μM WQ-2101. Data are the

44

mean of three biological replicates, and error bars represent s.e.m. $P < 0.05$ [*], $P < 0.01$ [**], $P < 0.005$ [***], Student's t-test. **d)** Fraction of the m + 2 isotopomer of glycine labeled in the presence (red) or absence (blue) of 25 μM WQ-2101. Data are the mean of three biological replicates, and error bars represent s.e.m. $P < 0.05$ [*], $P < 0.01$ [**], $P < 0.005$ [***], Student's t-test. **e)** Fraction of the m+5 isotopomer of ribose-5-phosphate labeled in the presence (red) or absence (blue) of 25 μM WQ-2101. Data are the mean of three biological replicates, and error bars represent s.e.m. $P < 0.01$ [**], $P < 0.005$ [***], Student's t-test. **f–k)** Fraction of the m + 2 isotopomers of citrate/isocitrate, αKG (α-ketoglutarate), succinate, fumarate, malate, and aspartate labeled in the presence (red) or absence (blue) of 25 μM WQ-2101. Data are the mean of three biological replicates, and error bars represent s.e.m. $P < 0.05$ [*], $P < 0.01$ [**], $P < 0.005$ [***], Student's t-test. In all experiments, cells were pre-treated with 25 μM WQ-2101 for 24h followed by introduction of [U-^{13}C] glucose-containing medium including inhibitor for the indicated times.
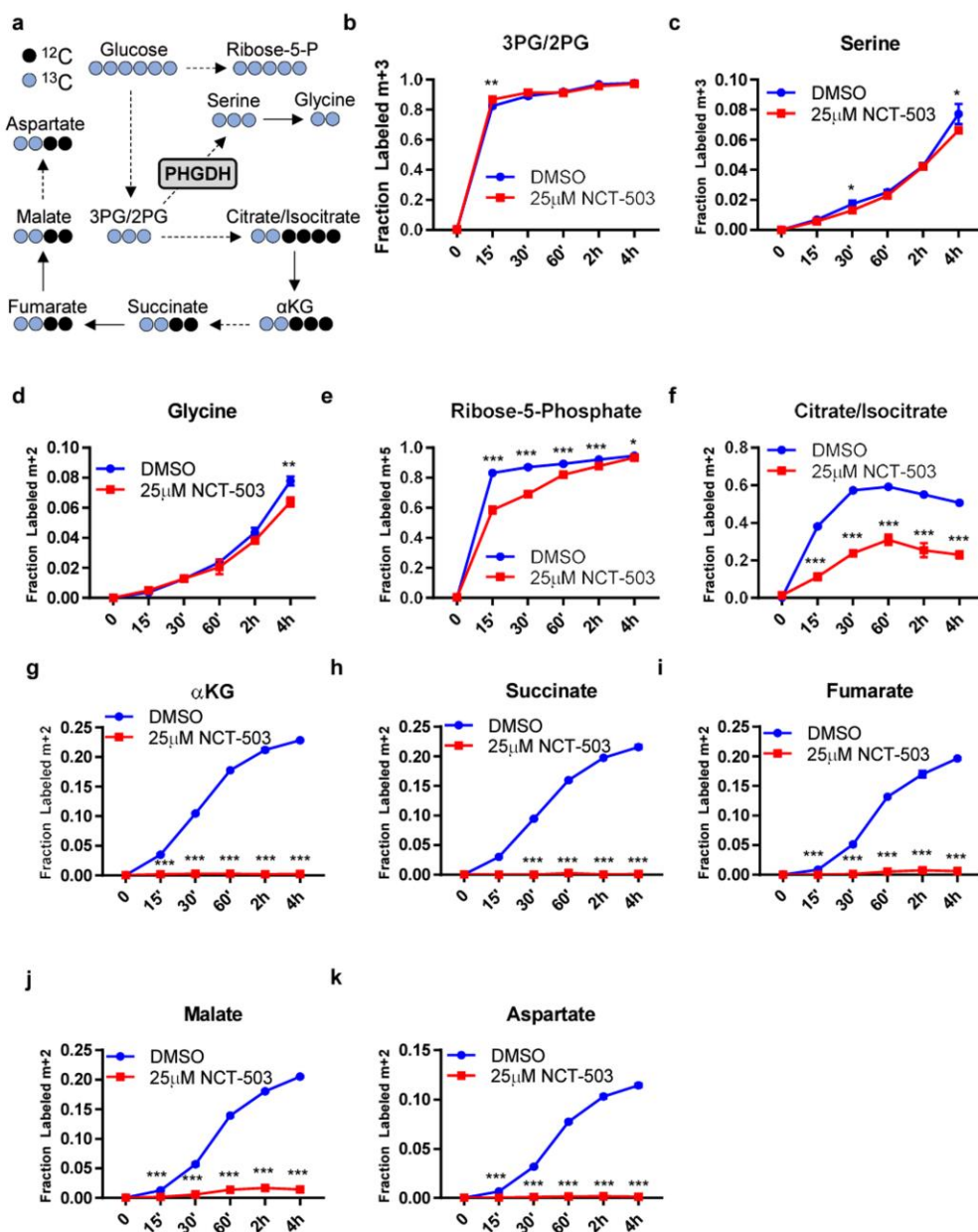
Figure 11: NCT-503 kinetic flux profiling.

a) Schematic of [U-^{13}C] glucose labeling of serine, glycine, and central carbon metabolites. b) Fraction of the m+3 isotopomer of 3PG/2PG (3-phosphoglycerate/2-phosphoglycerate) labeled in the presence (red) or absence (blue) of 25μM NCT-503. 3PG/2PG (3-phosphoglycerate/2-phosphoglycerate). Data are the mean of three biological replicates, and error bars represent s.e.m. P < 0.01 [**], Student's t-test. c) Fraction of the m+3 isotopomer of serine labeled in the presence `(red) or absence (blue) of 25μM NCT-503. Data are the mean of three biological replicates, and error bars

represent s.e.m. P < 0.05 [*], Student's t-test. d) Fraction of the m+2 isotopomer of glycine labeled in the presence (red) or absence (blue) of 25μM NCT-503. Data are the mean of three biological replicates, and error bars represent s.e.m. P < 0.01 [**], Student's t-test. e) Fraction of the m+5 isotopomer of ribose-5-phosphate labeled in the presence (red) or absence (blue) of 25μM NCT-503. Data are the mean of three biological replicates, and error bars represent s.e.m. P < 0.05 [*], P < 0.005 [***], Student's t-test. f-k) Fraction of the m+2 isotopomers of citrate/isocitrate, αKG (α-ketoglutarate), succinate, fumarate, malate, and aspartate labeled in the presence (red) or absence (blue) of 25μM NCT-503. Data are the mean of three biological replicates, and error bars represent s.e.m. P < 0.005 [***], Student's t-test. In all experiments, cells were pre-treated with 25μM NCT-503 for 24h followed by introduction of [U-^{13}C] glucose-containing medium including inhibitor for the indicated times.
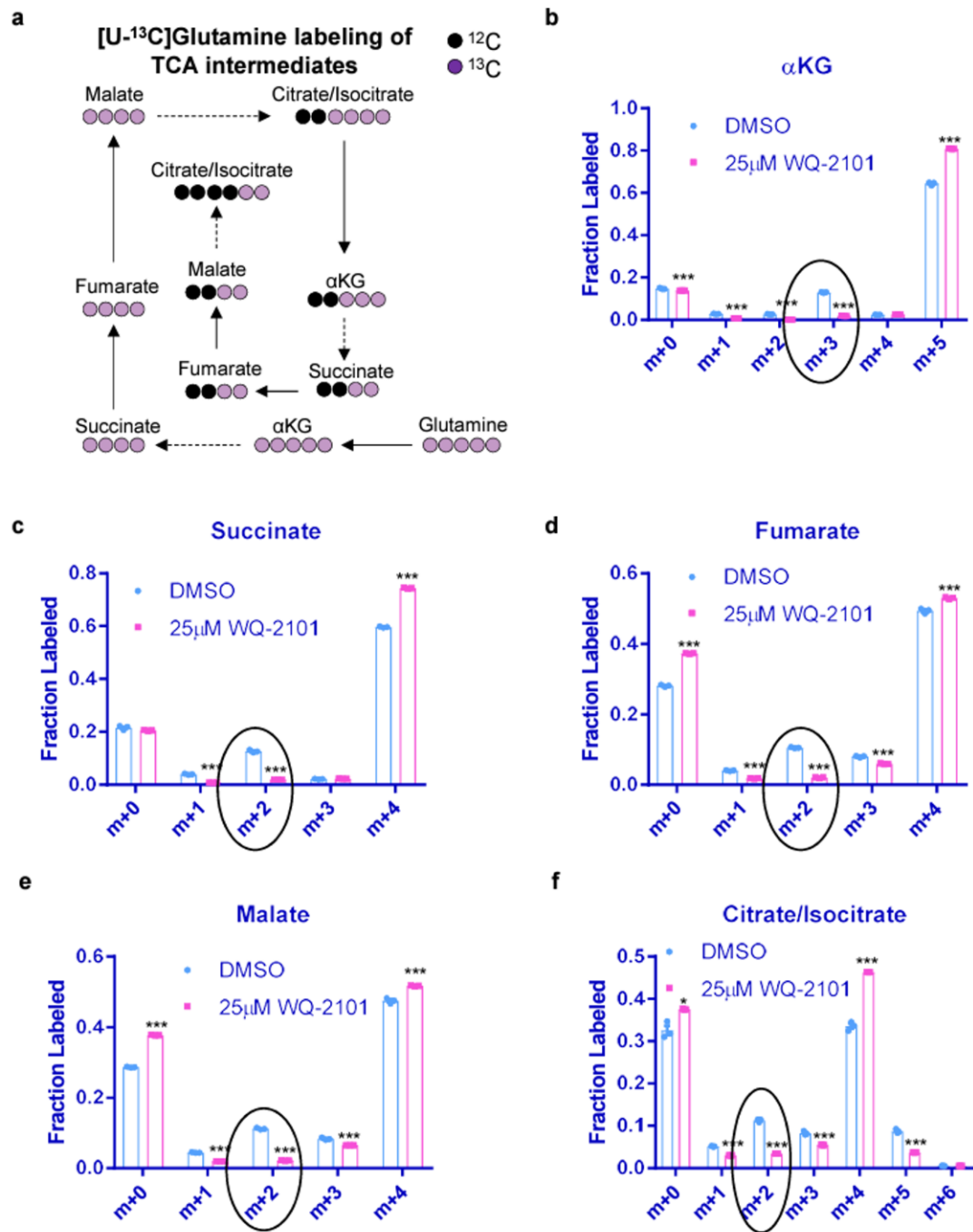
Figure 12: [U-¹³C]Glutamine labeling of TCA cycle.

a) Schematic of [U-¹³C] glutamine labeling of TCA cycle intermediates. b) Mass-isotopomer distribution (MID) of αKG (α-ketoglutarate) from [U-¹³C] glutamine in cells treated with DMSO control or 25µM WQ2101. Data are the mean of three biological replicates, and error bars represent s.e.m. $P < 0.005$ [***], Student's t-test. c) MID of

succinate from [U-^{13}C glutamine in cells treated with DMSO control or 25μM WQ-2101. Data are the mean of three biological replicates, and error bars represent s.e.m. P < 0.005 [***], Student's t-test. d) MID of fumarate from [U-^{13}C] glutamine in cells treated with DMSO control or 25μM WQ-2101. Data are the mean of three biological replicates, and error bars represent s.e.m. P < 0.005 [***], Student's t-test. e) MID of malate from [U-^{13}C] glutamine in cells treated with DMSO control or 25μM WQ-2101. Data are the mean of three biological replicates, and error bars represent s.e.m. P < 0.005 [***], Student's t-test. f) MID of citrate/isocitrate from [U-^{13}C] glutamine in cells treated with DMSO control or 25μM WQ-2101. Data are the mean of three biological replicates, and error bars represent s.e.m. P < 0.05 [*], P < 0.005 [***], Student's t-test. In all experiments, cells were pre-treated with DMSO or 25μM WQ-2101 for 4h followed by introduction of [U-^{13}C] glucose-containing medium including DMSO or WQ-2101 for 20h.

2.2.6 Restoration of TCA cycle and PPP rescues PHGDH inhibition

We then asked whether simultaneous restoration of pentose phosphate pathway

and TCA cycle metabolism could rescue cells from PHGDH inhibition. Indeed,

supplementing cells treated with WQ-2101 with ribose and cell-permeable α-

ketoglutarate was sufficient to attenuate the proliferative defects of PHGDH inhibition

(Fig. 13a, b, Fig. 14a, b), while supplementation with ribose and the one-carbon donor

formate was not, consistent with the hypothesis that one-carbon unit availability is

uncompromised during PHGDH inhibition (Fig. 14c). Furthermore, we performed LC-

HRMS on cells under the rescue conditions and observed an almost complete reversal in

TCA cycle (Fig. 13c) and pentose phosphate pathway (Fig. 13d) metabolites.

Importantly, we also found cells with PHGDH inhibition supplemented with ribose and

cell-permeable α-ketoglutarate had restored levels of purine (IMP) and pyrimidine

(UMP) precursors (Fig. 13e). In all, our data supports the mechanism whereby PHGDH

regulates the mass balance of central carbon metabolism and thus controls the fluxes

into the TCA cycle and pentose phosphate pathway to a greater extent than the SGOC network. Thus, the nucleotide deficiencies in response to PHGDH inhibition are largely due to reductions in central carbon flux (Fig. 13f).
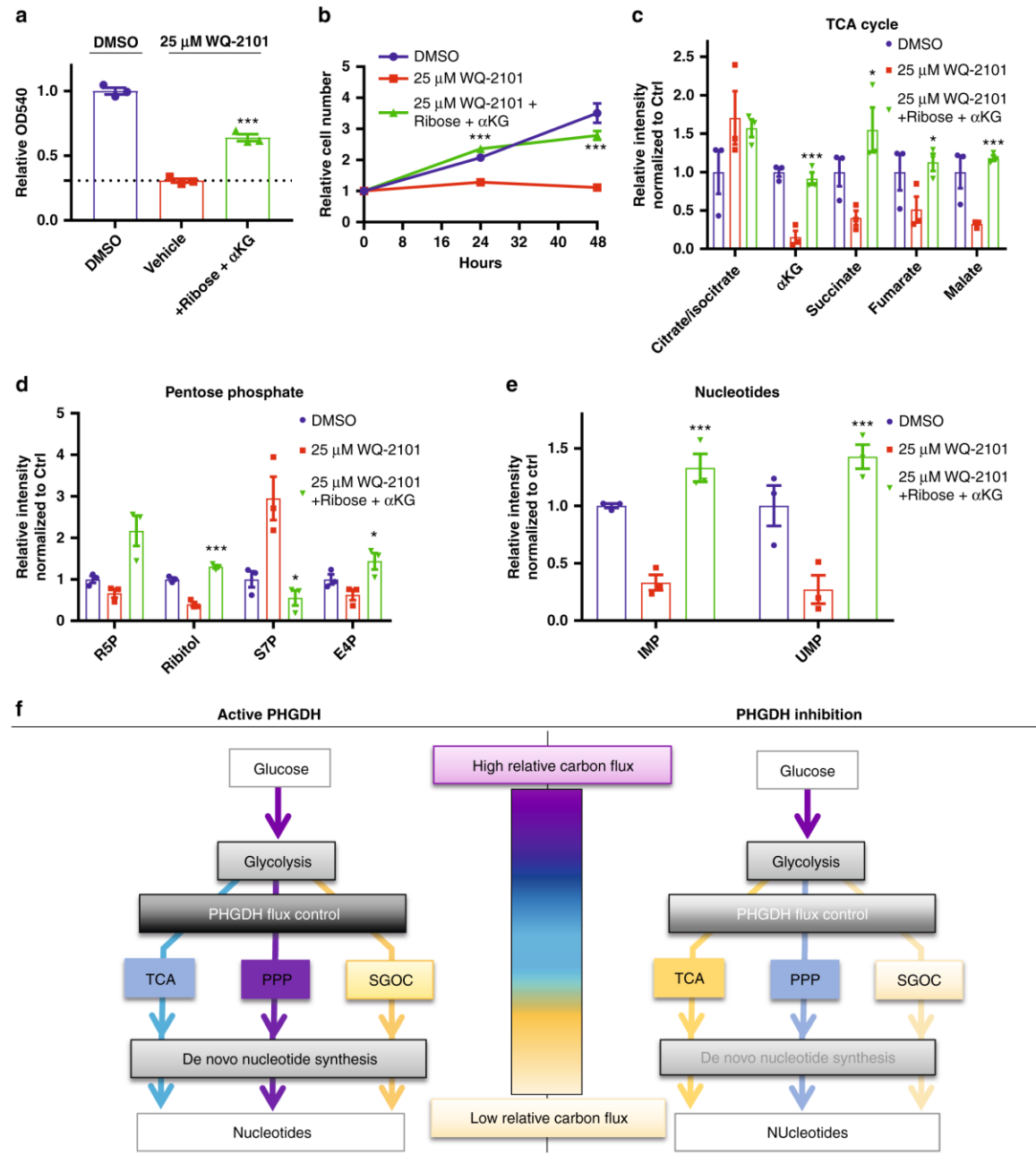
Figure 13: Restoration of TCA and PPP metabolism rescues cell proliferation during PHGDH inhibition.

a) MTT assay of cells treated with DMSO control, 25 µM WQ-2101, or 25 µM WQ-2101 supplemented with ribose and cell-permeable αKG (α-ketoglutarate) for 72 h. OD540 values are relative to DMSO control. Data are the mean of three biological replicates, and error bars represent s.e.m. $P < 0.005$ [***], Student's t-test. **b)** Proliferation assay of cells treated with DMSO control, 25 µM WQ-2101, or 25 µM WQ-2101 supplemented with ribose and cell-permeable αKG (α-ketoglutarate) for indicated time points. Cell number is relative to day of treatment (day 0) per condition. Data are the mean of three biological replicates, and error bars represent s.e.m. $P < 0.005$ [***], Student's t-test. **c)** Relative integrated peak intensities for TCA cycle-related metabolites. Data are the mean of three biological replicates, and error bars represent s.e.m. $P < 0.05$ [*], $P < 0.01$ [**], $P < 0.005$ [***], Student's t-test. **d)** Relative integrated peak intensities for pentose phosphate pathway metabolites. R5P (ribose-5-phosphate); S7P (sedoheptulose-7-phosphate); E4P (erythrose-4-phosphate). Data are the mean of three biological replicates, and error bars represent s.e.m. $P < 0.05$ [*], $P < 0.005$ [***], Student's t-test. **e)** Relative integrated peak intensities for IMP (inosine monophosphate) and UMP (uridine monophosphate). Data are the mean of three biological replicates, and error bars represent s.e.m. $P < 0.01$ [**], Student's t-test. **f)** Schematic for how PHGDH regulates glucose carbon flux control (left) and effects on these flux controls upon its inhibition (right). TCA (TCA cycle); PPP (pentose phosphate pathway); SGOC (serine, glycine, one-carbon metabolism). Purple to yellow color scale indicates high to low relative carbon flux through a given metabolic pathway.
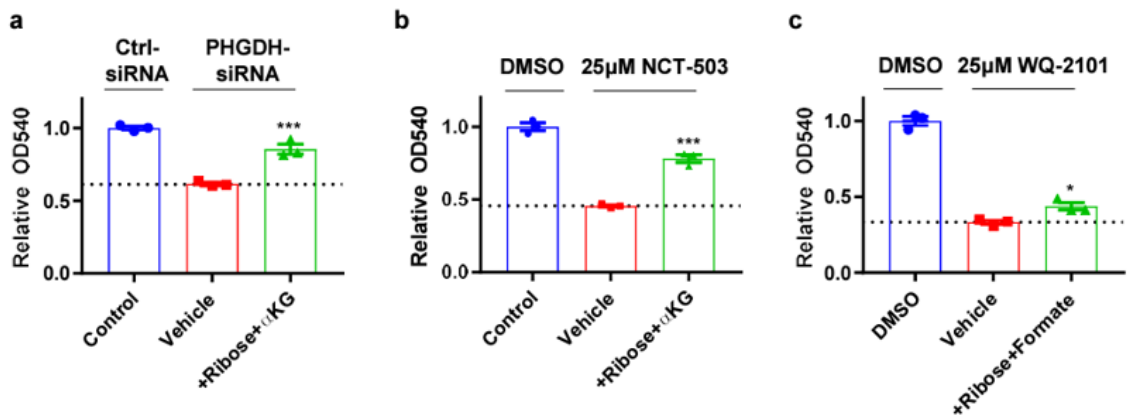
Figure 14: PHGDH siRNA and NCT-503 TCA cycle and pentose phosphate pathway rescue.

a) MTT assay of cells transfected with 20nM control siRNA or 20nM PHGDH siRNA for 48h followed by supplementation with ribose (15mM) and di-methyl α-ketoglutarate (αKG, 3mM) for 72h. OD540 values are relative to DMSO control. $P < 0.005$ [***], one-way ANOVA. b) MTT assay of cells treated with DMSO control, 25µM WQ-2101, or

25μM WQ-2101 supplemented with ribose (15mM) and dimethyl α-ketoglutarate (αKG, 3mM) for 72h. OD540 values are relative to DMSO control. P < 0.005 [***], one-way ANOVA. c) MTT assay of cells treated with DMSO control, 25μM WQ-2101, or 25μM WQ-2101 supplemented with ribose (15mM) and formate (0.5mM) for 72h. OD540 values are relative to DMSO control. P < 0.05 [*], one-way ANOVA.

2.3 Discussion

Leading up to this study, the current paradigm was that the major function of

PHGDH in proliferating cells is to maintain folate pools for nucleotide synthesis and

contribute to the glycine backbone of purines[108]. In our study, we confirmed that

PHGDH is critical for nucleotide synthesis, and defined a new mechanism by which

PHGDH contributes to and is required for nucleotide metabolism. Namely, PHGDH

regulates and is required for nucleotide metabolism by supporting the backbone of

central carbon metabolism. Thus, diversion of glycolysis into serine synthesis also

coordinates anabolic fluxes related to central carbon metabolism[200]. Notably, these fluxes

controlled by PHGDH include ribose synthesis from the pentose phosphate pathway

and the nucleobases from the TCA cycle. Supporting this model, our calculations using

metabolic flux analysis and measurements using kinetic flux profiling demonstrated that

the major fluxes affected upon PHGDH inhibition that alter nucleotide metabolism are

related to central carbon metabolism, and not the serine synthesis pathway. Our

findings are thought to be a direct mechanism of PHGDH inhibition rather than a

general consequence of reduced cell proliferation, consistent with previous reports

showing metabolic flux and metabolite availability may not coordinate with proliferation status[200,201].

Furthermore, these findings define a mechanism whereby the diversion of flux into one pathway is coupled to and thus controls numerous other pathways through long range interactions. This regulation has been in shown in other cases to occur via allosteric mechanisms[202] where changes in the concentration of metabolites in one pathway bind to enzymes and regulate the activity of other pathways. This study provides an additional example of how such a long-range regulatory mechanism in metabolism can be achieved. In this study, however, it is the mass balance and the requirement of maintaining flux balance is sufficient to regulate the flux into other neighboring anabolic pathways.

Conversely, other mechanisms have been proposed that lead to increased serine synthesis by accumulation of glycolytic intermediates[203-205]. In these scenarios, serine synthesis would serve additional biological functions by also coupling flux into related anabolic pathways. Furthermore, disruption of any of these mechanisms that push flux into serine synthesis would also affect both mitochondrial and pentose phosphate metabolism. Thus, these findings underscore the need for quantitative flux analysis to understand the metabolic requirements of altered enzyme activity, which may not be apparent from measurements of metabolite levels, and ultimately in understanding

unanticipated contexts in which targeting PHGDH might be effective in proliferative disease.

2.4 Methods

2.4.1 Cell culture and reagents

HCT116, MDA-MB-468, and MCF-7 cells were purchased from ATCC. BT-20 and MDA-MB-231 cells were kindly provided by Dr. Donald McDonnell (Duke University). SCOV3 CRISPR-Cas9 mediated PHGDH knockout cells were generated as previously described[109]. All cells were maintained in RPMI 1640 (GIBCO) supplemented with 10% heat-inactivated fetal bovine serum (Sigma, F2442) and 100 U/mL penicillin 100 mg/mL streptomycin (GIBCO). Cells were cultured in a 37 °C, 5% CO2 atmosphere. Cell lines were authenticated by their source using short-tandem repeat (STR) profiling, and tested negative for mycoplasma contamination. MCF-7 and BT-20 are listed in the ICLAC database of commonly misidentified cells; the use of these cell lines is justified by STR profiling authentication and their respective PHGDH levels (Fig. 1c). For isotope tracing experiments, dialyzed fetal bovine serum (Thermo Fisher Scientific, 88440) was substituted for fetal bovine serum upon administration of the isotope-containing medium. WQ-2101 was synthesized as previously described[109]. Sodium DL-lactate (71720), Sodium α-Ketobutyrate (K0875), Dimethyl-α-ketoglutarate (cell-permeable α-ketoglutarate) (349631), N-Acetyl-L-cysteine (A9165), D-Ribose (R9629), and NCT-503 (SML1659) were purchased from Sigma. Formic acid was purchased from Fischer

Scientific (A117). Sodium pyruvate was purchased from Santa Cruz Biotechnology (sc-208397A). EmbryoMax Nucleosides was purchased from Millipore (ES-008-D). U-13C-glucose and U-13C-glutamine were purchased from Cambridge Isotope Laboratories (CLM-1396-10 and CLM-1822-H-PK).

2.4.2 MTT and proliferation assays

MTT (3-[4,5-Dimethylthiazol-2-yl]-2,5-diphenyltetrazolium bromide) was purchased from Thermo Fisher Scientific (M6494). Cells were seeded at a density of 2-5×10^3 cells per well in 96-well plates and allowed to adhere for 24 h prior to treatment. Following treatment, medium was carefully aspirated and replaced with 100 μL of 0.5 mg/mL MTT solution in phenol red-free RPMI 1640 (GIBCO) and incubated at 37 °C for 1.5 h. Following incubation, MTT solution was carefully removed and 200 μL DMSO was added to dissolve the formazan. Absorbance was recorded at 540 nm. For proliferation assays, cells were seeded at a density of 2.5×10^4 cells per well in 12-well plates and allowed to adhere for 24 h prior to treatment. Cells were then counted for each condition (day 0) prior to administration of indicated treatments, followed by cell counting at indicated time points using a MOXI Z automated cell counter (Orflo).

2.4.3 Immunoblotting

Cells were lysed in RIPA buffer (VWR International) containing freshly added protease inhibitor complex (Roche). 20 μg of protein was loaded on precast NuPAGE Bis-Tris gels (Thermo Fisher Scientific) followed by transfer onto nitrocellulose.

Chemiluminescent signals were detected with Western Lighting Plus-ECL (Perkin Elmer, NEL103001) and imaged with the ChemiDoc Touch Imaging System (Bio-Rad). Anti-PHGDH antibody was purchased from Sigma (WH0026227M1), and was used at 1:1000 dilution. Anti-β-ACTIN antibody was purchased from Cell Signaling (3700S), and was used at 1:2000 dilution.

2.4.4 Microscopy

Cells were seeded at a density of 2–5 × 10^3 cells per well in 96-well plates and allowed to adhere for 24 h prior to treatment. Following treatment, medium was replaced with 1× PBS prior to imaging. Images were captured using a Leica DM IL LED microscope equipped with a Leica MC170HD camera at ×10 objective using LAS EZ software (Leica). Scale bars = 100 μm.

2.4.5 siRNA transfections

ON-TARGETplus Non-targeting control siRNA (D-001810-01-05) and SMARTpool ON-TARGETplus siRNA oligonucleotides targeting human *PHGDH* (L-009518-00) were purchased from Dharmacon. siRNA transfections were performed using Lipofectamine RNAiMAX (Thermo Fisher Scientific) according to the manufacturer's protocol. Experiments were performed 72 h post transfection.

2.4.6 Metabolite extraction

Polar metabolite extraction was conducted as previously described[17,206]. Briefly, 1.5–3 × 10^5 cells per well were seeded into six-well plates and allowed to adhere for 24 h

prior to treatment. Cell confluence was equal across conditions at the time of extraction.

Following treatment, medium was aspirated and 1 mL of extraction solvent (80%

methanol/water) cooled to −80 °C was immediately added to each well prior to

transferring the plates to −80 °C for 15 min. The plates were then removed, placed on dry

ice, and the cells were scraped into the extraction solvent and transferred to Eppendorf

tubes. Metabolite extractions were centrifuged at 20,000 × g at 4 °C for 10 min. The

solvent in each sample was then transferred to a new Eppendorf tube and evaporated

using a speed vacuum. For polar metabolite analysis, the evaporated cell extracts were

first dissolved in 15 μL water and then diluted with 15 μL methanol/acetonitrile (1:1

v/v). Finally, samples were centrifuged at 20,000 × g at 4 °C for 10 min, and the

supernatants were transferred to LC vials prior to HPLC injection (3 μL).

2.4.7 High-performance liquid chromatography

Compound separation was performed using an XBridge amide column

(100 × 2.1 mm i.d., 3.5 μm; Waters) on a Dionex Ultimate 3000 UHPLC at room

temperature. Mobile phase A: water with 5 mM ammonium acetate, pH 6.9; Mobile

phase B: 100% acetonitrile. The following linear gradient was used: 0 min, 85% B;

1.5 min, 85% B; 5.5 min, 35% B; 10 min, 35% B; 10.5 min, 10% B; 12.5, 10% B; 13.5 min,

85% B; 20 min, 85% B. Flow rate was 0.15 ml/min from 0 to 5.5 min, 0.17 ml/min from 6.9

to 10.5 min, 0.3 ml/min from 10.6 to 17.9 min, and 0.15 ml/min from 18 to 20 min. All

solvents used were LC-MS grade, and were purchased from Fisher Scientific.

2.4.8 Mass spectrometry

Mass spectrometry was performed using the Q Exactive plus (Thermo Scientific) instrument as previously described[17,206]. The Q Exactive Plus MS is equipped with a heated electrospray ionization probe (HESI) and the relevant parameters are as follows: evaporation temperature, 120 °C; sheath gas, 30; auxiliary gas, 10; sweep gas, 3; spray voltage, 3.6 kV for positive mode and 2.5 kV for negative mode. Capillary temperature was set at 320 °C, and S lens was 55. A scan range from 70 to 900 (m/z) was used. Resolution was set at 70,000. The maximum injection time was 200 ms, and the automated gain control was targeted at 3×106 ions.

2.4.9 Metabolite peak extraction and data analysis

Raw peak data was processed on Sieve 2.0 software (Thermo Scientific) with peak alignment and detection performed according to the manufacturer's protocol. The method "peak alignment and frame extraction" was applied for targeted metabolite analysis. An input file of theoretical m/z and detected retention time was used for targeted metabolite analysis, and the m/z width was set to 5 ppm. An output file was obtained after data processing that included detected m/z and relative intensity in the different samples. For isotope tracing experiments, the mass isotopomer distributions were calculated and normalized by comparing the ratio of labeled to unlabeled metabolites in each sample. For ribose and αKG rescue experiments, peak intensities for ribose + αKG + inhibitor were normalized to ribose + αKG + vehicle. Metabolite pathway

58

impacts were determined by MetaboAnalyst pathway analysis [www.metaboanalyst.ca] using the following parameters: Over Representation Analysis- Hypergeometric Test; Pathway Topology Analysis- Relative-betweeness Centrality. Volcano plots were generated using GraphPad Prism 7.

2.4.10 Metabolic flux analysis

A metabolic model including 19 reactions and 21 metabolites in pentose phosphate pathway, serine synthesis, TCA cycle and nucleotide synthesis pathway was used. Biomass synthesis was modeled based on literature values for molecular composition of dry cell weight[207]. The model was then converted to elementary metabolite units (EMUs)[208] according to the stoichiometry and carbon atom mapping relationships. The EMU model was used in estimation of the fluxes from mass isotopomer distributions (MIDs) of metabolites measured by LC-HRMS. Flux ratios were solved from MIDs of metabolites at the branch points. Metabolic fluxes relative to growth rate were then solved analytically from the combination of flux ratios at branch points and the stoichiometric matrix. Mean and standard deviation values were computed based on fluxes estimated from three biological replicates. Construction of the metabolic flux analysis model is reported in Reid et al. (2018).

2.4.11 Statistics

All experiments contained three biological replicates. Results shown as means; error bars represent the standard error of the mean. The unpaired Student's t-test was

used to determine statistical significance of differences between means (P < 0.05 [*],

P < 0.01 [**], P < 0.005 [***]) unless otherwise stated.

2.4.12 Code availability

Source code for the metabolic flux analysis model is available on GITHUB via

https://github.com/LocasaleLab/Reid-et-al-2018.

2.5 Author Contributions

This chapter is from a collaborative study. Annamarie Allen assisted the lead

author of the study, Michael Reid, with collecting experimental data, data analysis, and

figure presentation and organization. Specifically, Annamarie contributed significantly

to the nucleoside rescue experiments shown in Figures 3 and 4, analysis of the tracing

data shown in Figures 6, 7, and 10, and creation of the Schematic shown in Figure 13.

3. Evolved resistance to partial GAPDH inhibition results in loss of the Warburg effect and a different state of glycolysis[iv]

3.1 Background and Context

As discussed in Chapter 1.3.1.1, inhibition of the glycolytic enzyme GAPDH is a

selective way to disrupt metabolism in cancer cells that are heavily reliant on the

Warburg Effect. The natural product koningic acid (KA) is a selective GAPDH

inhibitor[17,209], and use of this compound not only offers a potential cancer therapy, but

also a useful tool for studying the properties of the Warburg Effect. Whether glucose

metabolism is functionally different during fully oxidative glycolysis or during the WE

is unknown, so my colleagues and I used KA to investigate this question. To do this, we

evolved resistance to KA in a high-WE cell line, and examined what aspects of global

metabolism changed. We found that KA-resistant cells lose the WE but continue to

conduct glycolysis and surprisingly remain dependent on glucose as a carbon source.

Consequently, this altered state of glycolysis led to differential metabolic activity and

requirements, including emergent activities in and dependences on fatty acid

---

metabolism. These findings reveal that aerobic glycolysis is a process functionally distinct from conventional glucose metabolism and leads to distinct metabolic requirements and biological functions.

3.2 Results

3.2.1 GAPDH inhibition leads to different phenotypic outcomes from targeting glucose uptake

We first sought to determine whether disrupting GAPDH activity results in different outcomes from other perturbations to glycolysis. Because GAPDH has differential rate control in cells undergoing the WE (i.e. high glucose uptake and lactate secretion)[17], we used a high-WE cell line, BT-549, and compared inhibition of GAPDH with KA with inhibition of glucose uptake and deprivation of glucose from the culture medium (Fig. 15A). First, we measured the IC50 of E11, a validated, highly potent inhibitor of GLUT-1 and thus glucose uptake[210] (Fig. 16A). We then compared cell viability of BT-549 treated with doses of KA above and below the known IC50[17] and/or E11. We found that co-treatment of KA and E11 caused a greater significant decrease in cell viability than treatment with either compound alone (Fig. 15B).

We further found significant changes between KA-treated cells and cells cultured in glucose-deprived medium (Fig. 15C). To assess these differential effects on cells at a metabolic level, we used LC coupled to high-resolution MS (LC-HRMS)-based metabolomics, which revealed gross differences in global metabolism when comparing KA-treated BT-549 cells with glucose-deprived cells (Fig. 15D). An analysis of glycolysis

indicated an accumulation of glycolytic intermediates upstream and depletion of those

downstream of GAPDH in cells treated with KA, whereas glucose-deprived conditions

revealed an overall depletion of metabolites throughout glycolysis (Fig. 15E). Thus, cells

exhibit a differential metabolic response to GAPDH inhibition compared with other

modes of glycolysis inhibition. These findings raise the possibility that cells utilize and

rely on the WE differently from glycolysis, providing rationale that the WE is different

from other forms of glucose metabolism.
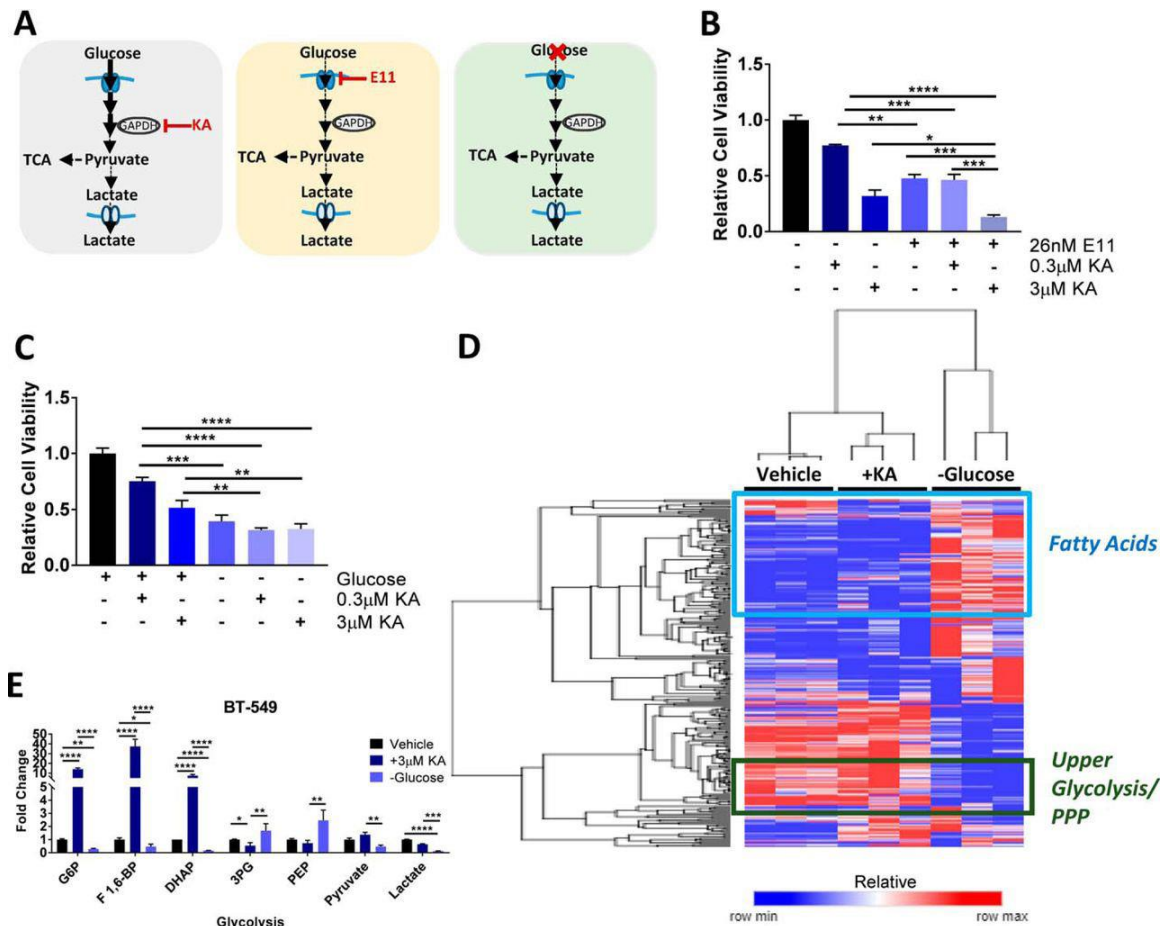
Figure 15: GAPDH inhibition leads to different phenotypic outcomes from targeting glucose uptake.

A) Schematic representing the comparison of KA treatment with glucose transporter-1 (GLUT-1) inhibition with E11 or deprivation of glucose from the growth medium. B) Cell viability of BT-549 breast cancer cells treated with E11 (26 nm) with or without KA (0.3 or 3 μm) after 24 h. *, $p < 0.05$; **, $p < 0.01$; ***, $p < 0.001$; ****, $p < 0.0001$ as determined by one-way ANOVA. C) cell viability of BT-549 breast cancer cells cultured in complete or glucose-restricted medium and treated with or without KA (0.3 or 3 μm) after 24 h. *, $p < 0.05$; **, $p < 0.01$; ***, $p < 0.001$; ****, $p < 0.0001$ as determined by one-way ANOVA. D) hierarchical clustered heat map quantile-normalized of BT-549 cells with condition annotations of global metabolic responses to vehicle, 3 μm KA, or glucose-restricted conditions for 6 h with annotations of metabolic pathways. The scale represents 0 to 1 for row minimum and row maximum, respectively, after quantile normalization. E, BT-549 glycolysis profile for vehicle, KA, or glucose-restricted conditions for 6 h. G6P, glucose 6-phosphate; F 1,6-BP, fructose 1,6 bisphosphate; DHAP, dihydroxyacetone phosphate; 3PG, 3-phosphoglycerate; PEP, phosphoenolpyruvate. All data are represented as mean ± S.E. (error bars) from n = 3 biological replicates. *, $p < 0.05$; **, $p < 0.01$; ***, $p < 0.001$; ****, $p < 0.0001$ as determined by two-way ANOVA unless otherwise indicated.

3.2.2 Cells evolve resistance to GAPDH inhibition independent of drug metabolism

To investigate whether glycolysis exists in different biological states from the WE, we hypothesized that cells could transition from the WE to another state of glucose metabolism when faced with a selective pressure against maintaining glycolysis in a certain state. Given that KA was previously shown to be selectively toxic to cells undergoing the WE, we suspected that it could be a useful tool to investigate this concept. We cultured BT-549 cells with incrementally increasing concentrations of KA and monitored their growth rate over a period of 20 weeks with parental cells maintained in cell culture in parallel (Fig. 16, A and B). The specific growth rate of parental cells measured after 1 week in culture was recorded as 0.0173 h^{-1} and was used as the week 0 baseline measurement for beginning KA treatment for acquired resistance.

Three clonal cell populations that developed resistance to KA exhibited growth rates between 0.0022 and 0.0058 h⁻1. These were isolated and maintained in 3 μm KA for the remainder of the study (BT-549(R)1–3) (Fig. 16C). IC50 values for KA in each of these clones were found to be greater than 200 μm compared with the parental cells that exhibited an IC50 of ~1 μm KA (Fig. 16D).

For this system to be an effective model for evolving a transition out of the WE, it was necessary to first confirm that resistance to KA was not occurring due to mechanisms outside of cellular metabolism. There are several known pharmacological mechanisms that are commonly implicated in drug resistance that include alterations in drug metabolism and target disengagement[211]. To test for altered drug metabolism, such as a difference in drug efflux, we used LC-HRMS to measure intracellular concentrations of KA in BT-549 sensitive and acquired resistant cells as well as in MCF-7 KA-intrinsic resistant cells (Fig. 16E). Intracellular concentrations of KA in BT-549 acquired resistant cells maintained in 3 μm KA remained consistent with concentrations detected in BT-549 parental and MCF-7 intrinsic resistant cells that were treated with 3 μm KA (Fig. 16F and Fig. 17A). We also found similar intracellular concentrations of KA between BT-549 parental and acquired resistant cells at different time points following culture of cells with KA (Fig. 17 B–D). Together, these data confirm that drug efflux is not contributing to acquired resistance to KA in these cells.

To verify that KA was still engaging its target (i.e. the catalytic site of

GAPDH)[209,212], we carried out a GAPDH activity assay in the presence or absence of KA

and found that KA maintains target engagement through decreasing GAPDH activity in

BT-549 acquired resistant cells comparable with that of BT-549 parental cells (Fig. 16G

and Fig. 17 E and F) and MCF-7 cells (Fig. 17G). In support of these findings, we

observed little difference in GAPDH protein expression between BT-549 parental and

acquired resistant cells (Fig. 17H). We also found that acquired resistant cells can

become resensitized to KA upon KA removal for 2 weeks, followed by the addition of

KA again (Fig. 17I), further arguing against an inability to maintain target engagement.

Together, these data indicate that acquired resistant cells retain normal KA drug

metabolism properties with continued target engagement at the active site of GAPDH.

Thus, independent of drug pharmacology, biological mechanisms related to glucose

metabolism may underlie the resistance to GAPDH inhibition.
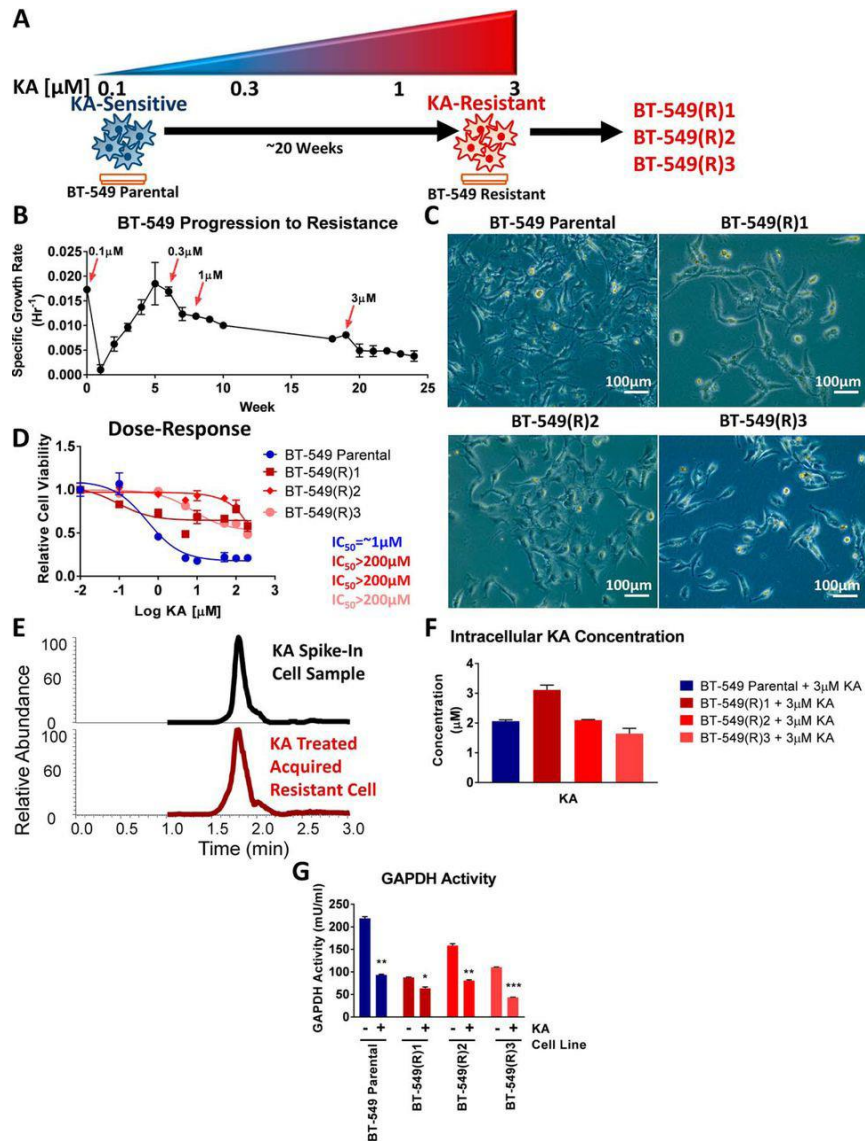
Figure 16: Cells evolve resistance to GAPDH inhibition independent of drug metabolism.

A) schematic representing progression to acquired resistance model of BT-549 cells. After 20 weeks of incrementally increasing doses of KA, clonal populations of acquired resistant cells were isolated and maintained in 3 µm KA for the duration of the study. B) recorded growth rates of BT-549 cells during the 20-week period of progression to acquired resistance. C) representative images of BT-549 parental (top left) and three clonal acquired resistant cells (top right, bottom row). D) cell viability of BT-549 parental and acquired resistant cells treated with 0–200 µm KA and reported IC50 values. E) mass spectra of KA in a spiked sample and KA-treated acquired resistant cells using LC-MS with a representative sample. F) intracellular KA concentrations from BT-549

parental and acquired resistant cells treated with 3 μm KA. G, relative GAPDH activity in BT-549 parental and acquired resistant cells in response to vehicle or 3 μm KA (n = 2).

All data are represented as mean ± S.E. (error bars) from n = 3 biological replicates unless otherwise indicated. *, p < 0.05; **, p < 0.01; ***, p < 0.001; ****, p < 0.0001 as determined by multiple t tests.
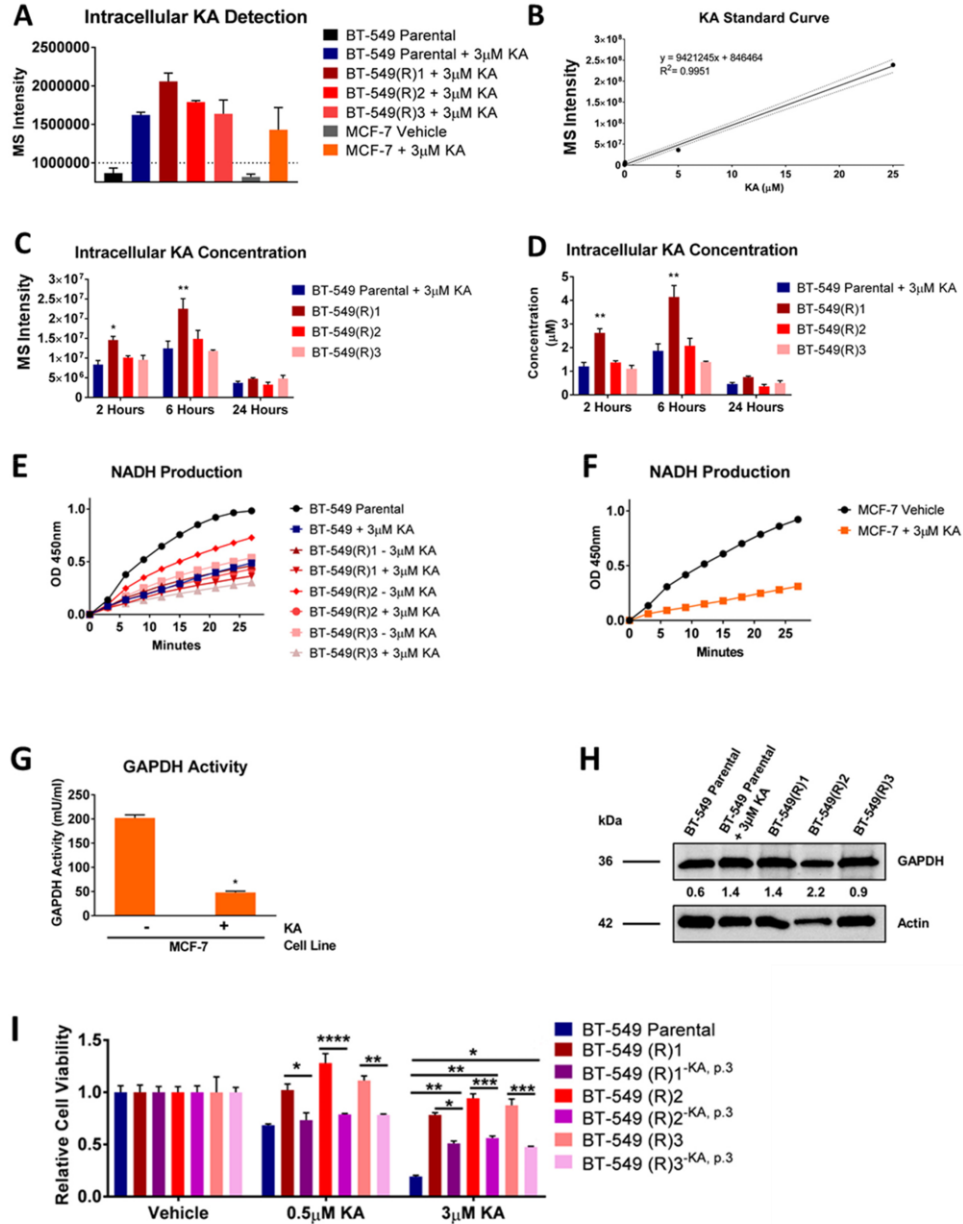
Figure 17: Supplemental-Cells evolve resistance to GAPDH inhibition independent of drug metabolism.

68

A) Mass spectrometry intensities of intracellular KA in vehicle or KA (3µM) treated cells using liquid chromatography-mass spectrometry (LC-MS). Dotted line denotes noise level. B) Standard curve of KA spiked into untreated BT-549 parental cells. C) MS intensity values of KA concentrations after treatment with vehicle or 3µM KA for 2, 6, and 24 hours. D) Absolute intracellular KA concentrations after treatment with vehicle or 3µM KA for 2, 6, and 24 hours. E) Relative NADH production from 0-27 minutes in kinetic mode of BT-549 parental and acquired resistant cells with and without KA (3µM) treatment (n=2). F) Relative NADH production of MCF-7 cells as in (B) (n=2). G) Relative GAPDH activity in MCF-7 cells in response to vehicle or 3µM KA (n=2). *p<0.05, **p<0.01, ***p<0.001, ****p<0.0001 as determined by Student's t-test. H) Immunoblotting of GAPDH in BT-549 parental and acquired resistant cells with quantitation normalized to actin. I) BT-549 acquired resistant cells were passed either with KA or without KA (as indicated by superscript -KA, p.3) for 3 passages (a total of 2 weeks). After 2 weeks, cells were treated with vehicle, 0.5µM KA, or 3µM KA and compared to BT-549 parental cells.

All data are represented as mean ± SEM from n=3 biological replicates unless otherwise indicated. *p<0.05, **p<0.01, ***p<0.001, ****p<0.0001 as determined by Two-Way ANOVA unless otherwise indicated.

3.2.3 Acquired resistant cells lose the Warburg effect but remain dependent on glycolysis

Using our evolved resistance model to the glycolytic enzyme GAPDH, we

sought to determine whether these cells continue to undergo the WE. We treated BT-549

acquired resistant cells with KA and found that acquired resistant cells still undergo

glycolysis marked by increases in fructose 1,6-bisphosphate compared with untreated

BT-549 parental, which are indicative of slower rates of glycolysis[16,213] and decreases in

lactate levels compared with parental cells, suggestive of a lower WE (Fig. 18A).

Interestingly, we also found that acquired resistant cells exhibited similar or lower levels

of pentose phosphate pathway metabolites compared with parental cells (Fig. 20, A–D).

Because low lactate levels were detected in the acquired resistant cells compared with parental cells, we next sought to examine lactate production from glucose carbon using uniformly labeled [U-^{13}C]glucose in BT-549 parental and acquired resistant cells. We observed decreased lactate production in the acquired resistant cells compared with untreated parental cells at levels comparable with the lactate production observed in the parental cells treated with 3 μm KA (Fig. 18B and Fig. 20E). In addition, we measured intracellular glucose and lactate levels in parental and acquired resistant cells (Fig. 20F). As expected, parental and acquired resistant cells exhibited similar intracellular glucose levels, indicative of similar glucose uptake. Parental and acquired resistant cells had similar intracellular lactate levels, which we reasoned was likely due to the majority of lactate produced by cells being immediately secreted out of cells and into the environment[4,214]. Indeed, upon measuring excreted lactate from cells in spent medium from 0 to 6 h, we found significantly less excreted lactate from BT-549 acquired resistant cells compared with parental cells treated with either vehicle or KA, with a similar finding after 24 h (Fig. 18 (C and D) and Fig. 20G). In addition, the decreases in lactate levels were not immediately reversible upon removal of KA (Fig. 20H). Quantitative measurements of the WE via relative lactate flux calculations revealed lower lactate flux (i.e. low WE) in acquired resistant cells compared with parental cells, with a lactate flux value comparable with the low glycolytic cell line, MCF-7 (Fig. 20I). Together, these data indicate that acquired resistant cells evolved a loss of the WE.

70

Because acquired resistant cells no longer undergo the WE, we asked whether they remained dependent on glucose uptake and depend on glycolysis for survival, because previous studies have indicated that cells are either glycolysis-dependent or -independent[215,216]. We reasoned that if these cells do continue to rely on glycolysis, which would be different from WE or non-WE cells, then another glycolytic state could have emerged. We treated the acquired resistant cells with E11 and/or KA and determined cell viability. Whereas these cells remained resistant to KA as expected, we surprisingly observed differences in sensitivity upon treatment with E11 in combination with KA (Fig. 18E). To further investigate this differential dependence on glycolysis, we studied the response to glucose deprivation. After 24 h of culture in glucose-deprived growth medium and KA, we found that the viability of BT-549 acquired resistant cells decreased compared with cells cultured in full growth medium and maintained in KA (Fig. 18F). In addition, metabolite profiling of BT-549 acquired resistant cells in glucose-deprived growth medium compared with those maintained in 3 μm KA revealed global differences in overall metabolic levels (Fig. 19). Together, these data indicate that BT-549 acquired resistant cells no longer exhibit or require the WE but remain dependent on glycolysis for survival.

Interestingly, we further found that acquired resistant cells displayed decreased fraction labeling and carbon contribution from glucose through glycolysis, decreased fraction labeling with a small increase in carbon contribution from glucose through the

pentose phosphate pathway, and decreased fraction labeling and carbon contribution

through the citric acid (TCA) cycle (Fig. 20, J–T). Taken together, these data further

clarify the existence of multiple states of glucose metabolism.
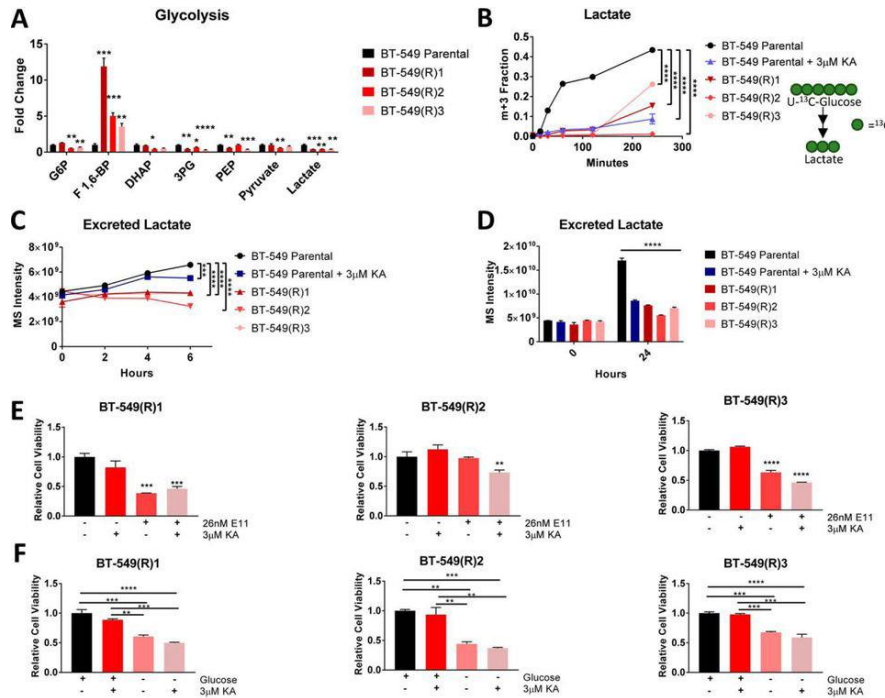
Figure 18: Acquired resistant cells lose the Warburg effect but remain dependent on glycolysis.

A) glycolytic metabolite levels measured after 6 h. All glycolysis metabolite levels measured from parental cells were normalized to 1. All glycolysis metabolite levels measured from acquired resistant cells are normalized to parental cell levels. *, $p < 0.05$; **, $p < 0.01$; ***, $p < 0.001$; ****, $p < 0.0001$ as determined by multiple t tests. B) [^{13}C]lactate from [U-^{13}C]glucose in BT-549 parental treated with vehicle or 3 µm KA and acquired resistant cells for 0–4 h. C) excreted lactate detected in medium from 0 to 6 h. D) excreted lactate detected in medium after 24 h. E) cell viability of BT-549 acquired resistant cancer cells treated with E11 (26 nm) with or without KA (3 µm) after 24 h. *, $p < 0.05$; **, $p < 0.01$; ***, $p < 0.001$; ****, $p < 0.0001$ as determined by one-way ANOVA. F) cell viability of BT-549 acquired resistant cancer cells cultured in complete or glucose restricted medium and treated with or without KA (3 µm) after 24 h. *, $p < 0.05$; **, $p < 0.01$; ***, $p < 0.001$; ****, $p < 0.0001$ as determined by one-way ANOVA.

All data are represented as mean ± S.E. (error bars) from n = 3 biological replicates. *, p < 0.05; **, p < 0.01; ***, p < 0.001; ****, p < 0.0001 as determined by two-way ANOVA unless otherwise indicated.
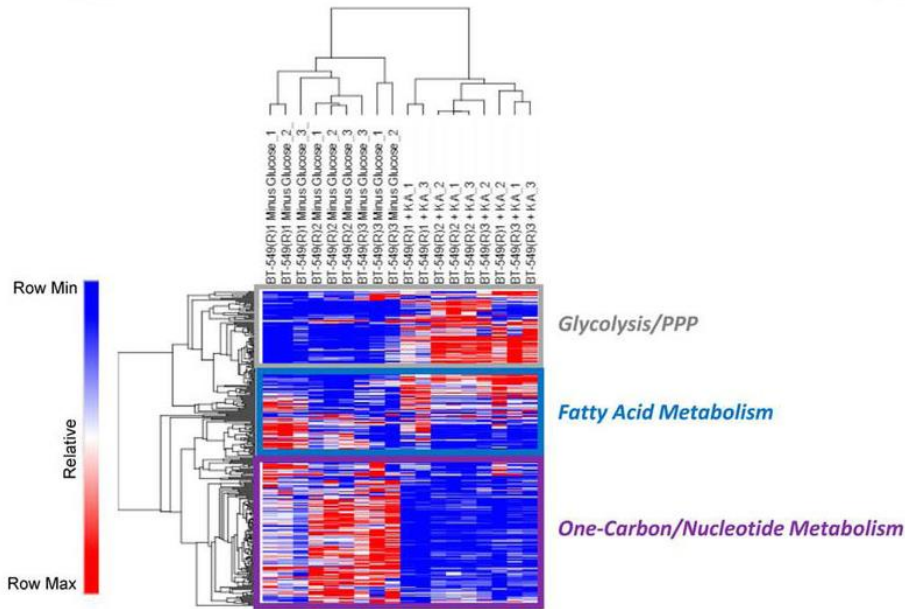
Figure 19: Hierarchical Clustering-Acquired resistant cells lose the Warburg effect but remain dependent on glycolysis

Hierarchical clustered heat map quantile-normalized of BT-549 cells with condition annotations of global metabolic responses to vehicle, 3 μm KA, or glucose-restricted conditions for 6 h with annotations of metabolic pathways. The scale represents 0 to 1 for row minimum and row maximum, respectively, after quantile normalization. G6P, glucose 6-phosphate; F 1,6-BP, fructose 1,6-bisphosphate; DHAP, dihydroxyacetone phosphate; 3PG, 3-phosphoglycerate; PEP, phosphoenolpyruvate.
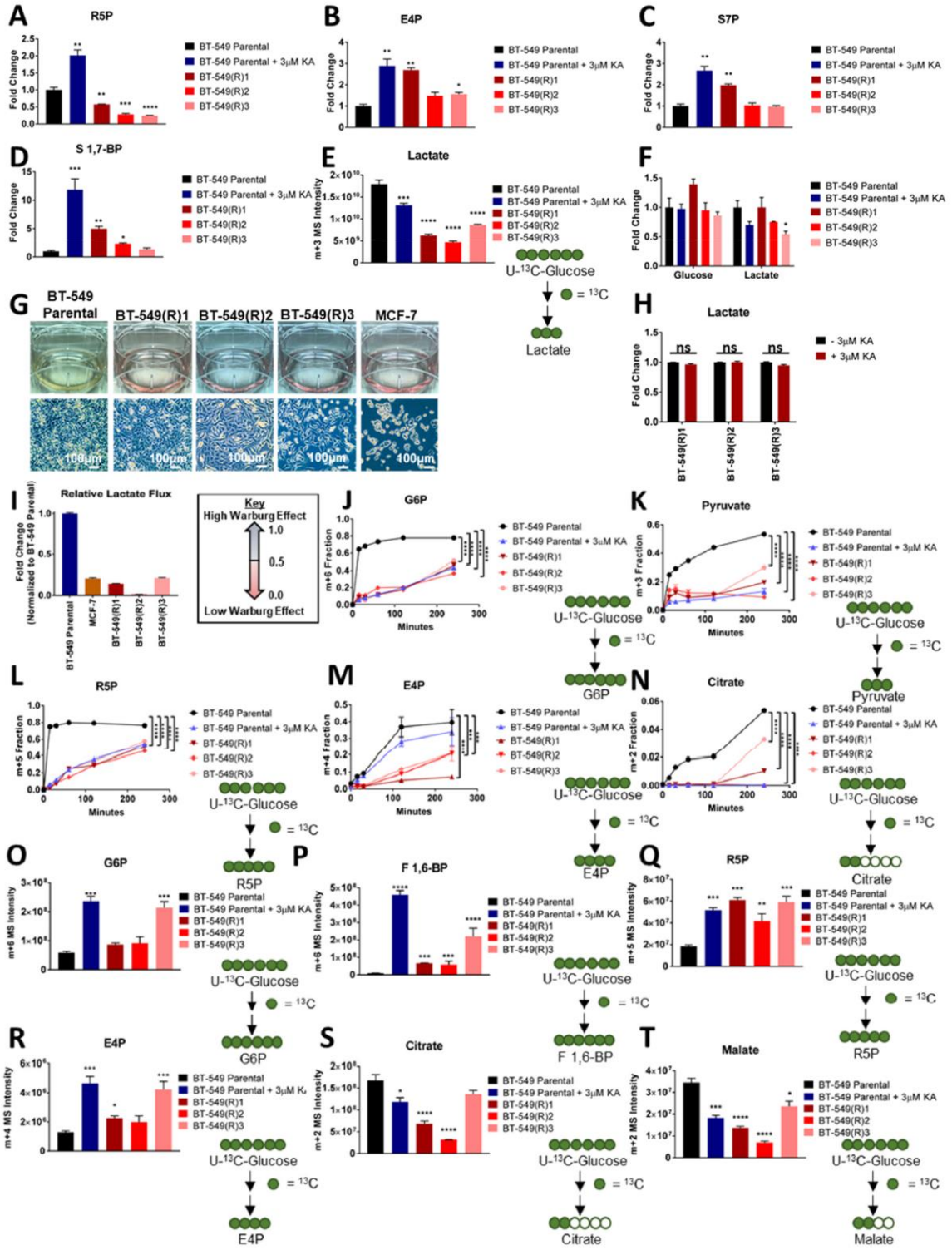
Figure 20: Supplemental-Acquired resistant cells lose the Warburg effect, but remain dependent on glycolysis

A) R5P levels in BT-549 parental and acquired resistant cells treated with vehicle or KA for 6 hours. B) E4P as in A. C) S7P as in A. D) S 1,7-BP as in A. E) MS intensity of ^{13}C-lactate in BT549 parental and acquired resistant cells treated with vehicle or KA for 6 hours followed by U-13C-glucose labeling for 24 hours. F) Levels of intracellular glucose and lactate in BT-549 parental and acquired resistant cells after 6 hours. G) Representative images of spent media (top row) and cells (bottom row) at confluency in BT-549 parental, BT-549 acquired resistant, and MCF-7 intrinsic resistant cells after 48 hours. H) Lactate levels in BT-549 acquired resistant cells upon removal or maintained in KA (3µM) KA after 24 hours. Not significant denoted as "ns" determined by multiple t-tests. I) Relative lactate flux calculated for BT-549 parental and acquired resistant cells as well as in MCF-7 cells. Value are normalized to lactate flux of BT-549 parental cells. Key denotes low to high Warburg effect and respective values. J) 13C-G6P in BT-549 parental and acquired resistant cells treated with vehicle or KA for 0-4 hours. K) ^{13}C-pyruvate as in J. L) ^{13}C-R5P as in J. M) ^{13}C-E4P as in J. N) ^{13}C-citrate as in J. O) ^{13}C-G6P as in E. P) ^{13}C-F1,6-BP as in E. Q) ^{13}C-R5P as in E. R) ^{13}C-E4P as in E. S) ^{13}C-citrate as in E. T) ^{13}C-malate as in E. G6P, glucose-6-phosphate; F 1,6-BP, fructose 1,6-bisphosphate; R5P, ribose-5-phosphate; E4P, erythrose-4-phosphate; S7P, sedoheptulose-7-phosphate; S 1,7-BP, sedoheptulose 1,7bisphosphate. All data are represented as mean ± SEM from n=3 biological replicates. *p<0.05, **p<0.01, ***p<0.001, ****p<0.0001 as determined by Two-Way ANOVA unless otherwise indicated.

3.2.4 Changes in fatty acid metabolism emerge as a functional output of evolved resistance to KA

Our data thus far indicate a transition from the utilization of the WE to loss of the WE in cells with acquired resistance to KA with changes in glucose metabolism. To understand the temporal dynamics of metabolism that result in the observed change in state of glucose metabolism, we extracted metabolites from cells at different times over the 20-week time course during progression to resistance and compared their metabolite levels with those of parental cells treated with the corresponding doses of KA (Fig. 21A). Metabolite profiling revealed global differences, with glycolysis most prominently affected in the parental cells and changes to fatty acid, one-carbon, and nucleotide

75

metabolism most apparent in acquired resistant cells (Fig. 21, B and C). Over half of the common changes in each of the clones relative to the parental cells were related to fatty acid metabolism (Fig. 21D), including small and variably significant increases in fatty acid levels (Fig. 22, A–C).

Given the common changes to fatty acid metabolism and our findings that acquired resistant cells are utilizing glucose carbon differently from parental cells, we asked whether other carbon sources, such as glutamine, account for the observed differences (Fig. 22D). Interestingly, we found small but significant increases in the fraction labeled from glutamine through the TCA cycle, indicating that acquired resistant cells fuel their TCA cycle, at least in part, by glutamine (Fig. 22, E–I). Next, we analyzed whether partial increases in fatty acid levels in acquired resistant cells result from carbon contribution by glucose, glutamine, and/or palmitate and found small contributions of each of these carbon sources to representative fatty acid metabolites (Fig. 22, J–Q). We then asked whether removal of lipids from the extracellular environment differentially affects acquired resistant cell survival (Fig. 22R). We found no significant differences compared with parental cells, likely due to extracellular lipids not being a major carbon contributor in acquired resistant cells (Fig. 22, S–U). Together, these data demonstrate differences in fatty acid metabolism in acquired resistant cells with variable contributions from different carbon sources compared with parental cells.
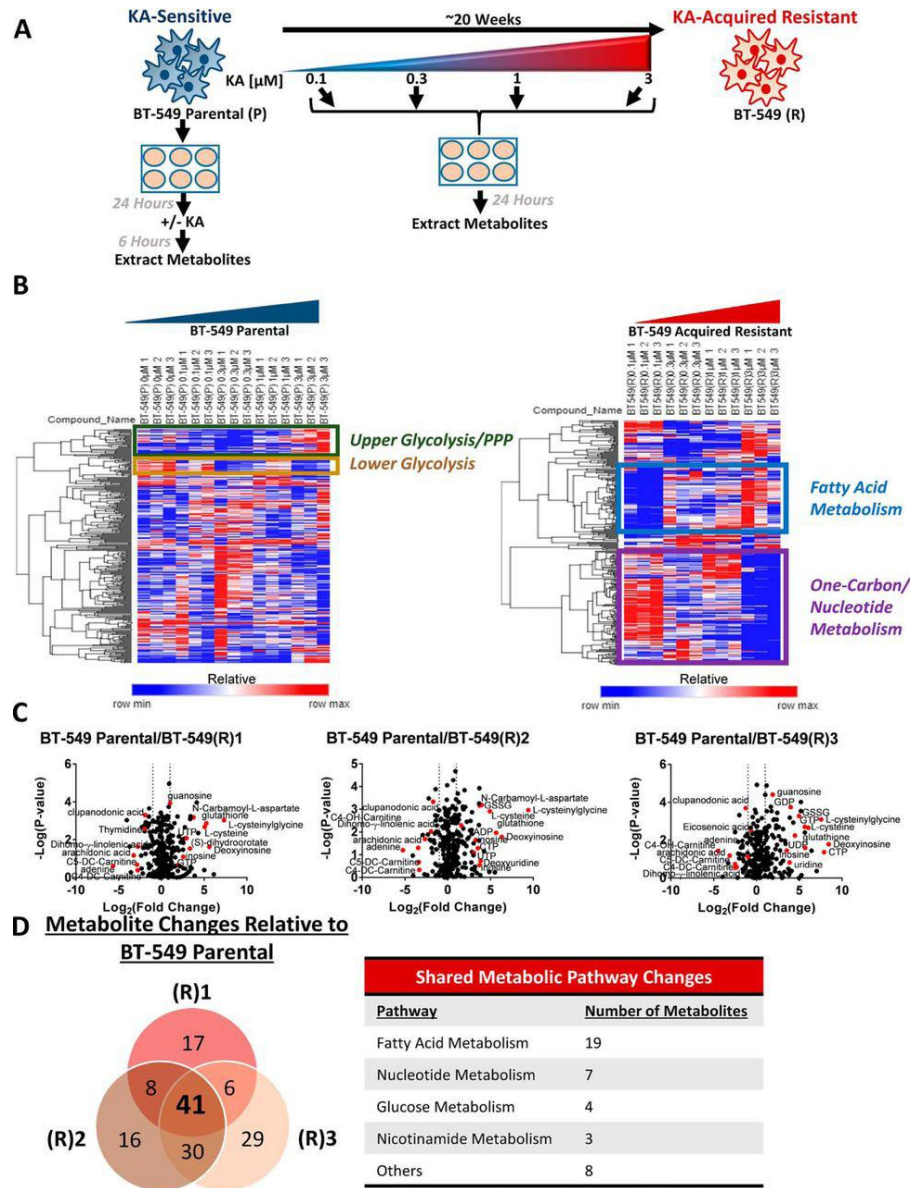
Figure 21: Changes in fatty acid metabolism emerge as a functional output of evolved resistance to KA.

A) schematic of experimental setup for metabolomics during evolution to acquired resistance to KA. Metabolites from parental cells were extracted after 6 h of treatment with 0–3 μm KA. Metabolites from KA-acquired resistant cells were extracted over the 20-week progression to resistance period upon resistance to the depicted doses. B) hierarchical clustered heat maps quantile-normalized. Shown is a heat map depicting detected metabolites from parental cells treated with 0–3 μm KA for 6 h (left) and a heat

map depicting detected metabolites as cells acquire resistance to 0–3 μm KA over 20 weeks (right). Heat maps show annotations of metabolite pathways. The scale represents 0 to 1 for row minimum and row maximum, respectively, after quantile normalization. C) volcano plots showing metabolite profiles of BT-549 acquired resistant cells maintained in 3 μm KA compared with BT-549 parental cells treated with vehicle. Shown is log2 -fold change versus $-\log_{10}$ p value. Dotted lines along the x axis represent $\pm\log_2(1)$ -fold change, and the dotted line along the y axis represents $-\log_{10}(0.05)$. Metabolites $\pm \log_2(1)$ -fold change are shown as red points with metabolite names denoted. All other metabolites are shown as black points. D) Venn diagram indicating the overlap of metabolic changes among KA-resistant clones based on average $\pm\log_2(1)$ -fold changes compared with BT-549 parental cells treated with vehicle. G6P, glucose 6-phosphate; F 1,6-BP, fructose 1,6-bisphosphate; DHAP, dihydroxyacetone phosphate; 3PG, 3-phosphoglycerate; PEP, phosphoenolpyruvate. All data are represented as mean ± S.E. from n = 3 biological replicates. *, $p < 0.05$; **, $p < 0.01$; ***, $p < 0.001$; ****, $p < 0.0001$ as determined by two-way ANOVA.
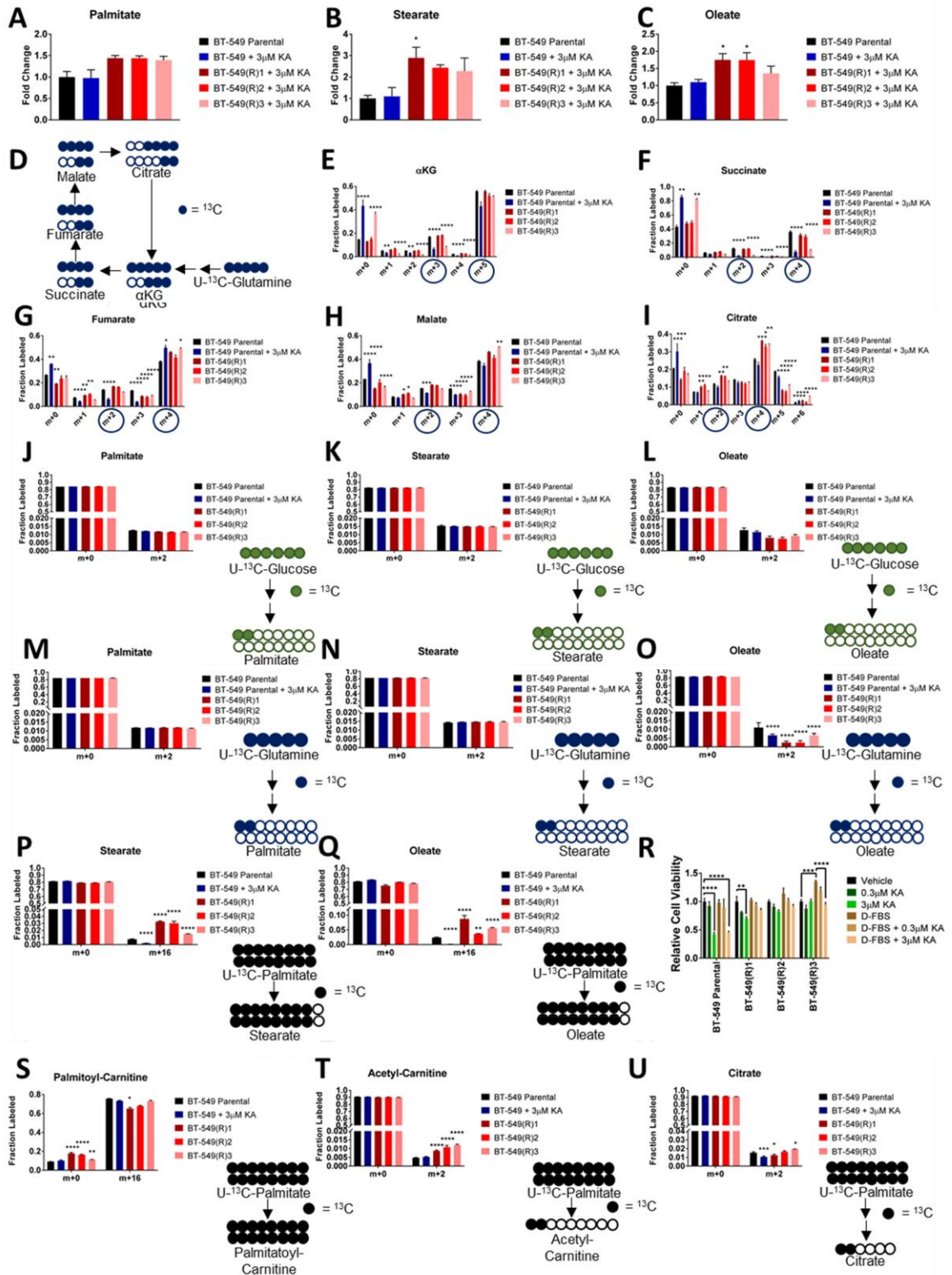
Figure 22: Changes in fatty acid metabolism emerge as a functional output of evolved resistance to KA.

A) Levels of palmitate after treatment with vehicle or KA for 6 hours. B) Stearate as in A. C) Oleate as in A. D) Schematic depicting two turns of the TCA cycle after labeling cells with U-13Cglutamine. E) Fraction labeled of ^{13}C-αKG from U-13C-glutamine labeling after pretreatment with vehicle or KA for 6 hours followed by tracing for 24 hours. Isotopomers labeled by U^{13}C-glutamine are circled in blue. F) ^{13}C-succinate as in E. G) ^{13}C-fumarate as in E. H) ^{13}C-malate as in E. I) ^{13}C-citrate as in E. J) Fraction labeled of ^{13}C-palmitate after pretreatment with vehicle or KA for 6 hours followed by U-^{13}C-glucose labeling for 24 hours. K) ^{13}C-stearate as in J. L) ^{13}C-oleate as in J. M) Fraction labeled of ^{13}C-palmitate after pretreatment with vehicle or KA for 6 hours followed by U-^{13}C-glutamine labeling for 24 hours. N) ^{13}C-stearate as in M. O) ^{13}C-oleate as in M. P) Fractions labeled of ^{13}C-stearate after pretreatment with vehicle or KA for 6 hours followed by U-^{13}C-palmitate labeling for 24 hours. Q) ^{13}C-oleate as in P. R) Cell viability of BT-549 parental and acquired resistant cells treated with vehicle or KA for 24 hours in complete media or media supplemented with 10% delipidated serum. S) Fraction labeled of ^{13}C-palmitoyl-carnitine after pretreatment with vehicle or KA for 6 hours followed by U-^{13}C-palmitate labeling for 24 hours. T) ^{13}C-acetyl-carnitine as in S. U) ^{13}C-citrate as in S. All data are represented as mean ± SEM from n=3 biological replicates. *$p<0.05$, **$p<0.01$, ***$p<0.001$, ****$p<0.0001$ as determined by Two-Way ANOVA. αKG, α-ketoglutarate.

To further probe the differences we observed in fatty acid metabolism, we used cerulenin, a fatty acid synthase inhibitor that inhibits fatty acid oxidation by increasing malonyl-CoA levels[217-219]. We observed increased sensitivity in acquired resistant cells compared with parental cells and also found no significant change in MCF-7 cells (Fig. 24, A–C). Additionally, the acquired resistant cells treated with cerulenin exhibited a differential metabolic response (Fig. 23A and Fig. 24D). Next, we asked whether cerulenin differentially affected acyl-carnitine levels, signatures of fatty acid metabolism[220,221], in BT-549 acquired resistant cells compared with BT-549 parental cells. Whereas we found that BT-549 parental cells exhibited few changes in acyl-carnitine

80

levels upon co-treatment with KA and cerulenin, we found that when acquired resistant

cells are maintained in KA, acyl-carnitines are elevated, but upon co-treatment with

cerulenin, many of them significantly decrease (Fig. 23B and Fig. 24E). In corroboration

with these findings, treatment with etomoxir, an inhibitor of carnitine

palmitoyltransferase (CPT1), showed modest differential effects in viability of acquired

resistant cells compared with parental cells, notably at 100 μm (Fig. 24F).

Because the biguanide metformin has been shown to decrease fatty acid and

mitochondrial metabolism[222], we asked whether metformin displayed similar effects as

cerulenin and etomoxir. Using the measured IC50 of metformin in BT-549 parental cells

(Fig. 24G), we co-treated parental and acquired resistant cells with metformin and KA,

which revealed decreases in cell viability of both BT-549 parental and acquired resistant

cells, albeit to a lesser extent in BT-549(R)2 cells, and no significant response in the

nonglycolytic MCF-7 cells (Fig. 24, H and I). We also found that upon co-treatment with

KA and metformin compared with KA alone, acyl-carnitines were to a larger extent

significantly decreased in acquired resistant cells than in parental cells (Fig. 23, C and D

and Fig. 24, J and K). Given the observed fatty acid metabolic phenotypes, we asked

whether KA-resistant cells also depend on oxidative phosphorylation. We profiled the

TCA cycle intermediates, a readout of oxidative phosphorylation, in the context of

metformin inhibition in parental and KA-resistant cells (Fig. 24L). Upon treating

parental cells with metformin in combination with KA, we observed decreases in several

TCA cycle metabolites, including α-ketoglutarate. However, whereas we found similar

decreases in α-ketoglutarate upon metformin treatment in all three resistant cell lines

maintained in KA, we also observed significant or modest increases in several other

TCA cycle intermediates. These results suggest that compared with parental cells,

acquired resistant cells rely more on oxidative phosphorylation. Taken together, these

data confirm that distinct metabolic phenotypes related to fatty acid metabolism occur

downstream of the differences in glycolysis in acquired resistant cells.
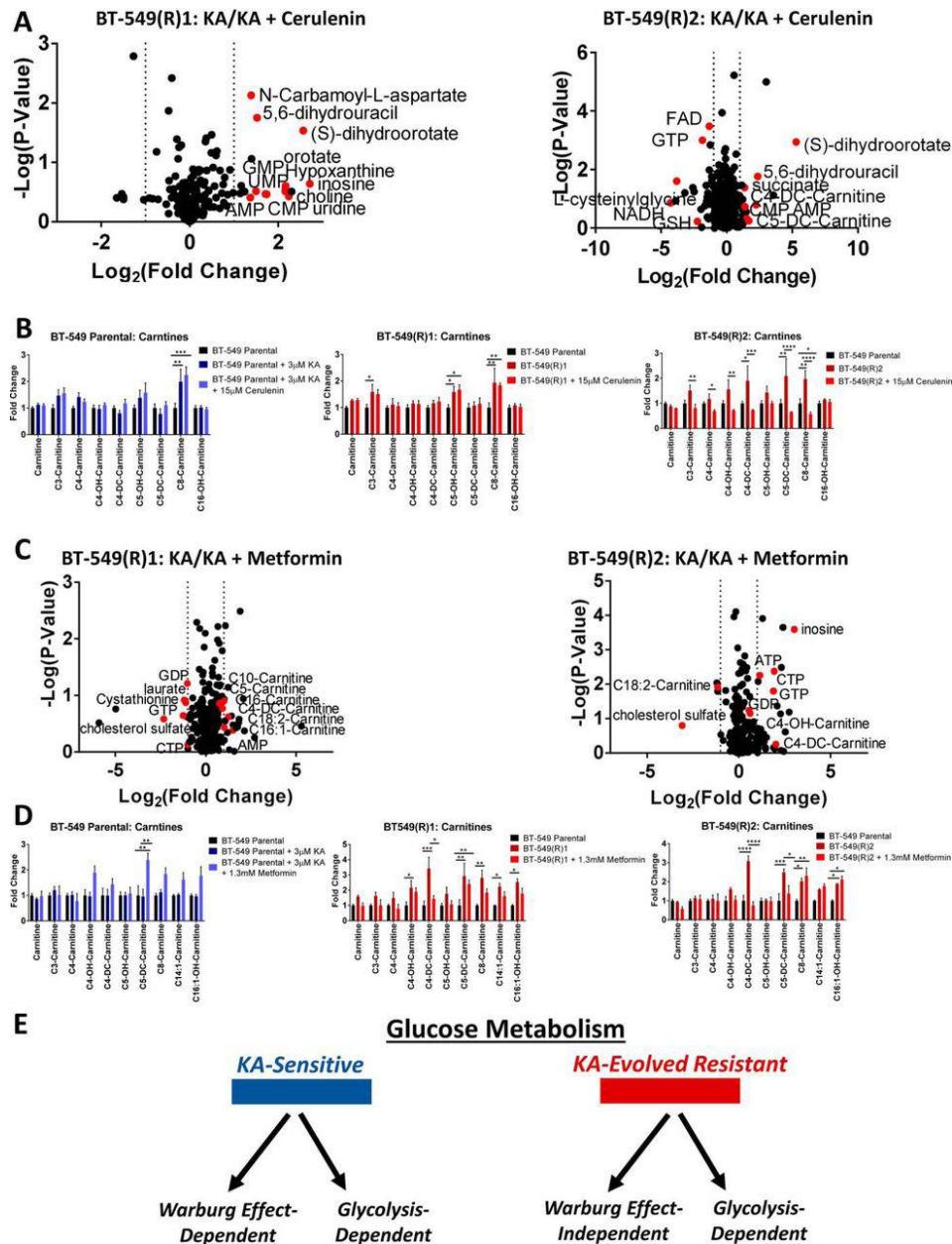
Figure 23: Changes in fatty acid metabolism occur downstream of differences in glycolysis in acquired resistance to KA.

A) volcano plots showing metabolite profiles of BT-549 acquired resistant (R)1 and (R)2 cells maintained in KA (3 μm) with or without cerulenin (15 μm). Log_2 -fold change versus $-log_{10}$ p value. Dotted lines along the x axis represent $\pm log_2(1)$ -fold change, and the dotted line along the y axis represents $-log_{10}(0.05)$. Metabolites $\pm log_2(1)$ -fold change are shown as red points with metabolite names denoted. All other metabolites are black points. B) acyl-carnitine levels in BT-549 parental and acquired

resistant cells maintained in KA (3 μm) and treated with or without cerulenin (15 μm) for 6 h. C) volcano plots showing metabolic profiles of BT-549 acquired resistant (R)1 and (R)2 cells maintained in KA (3 μm) with or without metformin (1.3 mm) as in A. D) acyl-carnitine levels in BT-549 parental and acquired resistant cells maintained in KA (3 μm) and treated with or without metformin (1.3 mm) for 6 h. E) schematic representing different phenotypically defined glucose metabolism states. SAH, S-adenosyl-l-homocysteine. All data are represented as mean ± S.E. (error bars) from n = 3 biological replicates. *, $p < 0.05$; **, $p < 0.01$; ***, $p < 0.001$; ****, $p < 0.0001$ as determined by two-way ANOVA.
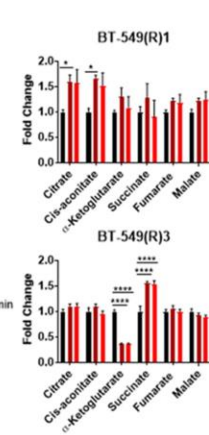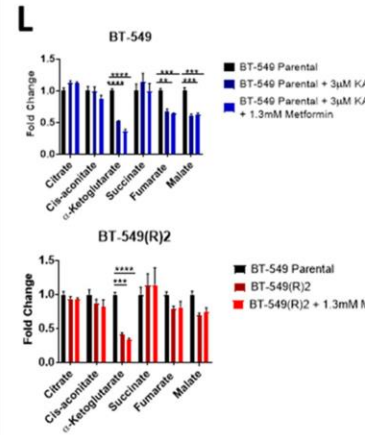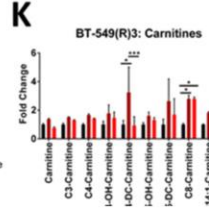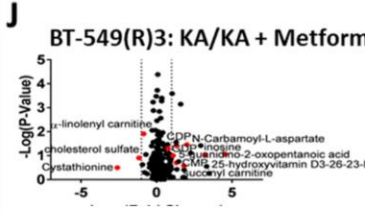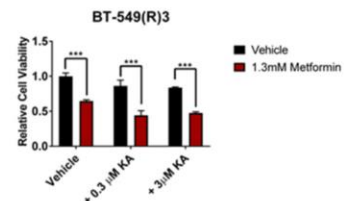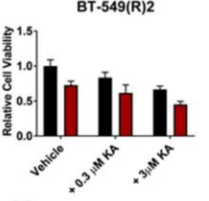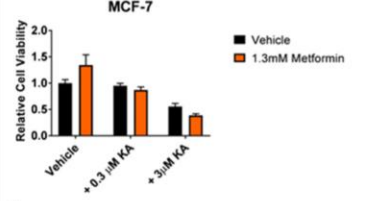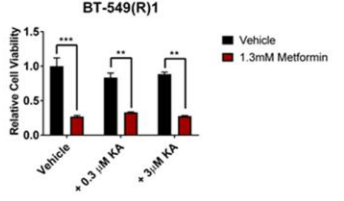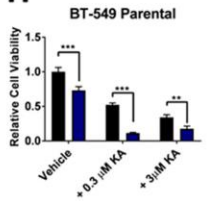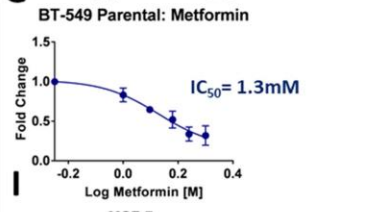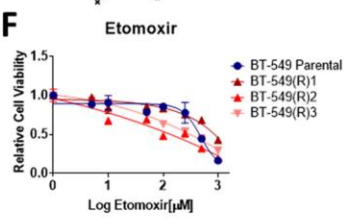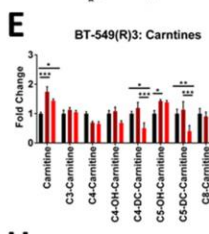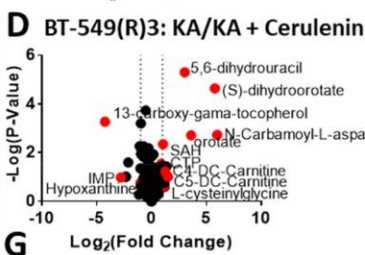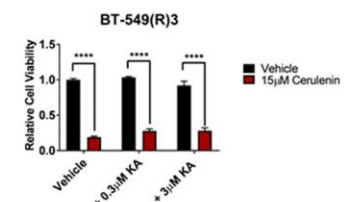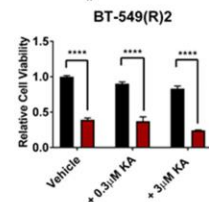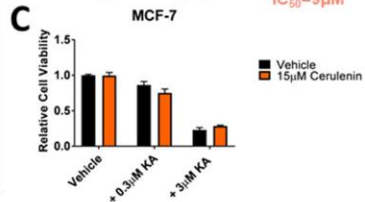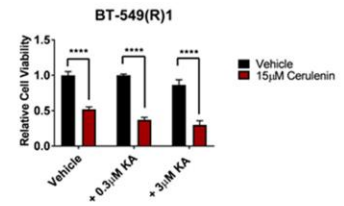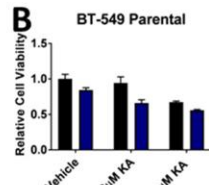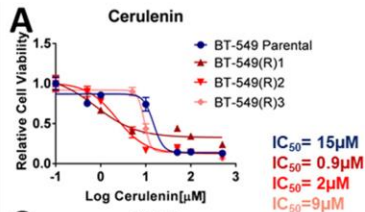
Figure 24: Supplemental-Changes in fatty acid metabolism occur downstream of differences in glycolysis in acquired resistance to KA.

A) BT-549 parental and acquired resistant cells dose-response curve treated with 0-500μM cerulenin for 24 hours. B) Cell viability of BT-549 parental cells and acquired resistant cells treated with cerulenin (15μM) with or without KA (0.3μM or 3μM) for 24 hours. C) Cell viability of MCF-7 cells as in B. D) Volcano plot showing metabolite profiles of BT-549 acquired resistant (R)3 cells maintained in KA (3μM) with or without cerulenin (15μM). $\log_2$ fold change versus $\log_{10}$ p-value. Dotted lines along x-axis represent ± $\log_2(1)$ fold change and dotted line along y-axis represents $-\log_{10}(0.05)$. Metabolites ± $\log_2(1)$ fold change shown as red points with metabolite names denoted. All other metabolites are black points. E) Acyl-carnitine levels in BT-549 acquired resistant (R)3 cells maintained in KA (3μM) and treated with or without cerulenin (15μM) for 6 hours. F) BT-549 parental and acquired resistant cells dose-response curve treated with 0-1mM etomoxir for 24 hours. G) BT-549 parental cell dose-response curve treated with 0-2mM metformin for 24 hours. H) Cell viability of BT-549 parental and acquired resistant cells treated with metformin (1.3mM) with or without KA (0.3μM or 3μM) for 24 hours. I) Cell viability of MCF-7 cells as in G. J) Volcano plot showing metabolite profiles of BT-549 acquired resistant (R)3 cells maintained in KA (3μM) with or without metformin (1.3mM) as in D. K) Acyl-carnitine levels in BT-549 acquired resistant (R)3 cells maintained in KA (3μM) and treated with or without metformin (1.3mM) for 6 hours. L) TCA cycle levels in BT-549 parental and acquired resistant cells maintained in KA (3μM) and treated with or without metformin (1.3mM) for 6 hours. All data are represented as mean ± SEM from n=3 biological replicates. *$p<0.05$, **$p<0.01$, ***$p<0.001$, ****$p<0.0001$ as determined by Two-Way ANOVA unless otherwise indicated.

3.3 Discussion

Previous work has shown that GAPDH has a specific regulatory role in aerobic glycolysis[16,17,223,224]. Our current study extends from this understanding to show that cells that evolve resistance to a specific GAPDH inhibitor, KA, lose the WE but remain dependent on glycolysis with different metabolic outputs from cells undergoing the WE or not. In particular, we demonstrate that cells can exist in at least two separate states of glucose metabolism, including WE-dependent and glycolysis-dependent or WE-

independent and glycolysis-dependent. Glycolysis has been thoroughly studied using

models that ablate the expression of glycolytic enzymes or completely block the

pathway[12,13,215,225], which reduces overall or eliminates altogether the activity of

glycolysis. Our model of evolved resistance to KA is useful to study glucose metabolism

regulation without complete pathway inhibition. Instead, we were able to place a

selection pressure against the fitness of using the WE during proliferation. Moreover,

using metabolomics, we further demonstrate that the resulting pressure to lose the WE

retains a requirement for glycolysis but alters several metabolic outputs in central

carbon metabolism. For example, fatty acid metabolism is up-regulated and selectively

required in cells. Our extensive metabolomics analyses also provide insight into

enzymatic activity changes. Based on our profiling, it is worth noting that many

activities in enzymes have likely changed throughout glycolysis and branching

pathways. These enzyme activities, as well as the availability of different nutrients and

metabolites, may also contribute to the observed fluxes through glycolysis and other

biosynthetic pathways that are dependent on glycolytic metabolites. Furthermore, we

could capture the temporal dynamics of metabolic alterations from early to late time

points of this evolution, which also may depend on factors such as nutrient availability

and enzyme activities. In physiology, such as within a tumor microenvironment, it is

likely that this range of metabolic plasticity allows for rapid adaptation to a dynamic

environment. A genome-wide study could be considered for future studies to complement changes observed in the metabolic network.

We were able to study glycolysis under different configurations of metabolic activity as cells transition from the WE to another glycolytic state. We provide clear evidence for a distinction between the WE and glucose metabolism. Interestingly, previous literature and related drug development efforts have worked under the model that glycolysis functions as a binary switch (i.e. glucose-dependent or -independent)[215,216]. In these cases, glucose dependence is identical to aerobic glycolysis. Our findings show that although KA-resistant cells no longer undergo the WE, they undergo glycolysis with less lactate production and remain dependent on glucose uptake. Whereas the difference in intracellular lactate levels between parental cells treated with KA and acquired resistant cells maintained in KA was not as dramatic as was seen with measurements of secreted lactate, the majority of lactate produced by cells is immediately secreted into the environment[4,214], likely accounting for the larger differential found in secreted lactate. Thus, our data indicate that glucose metabolism exists functionally in a set of states, depending on selective pressures and demands for cellular survival. By evolving resistance to GAPDH inhibition with KA, we show that WE-undergoing cells that lose aerobic glycolysis do not simply switch to increased oxidative phosphorylation but maintain glucose metabolism in a separate biological state with separate metabolic outputs.

Although aerobic glycolysis has been extensively studied over the years, whether the WE has a function aside from glycolysis has been questioned[226,227]. Our findings provide evidence for the WE existing as a biologically functional state of glucose metabolism. From a therapeutic perspective, elucidating the WE as a distinct phenomenon from glucose metabolism provides a rationale for continued efforts to target the WE while keeping all other forms of glycolysis intact. Such efforts are under way, including various studies particularly focusing on the targeting of GAPDH[223,224,228]. The practicability of targeting GAPDH therapeutically likely results from the ability to target its activity. GAPDH is a highly abundant protein and is the most abundant protein in glycolysis[229]. In addition, previous reports record that most cancer types exhibit moderate GAPDH protein staining relative to normal tissues[230,231], indicating that GAPDH levels between normal and cancer cells are not considered to be different from each other. Thus, cells undergoing the WE exhibit higher GAPDH activity irrespective of protein level, which has been shown to be associated with increased sensitivity to GAPDH inhibition[16,17]. Additional studies also indicate the feasibility and tolerability of targeting GAPDH therapeutically in disease contexts[17,223].

This current study now provides evidence for a proof-of-principle concept in which acquired resistance to a potential cancer therapy can be encoded in the metabolic activity of the metabolic network controlled by the therapeutic target (i.e. GAPDH). This study further shows that acquired resistance from inhibition of the WE can result in an

altered glycolytic state whereby cells still remain dependent on glucose carbon for fueling their metabolic demands. These findings provide clinical relevance and systematic strategies for therapeutically targeting pathways in the central carbon network upon acquired resistance to inhibiting the WE, such as fatty acid metabolism. Notably, the WE and high rates of glycolysis have been shown to complement fatty acid metabolism in a tumor setting[232]. One potential reason for this could be due to glucose-derived pyruvate incorporation into the TCA cycle, which would fuel fatty acid metabolism and synthesis.

The implications of our findings could extend to effective strategies in the tumor microenvironment as well, especially given the efficacy of KA on immune cell populations that rely on glycolysis for activation. Beyond the clinical implications of understanding acquired resistance to the WE, we now provide insight onto how cells can metabolically evolve resistance to a metabolic inhibitor over time. This is an important concept that can apply to other clinically relevant targeted metabolic therapies, such as 5-fluorouracil or gemcitabine, both of which have exhibited challenges clinically due to resistance. Although this study by itself does not resolve whether the WE is in fact driving cancer or whether it is a metabolic consequence of cancer progression, it does confirm that the WE is a real biological phenomenon with different biological and metabolic properties.

3.4 Methods

3.4.1 Cell culture

BT-549 and MCF-7 cells were cultured in full medium containing RPMI 1640 (Gibco), 10% heat-inactivated fetal bovine serum (FBS), 100 units/ml penicillin, and 100 µg/ml streptomycin. BT-549 and MCF-7 cells were obtained from the American Tissue Culture Collection (ATCC). KA-resistant BT-549 cells were cultured and maintained in full medium containing RPMI 1640, 10% heat-inactivated FBS, 100 units/ml penicillin, 100 µg/ml streptomycin, and 3 µm KA (isolated in-house) (16). Cells were cultured in a 37 °C, 5% CO_2 atmosphere.

3.4.2 Time to progression to resistance assay

Cells were allowed to progress to resistance as described previously[233]. To allow cells to acquire resistance to KA, BT-549 breast cancer cells were first seeded in triplicate in 15-cm plates at 3×10^6 cells/plate in normal medium. After 24 h, the normal growth medium was replaced with fresh medium at the indicated KA treatment. After 7 days, cells were lifted with 0.25% trypsin (Cellgro) and counted using a Moxi Z mini automated cell counter. All cells up to 1×10^6 cells were centrifuged at 1,500 rpm for 3 min, resuspended in 10 ml of medium, and plated into a 15-cm plate with fresh treatment. For each measurement, once cell number reached 3×10^6 cells 2 weeks in a row, the dose was increased as indicated. This procedure was repeated weekly for 20 weeks. Weekly growth rates (µ) were calculated from the number of cells plated the

91

previous week (N_0) and the number of cells counted in the current week (N) according to

the formula,

$$lnN = lnN_0 + \mu t$$
(Eq. 1)

where t is elapsed time in hours. These growth rates were then used to project

total cell number as if no cells had been discarded.

3.4.3 Cell viability assays

For all cell lines, 5×10^4 cells/well were seeded in triplicate in a 96-well plate and

allowed to adhere for 24 h. The following day, vehicle or treatment was added to each

well at the respective concentrations. After 24 h, the medium was aspirated and replaced

with 100 μl of phenol red–free RPMI 1640, and 12 mm 3-[4,5-dimethylthiazol-2-yl]-2,5-

diphenyltetrazolium (MTT) (Thermo Fisher Scientific, #M6494) was added to the cells.

After 4 h, the medium containing MTT was aspirated, and 50 μl of DMSO was added to

dissolve the formazan and read at 540 nm.

3.4.4 Drug treatments

For all cell lines, IC_{50} values of KA were measured by seeding 5×10^4 cells/well in

triplicate in a 96-well plate and allowed to adhere for 24 h. The following day, medium

was changed, and concentrations of either vehicle (H_2O or DMSO), KA, E11[210], cerulenin

(Sigma-Aldrich, #C2389), metformin (Santa Cruz Biotechnology, #202000A), or etomoxir

(Sigma-Aldrich, #E1905) were added. After 24 h, cell viability assays were carried out

using MTT as described previously.

3.4.5 Nutrient restriction in medium

For all cell lines, 5×10^4 cells/well were seeded in triplicate with complete RPMI 1640 medium in 96-well plates and allowed to adhere for 24 h. On the following day, the respective treatment medium was added in the absence or presence of KA at the indicated treatments. MTT assays were carried out as described previously. Treatment medium used was as follows: minus glucose (−Glucose): RPMI 1640 with glutamine lacking glucose containing 10% dialyzed FBS (Life Technologies), 100 units/ml penicillin, and 100 μg/ml streptomycin; delipidated serum (D-FBS): RPMI 1640 with glutamine containing 10% delipidated FBS (Thermo Fisher Scientific, #A3382101), 100 units/ml penicillin, and 100 μg/ml streptomycin. Cells were grown at 37 °C with 5% CO_2.

3.4.6 Synergism experiments

BT-549, SK-MEL-28, SK-MEL-5, and NCI-H522 cell lines were seeded at 5×10^4 cells/well in 96-well plates and allowed to adhere for 24 h prior to treatment. After, 0, 0.5, 1, 5, and 10 μM KA were used as single concentrations or in combination with 0, 10, 100, 500, and 1,000 nM E11 or in combination with 0, 0.5, 1, 5, and 11 mM glucose. After 24 h, dose-response curves were generated using MTT reagent as described above. Then cell viability values and concentrations were inputted into CompuSyn 1.0 software, and combination indices were calculated by the software to determine synergism, additivity, or antagonism.

3.4.7 Resensitization of BT-549 acquired resistant cells to KA

KA was removed from BT-549 acquired resistant cells for 3 passages (~2 weeks) (BT-549(R)1–3$^{-KA,p.3}$). After, parental cells, acquired resistant cells maintained in 3 μm KA, and BT-549(R)1–3$^{-KA,p.3}$ cells were treated with vehicle, 0.5 μM, or 3 μM KA for 24 h followed by measurement of cell viability with MTT reagent.

3.4.8 GAPDH activity assay

A GAPDH activity assay kit (BioVision, #K680) was used. All cells were seeded at 1×10^6 cells/10-cm plate with either vehicle or KA. After 24 h, cells were lysed, an NADH standard curve was made, and cells were measured at 450 nm in kinetic mode for 60 min at 37 °C according to the manufacturer's instructions.

3.4.9 Microscopy

Cells were seeded at a density of 5×10^3 cells/well in 6-well plates and allowed to adhere for 24 h prior to treatment. After 48 h, images were captured using a Leica DM IL LED microscope equipped with a Leica MC170HD camera at ×10 objective using LAS EZ software (Leica). Scale bars represent 100 μm.

3.4.10 Stable isotope labeling

Cells were seeded at 3×10^5 cells/well in a 6-well plate and allowed to adhere for 24 h. For [U-^{13}C]glucose isotopic labeling, cells were treated with either vehicle or KA for 6 h and then replaced with RPMI 1640 medium containing 11 mm [U-^{13}C]glucose (Cambridge Isotope Laboratories, #CLM-1396) and vehicle or KA for 0–4 h or for 24 h.

Metabolites were then extracted. For [U-^{13}C]glutamine isotopic labeling, cells were

treated with either vehicle or KA for 6 h and then replaced with RPMI 1640 medium

containing 10% dialyzed FBS, 2 mm [U-^{13}C]glutamine (Cambridge Isotope Laboratories,

#CLM-1822), and vehicle or KA for 24 h. Metabolites were then extracted. For [U-

^{13}C]palmitate isotopic labeling, cells were treated with vehicle or KA for 6 h and then

replaced with RPMI 1640 medium containing 10% dialyzed FBS, 100 μm [U-

^{13}C]palmitate (Cambridge Isotope Laboratories, #CLM-409), and vehicle or KA for 24 h.

Metabolites were then extracted.

3.4.11 Intracellular metabolite measurements

Cells were seeded at 3×10^5 cells/well in a 6-well plate and allowed to adhere for

24 h. After, cells were treated with vehicle or KA for 6 h and then washed twice with

0.9% NaCl. Metabolites were then extracted.

3.4.12 Extracellular metabolite excretion measurements

Cells were seeded at 3×10^5 cells/well in a 6-well plate and allowed to adhere for

24 h. After, cells were treated with vehicle or KA, and 15 μl of medium was collected

from 0 to 4 h and 24 h. Metabolites were then extracted.

3.4.13 Metabolite extraction

Metabolite extraction and subsequent LC-HRMS for polar metabolites of each

cell line were carried out using a Q Exactive Plus mass spectrometer as described

previously[206,234]. For culture from adherent cell lines, medium was quickly aspirated.

Next, 1 ml of extraction solvent (80% methanol/water) cooled to −80 °C overnight was added immediately to each well, and the plates were then transferred to −80 °C for 15 min. After, the plates were removed, and cells were scraped into the extraction solvent on dry ice. For medium extractions, 15 μl of medium was collected at 0–24 h. Next, 15 μl of extraction solvent (80% methanol/water) (Optima LC-MS grade, Fisher; methanol, #A456; water, #W6) was added to the medium. For absolute quantification of KA in cells, medium was quickly aspirated, and cells were washed twice with 0.9% NaCl following extraction for culture from adherent cells. 0.7 μM KA in water was added into extraction solvent before centrifugation. For absolute quantification of KA at 2, 6, and 24 h, cells were washed twice with 0.9% NaCl, and a standard curve of KA was applied with concentrations from 0 to 25 μm KA added into methanol solvent of untreated BT-549 cells before centrifugation. All metabolite extractions were centrifuged at 20,000 × g at 4 °C for 10 min. Finally, the solvent in each sample was evaporated using a speed vacuum for metabolite analysis. For polar metabolite analysis, the cell metabolite extract was first dissolved in 15 μl of water, followed by dilution with 15 μl of methanol/acetonitrile (1:1, v/v) (Optima LC-MS grade, Fisher; methanol, #A456; acetonitrile, #A955). Samples were centrifuged at 20,000 × g for 10 min at 4 °C, and the supernatants were transferred to LC vials. The injection volume for polar metabolite analysis was 5 μl.

3.4.14 Liquid chromatography

An XBridge amide column (100 × 2.1-mm inner diameter, 3.5 μm; Waters) was used on a Dionex (Ultimate 3000 UHPLC) for compound separation at room temperature. Mobile phase A is water with 5 mM ammonium acetate, pH 6.9, and mobile phase B is 100% acetonitrile. The gradient is linear as follows: 0 min, 85% B; 1.5 min, 85% B; 5.5 min, 35% B; 10 min, 35% B; 10.5 min, 35% B; 10.6 min, 10% B; 12.5 min, 10% B; 13.5 min, 85% B; and 20 min, 85% B. The flow rate was 0.15 ml/min from 0 to 5.5 min, 0.17 ml/min from 6.9 to 10.5 min, 0.3 ml/min from 10.6 to 17.9 min, and 0.15 ml/min from 18 to 20 min. All solvents are LC-MS grade and were purchased from Fisher.

3.4.15 Mass spectrometry

The Q Exactive Plus mass spectrometer (Thermo Scientific) is equipped with a heated electrospray ionization probe, and the relevant parameters were as listed: evaporation temperature, 120 °C; sheath gas, 30; auxiliary gas, 10; sweep gas, 3; spray voltage, 3.6 kV for positive mode and 2.5 kV for negative mode. Capillary temperature was set at 320 °C, and S lens was 55. A full scan range from 70 to 900 (m/z) was used. The resolution was set at 70,000. The maximum injection time was 200 ms. Automated gain control was targeted at 3×10^6 ions.

3.4.16 Peak extraction and data analysis

Raw data collected from LC-Q Exactive Plus MS was processed on Sieve 2.0 (Thermo Scientific). Peak alignment and detection were performed according to the

protocol described by Thermo Scientific. For a targeted metabolite analysis, the method

"peak alignment and frame extraction" was applied. An input file of theoretical m/z and

detected retention time of 197 known metabolites was used for targeted metabolite

analysis with data collected in positive mode, whereas a separate input file of 262

metabolites was used for negative mode. m/z width was set to 10 ppm. The output file

including detected m/z and relative intensity in different samples was obtained after

data processing. If the lowest integrated mass spectrometer signal (MS intensity) was

less than 1,000 and the highest signal was less than 10,000, then this metabolite was

considered below the detection limit and excluded for further data analysis. If the lowest

signal was less than 1,000, but the highest signal was more than 10,000, then a value of

1,000 was imputed for the lowest signals. Mass isotopomer distributions were

calculated, and samples were normalized by comparing the ratio of glucose-derived

labeled metabolites to unlabeled metabolites within each sample. Quantitation and

statistics were calculated using Microsoft Excel and GraphPad Prism 7.0.

3.4.17 Analysis of metabolomics data

GENE-E and Morpheus software were used for hierarchical clustering and heat

map generation (Broad Institute, https://software.broadinstitute.org/GENE-

E/index.html)[235]. For hierarchical clustering, Spearman correlation parameters were

implemented for row and column parameters, with the exception of BT-549 parental and

acquired resistant drug response data, in which hierarchical clustering for row

parameters only was used. Quantile normalization was used to normalize the data,

represented by color scales.

3.4.18 Lactate flux calculations

The time-dependent lactate-labeling pattern was modeled as with the equation,

$$\frac{[X^*]}{X^T} = 1 - e^{-\frac{f_X}{X^T}t}$$

(Eq. 2)

In which $[X^*]$ is the concentration of labeled lactate, X^T is the total concentration

(both labeled and unlabeled) of lactate, and f_X is the lactate production flux. This model

was fit to lactate mass isotopomer distributions using the fit() function in MATLAB to

determine relative lactate production fluxes. Relative lactate pool sizes were estimated

from MS signal intensities.

3.4.18 Quantification and statistical analysis

Unless otherwise noted, all error bars represent reported ± S.E. with n = 3

independent biological measurements, and statistical tests resulting in p value

computations were computed using two-tailed Student's t test, multiple t tests, one-way

ANOVA, or two-way ANOVA of log-transformed data followed by Tukey's multiple

comparisons. All statistics were computed using GraphPad Prism 7 (GraphPad

Software, Inc.).

3.5 Author Contributions

This chapter is from a collaborative study. Annamarie Allen assisted the lead author of the study, Maria Liberti, with collecting experimental data, data analysis, and figure presentation and organization. Specifically, Annamarie contributed significantly to many of the cell viability experiments involving cerulenin, etomoxir, metformin, and E11. Annamarie was also responsible for the finding that acquired resistant cells can become resensitized to KA.

4. Nucleotide metabolism is a target of ferroptosis

4.1 Background and Context

As described in Section 1.5, ferroptosis is an oxidative, iron-dependent form of cell death that is characterized by uncontrolled lipid peroxidation. The small molecule erastin induces ferroptosis by depleting cells of glutathione, which is needed by the lipid peroxide-detoxifying enzyme GPX4[172]. While the toxic effects of lipid peroxides have long been known[236,237], the idea of ferroptosis as a distinct cell death process is fairly recent and came about by elucidating the mechanism of erastin-induced cell death[75]. The study of ferroptosis has since been inextricably tied to erastin and other small molecule ferroptosis inducers and inhibitors such as the GPX4 inhibitor RSL3 and the lipophilic antioxidant ferrostatin-1.

These ferroptosis inducers are of interest as potential anti-cancer therapies, stemming from the notion that they could target apoptosis-evading cancers[76], and additionally supported by studies showing that they enhance the effectiveness of the effectiveness of chemotherapy and radiotherapy [86-90,180,182,183]. As described in Section 1.3.3, some cancers also show increased reliance on cystine uptake, providing additional rationale for the potential use of drugs like erastin for treating cancer.

Altered metabolism particularly from the mitochondria has been shown to influence ferroptosis providing additional aspects of the process[186], but whether this picture is complete is unknown. To investigate this question, we used our metabolomics

platform, which offers a broad coverage of cellular metabolism by measuring over 300 metabolites from more than 40 different metabolic pathways[206,234] and systematically profiled the metabolic effects of erastin and other ferroptosis inducers. We found that disruptions to nucleotide metabolism were surprisingly one of the largest metabolic alterations observed during ferroptosis, and additionally found that disruptions to central carbon metabolism are also present and may lead to the observed nucleotide disruptions.

4.2 Results

4.2.1 Alterations in nucleotide metabolism are overrepresented in metabolic profile of ferroptosis

To determine how global metabolism is affected when cells are treated with ferroptosis inducers, we treated three different ferroptosis-sensitive cell lines with an IC_{50} dose of ferroptosis inducers erastin or RSL3 (Fig. 25A) for 15 hours (before the onset of cell death) and then extracted polar metabolites for LC-MS based metabolomics and metabolic profiling. As expected, alterations in cysteine-related metabolites were observed in the metabolic profile of erastin-treated cells (Fig. 25B, D, F). However, all three cell lines also showed many alterations in the levels of nucleotide-related metabolites including nucleotides, nucleotide precursors and breakdown products, and/or nucleotide-sugars in both erastin and RSL3-treated cells, and these were some of the largest metabolic alterations observed (Fig. 25B-G). To determine whether nucleotide-related metabolites were statistically overrepresented in the metabolic profile

102

of erastin and RSL3-treated cells, metabolites with p<0.05 on each volcano plot were

sorted by the absolute value of the difference between DMSO and drug-treated. The

largest 10% of these metabolites were classified as nucleotide-related or not, and the

percentage that were nucleotide related is shown in Fig. 25H, I. Statistical

overrepresentation of nucleotide-related metabolites was determined by comparing this

percentage to the percentage of nucleotide-related metabolites that would be expected in

the top 10% based on chance. Nucleotide-related metabolites were statistically

overrepresented in erastin-treated BT-549 and HT-1080 cells, and in RSL3-treated HT-

1080 and U2OS cells (Fig. 25 H, I). In erastin-treated U2OS and RSL3-treated BT-549

cells, nucleotide-related metabolites were not statistically overrepresented, but

nucleotide changes were still observed in the metabolic profile (Fig. 25E, F). Common

nucleotide alterations observed included increased nucleoside levels (Fig. 26A-C),

decreased nucleotide precursor levels (Fig. 26D-F) and decreased nucleotide di- and

triphosphate levels (Fig. 26G-O). To determine whether these alterations could be the

result of off-target effects of either drug, we co-treated HT-1080 cells with erastin or

RSL3 and ferroptosis inhibitors deferoxamine (DFO), ferrostatin-1 (ferrostatin), or the

antioxidant Trolox. We found that nearly all nucleotide-related metabolic alterations

were at least partially rescued by ferrostatin treatment (Fig. 27A), and most of the

alterations were also partially rescued by DFO or Trolox treatment. We also found that

ferrostatin fully rescued the majority of RSL3-induced nucleotide alterations, and fully

103

rescued 50% of erastin-induced nucleotide changes, while DFO fully rescued 42 and 46%

of RSL3 and erastin-induced nucleotide changes, respectively (Fig. 27 B). DFO was

notably less effective than ferrostatin at rescuing nucleotide alterations, however this is

unsurprising as DFO has been shown to affect nucleotide metabolism itself[238]. The lesser

effectiveness of Trolox compared to ferrostatin was also not surprising, as ferrostatin has

been shown to more efficiently suppress lipid peroxidation in the context of ferroptosis

than Trolox[239]. These data show that most of the observed nucleotide alterations were

reversed by validated ferroptosis inhibitors and are unlikely the result of off-target

effects of either drug.
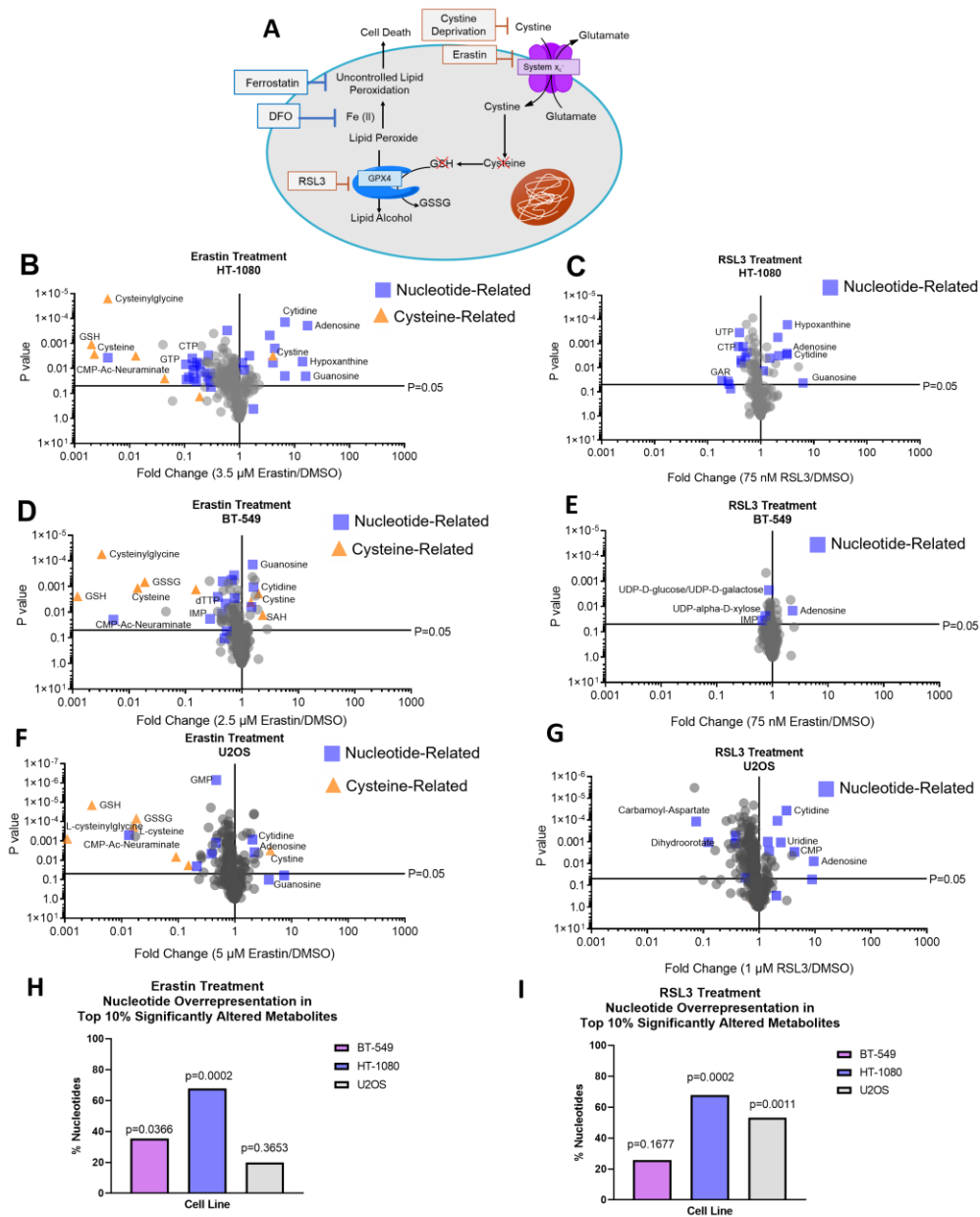
Figure 25: Alterations in nucleotide metabolism are overrepresented in metabolic profile of ferroptosis

A) Schematic of ferroptosis pathway B-I) Results from polar metabolomics shown as volcano plots using p-values generated from multiple unpaired t-tests on log-transformed ion intensity values. H, I) The percentage of the largest 10% of significantly altered metabolites that were nucleotides, nucleotide precursors and breakdown products, and nucleotide-sugars/lipids. For each volcano plot, metabolites with p<0.05

were sorted by the absolute value of the difference between DMSO and drug treatment, and the largest 10% were categorized as nucleotide-related or not. The percentage of these that were classified as nucleotide-related is graphed and the p-value is from a one-sided Fisher's exact test comparison of this percentage versus the expected number of nucleotide-related metabolites that would be in the top 10% most significantly altered based on chance.

Abbreviations: Deferoxamine (DFO), Reduced glutathione (GSH), Oxidized glutathione (GSSG), Glycineamide ribonucleotide (GAR), S-Adenosyl-L-homocysteine (SAH), CMP-N-Acetyl-Beta-Neuraminate (CMP-Ac-Neuraminate)
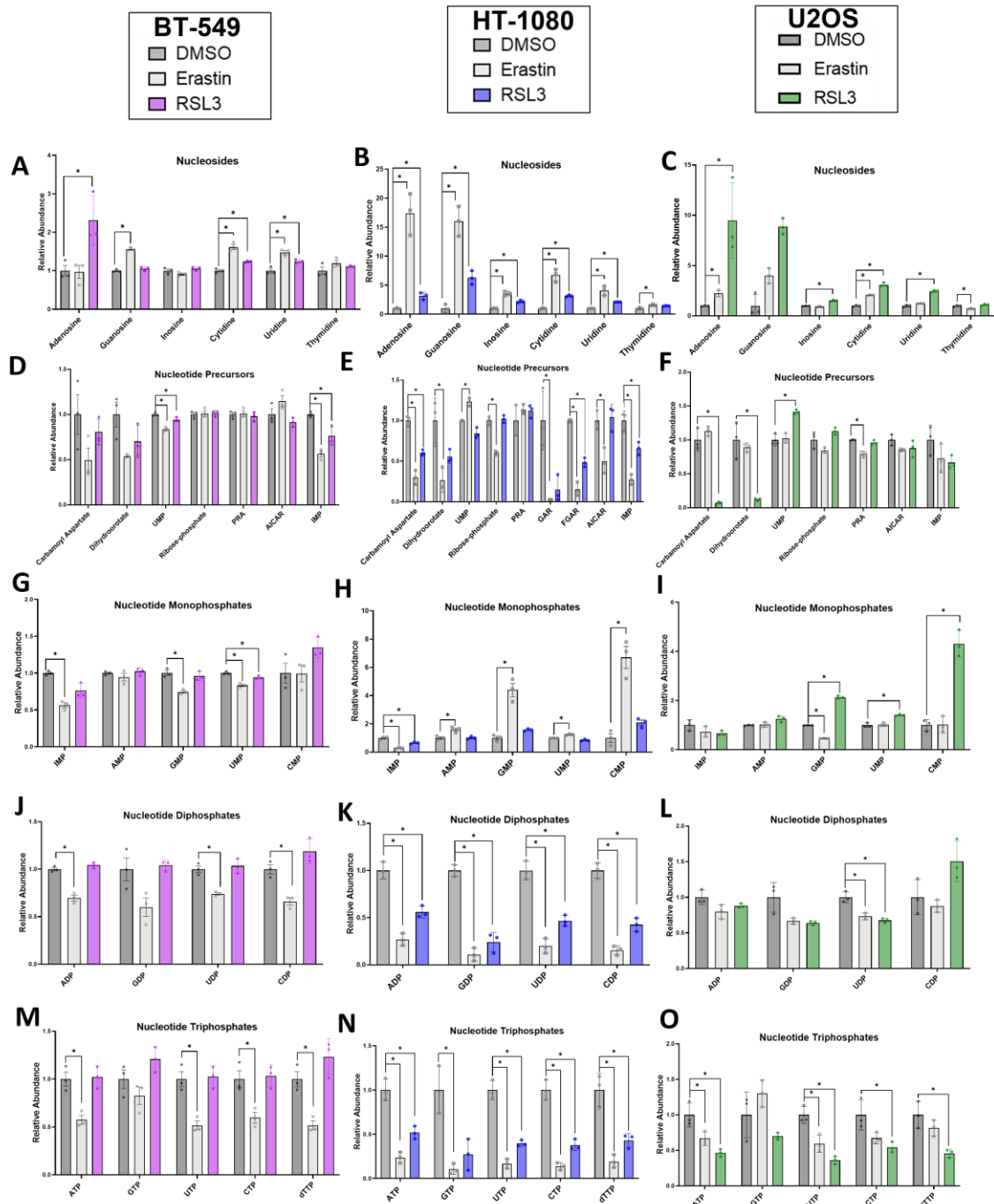
Figure 26: Supplemental- Alterations in nucleotide metabolism are overrepresented in metabolic profile of ferroptosis

A, D, G, J, M) Nucleotide-related metabolites from BT-549 cells treated with 3.5 μM erastin or 75 nM RSL3. B, E, H, K, N) Nucleotide-related metabolites from HT-1080 cells

treated with 2.5 μM erastin or 75 nM RSL3. C F, I, L, O) Nucleotide-related metabolites from U2OS cells treated with 5 μM erastin or 1 μM RSL3. For Figs. A-O, a two-way repeated measures ANOVA was performed on log-transformed values and followed by an uncorrected Fisher's LSD test if interaction term or main effect of treatment $p < 0.05$. * indicates $p < 0.05$ when comparing DMSO to Erastin or RSL3 treatment in Fisher's LSD test.

Abbreviations: N-carbamoyl-L-aspartate (Carbamoyl aspartate), 5-phosphoribosylamine (PRA), Glycineamide ribonucleotide (GAR), Formylglycinamide ribonucleotide (FGAR), 5-amino-4-imidazolecarboxamide (AICAR)
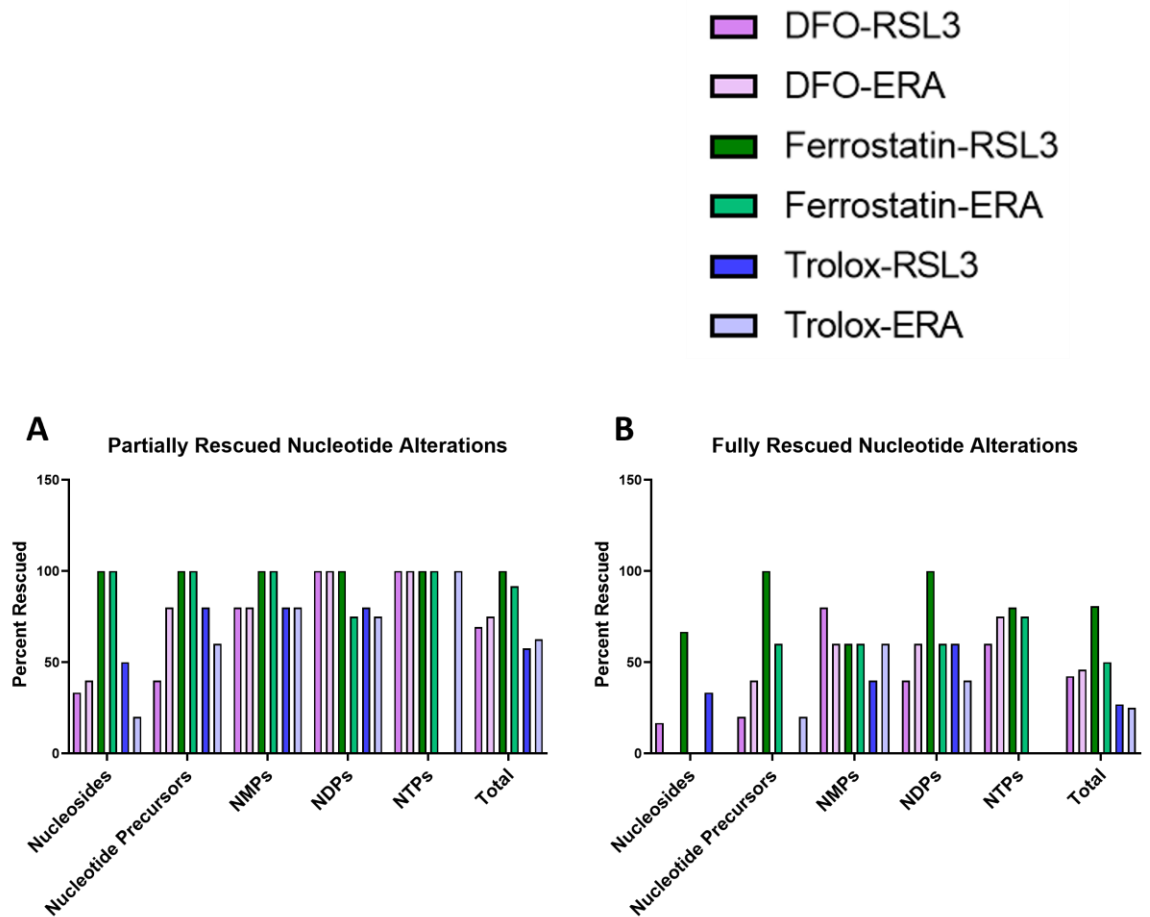
Figure 27: Nucleotide alterations are rescued by ferroptosis inhibitors

A) Percentage of nucleotide-related metabolites that were partially rescued by DFO, ferrostatin, or Trolox treatment in RSL3 or erastin (ERA)-treated cells. A partial rescue was defined as the rescue condition metabolite level being significantly higher or lower

than in the non-rescue drug-treated condition (higher if erastin or RSL3 caused a significant depletion in the metabolite, and lower if they caused a significant accumulate of the metabolite). Significance was determined by a two-way repeated measures ANOVA performed on log-transformed values and followed by an uncorrected Fisher's LSD test comparing drug-treated to control or drug-treated + rescue agent. B) Percentage of nucleotide-related metabolites that were fully rescued by DFO, ferrostatin, or Trolox treatment in RSL3 or erastin-treated cells. Metabolites were classified as "fully rescued" if they met both of the following conditions: 1) they were partially rescued defined by the conditions in A) and 2) the level of the metabolite in the rescue condition was not significantly different than the level of the metabolite in the control condition. Significance was determined by a two-way repeated measures ANOVA performed on log-transformed values and followed by an uncorrected Fisher's LSD test comparing control to drug-treated + rescue agent.

4.2.2 Erastin decreases nucleotide biosynthesis

Decreased nucleotide levels could result from insufficient nucleotide biosynthesis, insufficient energy levels, or both. To better understand how the ferroptosis inducer erastin causes this pattern of nucleotide changes, we performed ^{13}C-glucose tracing in BT-549 and HT-1080 cells treated with erastin and examined how nucleotide biosynthesis and energy producing pathways were affected. Universally labeled ^{13}C glucose (U-^{13}C glucose) labels purines and pyrimidines through conversion to ribose-5-phosphate (R5P) via the pentose phosphate pathway (Fig. 28 A). M+5 R5P showed no differences in fractional labeling between DMSO- and erastin-treated cells (Fig. 28 B, C), suggesting that pentose phosphate pathway defects are not responsible for any decreased m+5 nucleotide labeling. In HT-1080 cells, purines did not show decreased m+5 fractional labeling at the timepoint tested (Fig. 28 D-F), but pyrimidines did (Fig. 28 G-J). In BT-549 cells both purines and pyrimidines showed decreased m+5

fractional labeling (Fig. 28K-O). These results show that erastin disrupts nucleotide biosynthesis, which may partially explain why some nucleotides are depleted in cells treated with erastin.

Figure 28: Erastin decreases nucleotide biosynthesis

A) Schematic showing U-^{13}C Glucose nucleotide labeling through m+ 5 ribose-5-phosphate. B, D-H) M+5 fractional labeling plotted for relevant nucleotides and precursors from HT-1080 cells treated with 2.5 uM erastin. C, K-O) M+5 fractional

labeling plotted for relevant nucleotides and precursors collected from BT-549 cells treated with 3.5 uM erastin.

For Figs. B-O, an unpaired T-test was performed to compare DMSO to erastin for each metabolite. * indicates $p < 0.05$ for this test, no stars shown indicates $p > 0.05$.

4.2.3 Erastin alters glycolysis and citric acid cycle activity and decreases energy levels

Insufficient energy levels may also explain why higher-energy nucleotide di- and triphosphates were the type of nucleotide most often depleted under erastin treatment (Fig. 26 J-O), while lower-energy nucleotide monophosphate (Fig. 26 G-I) and nucleoside (Fig. 26 A-C) levels either increased or showed smaller fold-changes than the di- and triphosphates. To determine whether this could be occurring, we first looked at the total levels of metabolites in the energy-producing pathways glycolysis and the citric acid cycle (TCA). Erastin-treated HT-1080 and BT-549 cells showed significant depletions in many glycolytic intermediates (Fig. 29 A, D), and in TCA intermediates (Fig. 29 B, E). The ratio of ATP/AMP, an indicator of cellular energy status, was also significantly decreased in both cell lines (Fig. 29 C, F). U-^{13}C glucose tracing (Fig. 30 A) showed that pyruvate and lactate had significantly decreased m+3 fractional labeling under erastin treatment in both cell lines (Fig. 29 G, H, K, L) and a decreased m+3 pool size (Fig. 30 C, D, G, H), which indicates less glycolytic activity over time.

TCA cycle labeling showed a different pattern in the two different cell lines, with significantly increased ^{13}C glucose-derived m+2 labeling on the TCA cycle intermediates alpha-ketoglutarate (aKG) and malate in erastin-treated HT-1080 cells (Fig. 29 I, J) and

112

significantly less in erastin-treated BT-549 cells (Fig. 29 M, N). M+2 Aspartate, which is produced from the TCA cycle, also showed increased m+2 fractional labeling in erastin-treated HT-1080 cells and decreased m+2 fractional labeling in erastin-treated BT-549 cells (Fig. 30 E, I). M+4 aKG, which is produced in the second turn of the TCA cycle (Fig. 30 A), was also significantly increased in erastin-treated HT-1080 cells (Fig. 29 I). Before entering the TCA cycle, glucose is converted to pyruvate, which can enter the TCA via two enzymes, pyruvate dehydrogenase (PDH) and pyruvate carboxylase (PC) (Fig. 30 A). Pyruvate entry into the TCA via PC serves an anaplerotic role and can be distinguished from PDH-derived pyruvate labeling by subtracting the m+3 fraction of succinate from the m+3 fraction of malate or aspartate[192,240]. Interestingly, the m+3 malate fraction minus the m+3 succinate fraction was decreased in both cell lines treated with erastin (Fig. 29 J, N). The m+3 aspartate minus the m+3 succinate fraction was not decreased in erastin-treated HT-1080 cells (Fig. 30 E), but the labeling pattern of malate is more reliable to interpret since aspartate labeling is confounded by aspartate in the culture media[192]. Together, these results show that erastin-treated HT-1080 cells increase glucose usage into the TCA via PDH, while decreasing anaplerotic glucose entry into the TCA via PC. Erastin-treated BT-549 cells show decreased glucose usage in the TCA cycle through both PDH and PC indicating mitochondrial plasticity.
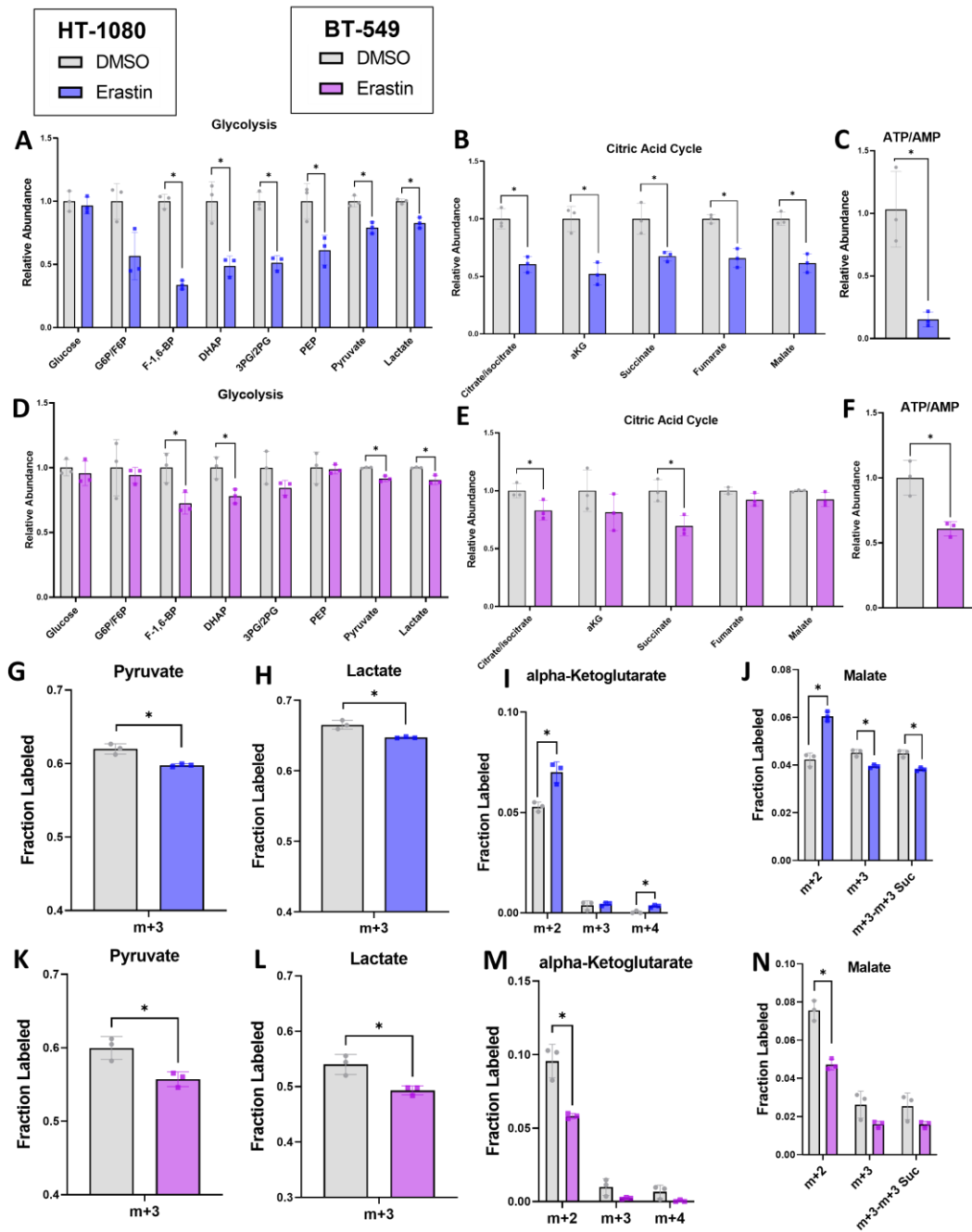
Figure 29: Erastin alters glycolysis and citric acid cycle activity and decreases energy levels

A-F) Relative levels of metabolites from relevant pathways in HT-1080 cells treated with 2.5 μM erastin or BT-549 cells treated with 3.5 μM erastin. G-N) Fractional labeling

plotted for relevant isotopomers in glycolysis and TCA in HT-1080 cells treated with 2.5 µM erastin or BT-549 cells treated with 3.5 µM erastin and subjected to U-^{13}C Glucose tracing. In Figs. J, N m+3-m+3 Suc represents the m+3 fraction of malate minus the m+3 fraction of succinate, which represents glucose entry into the TCA via pyruvate carboxylase.

For Figs. A-B and D-E a two-way repeated measures ANOVA was performed on log-transformed values and followed by an uncorrected Fisher's LSD test if interaction term or main effect of treatment $p<0.05$. * indicates $p<0.05$ when comparing DMSO to Erastin treatment in Fisher's LSD test, no stars shown indicates $p>0.05$. For Figs. C, F, G-N an unpaired T-test was performed to compare DMSO to erastin treatment. If more than one isotopomer is shown on the graph, a separate uncorrected T-test was performed for each. * indicates $p<0.05$ for this test, no stars shown indicates $p>0.05$.
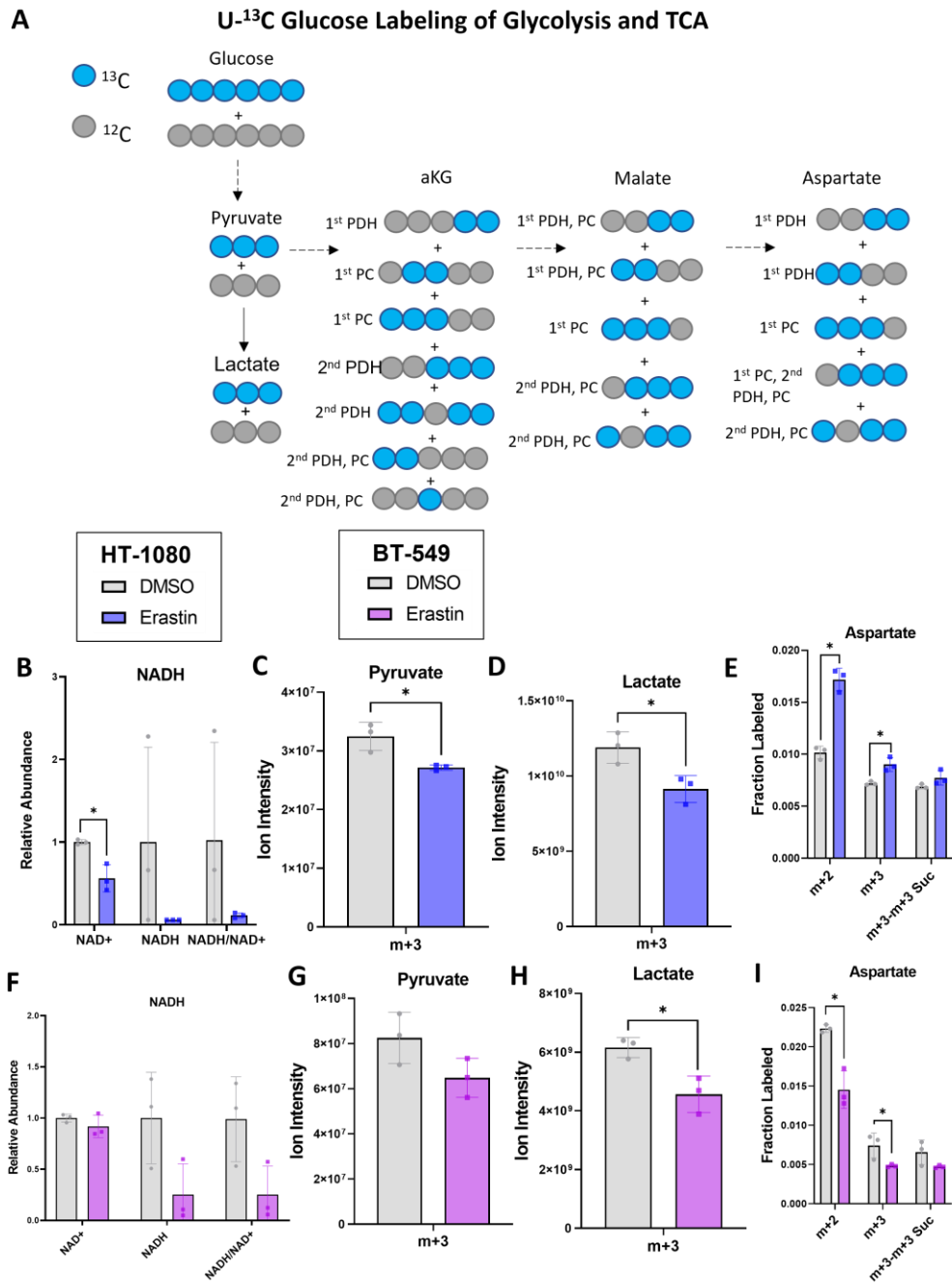
Figure 30: Supplemental-Erastin alters glycolysis and citric acid cycle activity and decreases energy levels

A) Schematic showing labeling of relevant glycolytic and TCA intermediates resulting from U-^{13}C Glucose tracing. PDH means the TCA intermediate's labeling pattern comes from pyruvate entering the TCA through pyruvate dehydrogenase and PC means the TCA intermediate's labeling pattern comes from pyruvate entering the TCA though pyruvate carboxylase. 1st means labeling from the 1st turn of the TCA, 2nd means labeling from the 2nd turn of the TCA. B, F) NAD+ and NADH levels in HT-1080 cells treated with 2.5 μM erastin and BT-549 cells treated with 3.5 μM erastin. C, D, G, H) M+3 pool size for pyruvate and lactate from U-^{13}C Glucose tracing. E, I) Aspartate fractional labeling from U-^{13}C Glucose tracing. m+3-m+3 Suc represents the m+3 fraction of aspartate minus the m+3 fraction of succinate, which represents glucose entry into the TCA via pyruvate carboxylase.

For Figs. B and F a two-way repeated measures ANOVA was performed on log-transformed values and followed by an uncorrected Fisher's LSD test if interaction term or main effect of treatment $p<0.05$. * indicates $p<0.05$ when comparing DMSO to Erastin treatment in Fisher's LSD test and no stars indicates $p>0.05$. For C-E and G-I an unpaired T-test was performed to compare DMSO to erastin treatment. If more than one isotopomer is shown on the graph, a separate uncorrected T-test was performed for each. * indicates $p<0.05$ for this test, no stars shown indicates $p>0.05$.

4.2.4 Exogenous nucleosides rescue viable cell number under erastin treatment

To understand whether depleted nucleotide levels have a functional significance in erastin-induced cell death and/or growth reduction, we co-treated cells with erastin and a nucleoside cocktail (Fig. 31A) that has previously been used to increase viable cell number in cells with diminished nucleotide production[241]. We found that co-treating with exogenous nucleosides caused a small increase in relative viable cell number in erastin-treated HT-1080 cells (Fig. 31B), but a larger nucleoside rescue effect was seen in HT-1080 cells when directly depleting cystine in the media (Fig. 31C). Nucleosides also partially rescued relative viable cell number and restored proliferation in erastin-treated BT-549 cells (Fig. 31D-F). Because nucleosides increased the number of viable cells 3

days after treatment in erastin-treated cells, but not 1 day after treatment (Fig. 31E), the

nucleosides likely increase viable cell number by restoring proliferation rather than by

inhibiting cell death in erastin-treated cells. Nucleosides did not show any rescue effect

in in erastin-treated U2OS cells (Fig. 32G). or in RLS3-treated HT-1080 or BT-549 cells

(Fig. 32H, I), while ferrostatin co-treatment caused a large rescue effect in every cell line

tested that was treated with erastin and RSL3 (Fig. 32A-F). This suggests that the

importance of nucleotide-related changes in affecting cellular fitness during ferroptosis

is likely secondary to other factors and plays a role in certain circumstances. To

understand how nucleosides increase cell proliferation in these circumstances, we

measured cysteine, glutathione, and nucleotide levels in BT-549 cells treated with erastin

with or without nucleoside co-treatment for 15 hours and found that nucleosides do not

alter the level of cysteine or glutathione depletion that is caused by erastin (Fig. 31G).

Nucleoside co-treatment did significantly increase the levels of certain nucleotides,

including GMP, CMP, (Fig. 31H) CDP, (Fig. 31I) and CTP (Fig. 31J), while others

including ADP, UDP, ATP, and dTTP were unaffected. These results show that

exogenous nucleosides can partially rescue nucleotide levels and cell proliferation which

are decreased by erastin in certain cell lines and conditions, suggesting that nucleotide

depletion plays a role in the loss of cellular fitness caused by erastin.
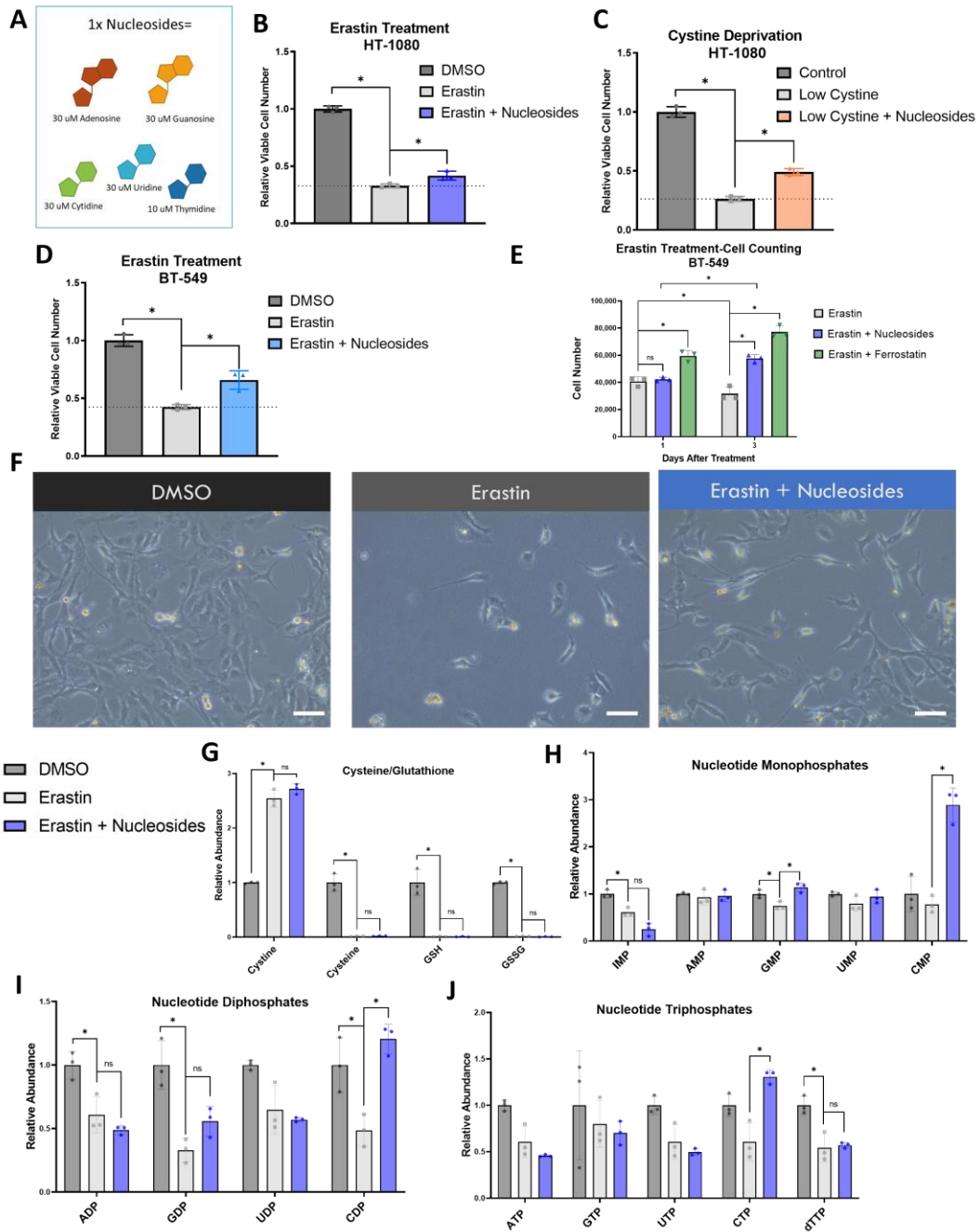
Figure 31: Exogenous nucleosides rescue viable cell number under erastin treatment

A) Identity and concentration of nucleosides in "1x Nucleosides" cocktail. B) Relative viable cell number in HT-1080 cells treated +/- 2.5 μM erastin and 1x nucleosides for 48

119

hours. C) Relative viable cell number in HT-1080 cells cultured in control media or media containing low cystine +/- 1x nucleosides for 48 hours. D) Relative viable cell number in BT-549 cells treated +/- 3.5 μM erastin and 1x nucleosides for 48 hours. E) Cell number as determined by an automated cell counter 24 and 72 hours after treatment with 3.5 μM erastin +/- 1x nucleosides and 0.5 μM Ferrostatin. F) Pictures of BT-549 cells taken after 48 hours +/- 3.5 μM erastin and 1x nucleosides. The scale bar shown is equal to 100 μm G-J) Relative levels of selected metabolites from BT-549 cells treated with 3.5 μM erastin +/- nucleosides.

For Figs. B-D, a one-way ANOVA was performed and followed by an uncorrected Fisher's LSD test when $p < 0.05$ for ANOVA. * indicates $p < 0.05$ in Fisher's LSD test. For E, a two-way ANOVA was performed and followed by an uncorrected Fisher's LSD comparing erastin to erastin + nucleosides and erastin + ferrostatin at each timepoint. Erastin and Erastin + Nucleosides at Day 1 was also compared to Day 3. For Figs. H-K, a two-way repeated measures ANOVA was performed on log-transformed values and followed by an uncorrected Fisher's LSD test if interaction term or main effect of treatment $p < 0.05$. * indicates $p < 0.05$ when comparing Erastin to DMSO or to Erastin + Nucleosides.

Bar is plotted at mean and error bars show standard deviation. Each dot represents one biological replicate.

121
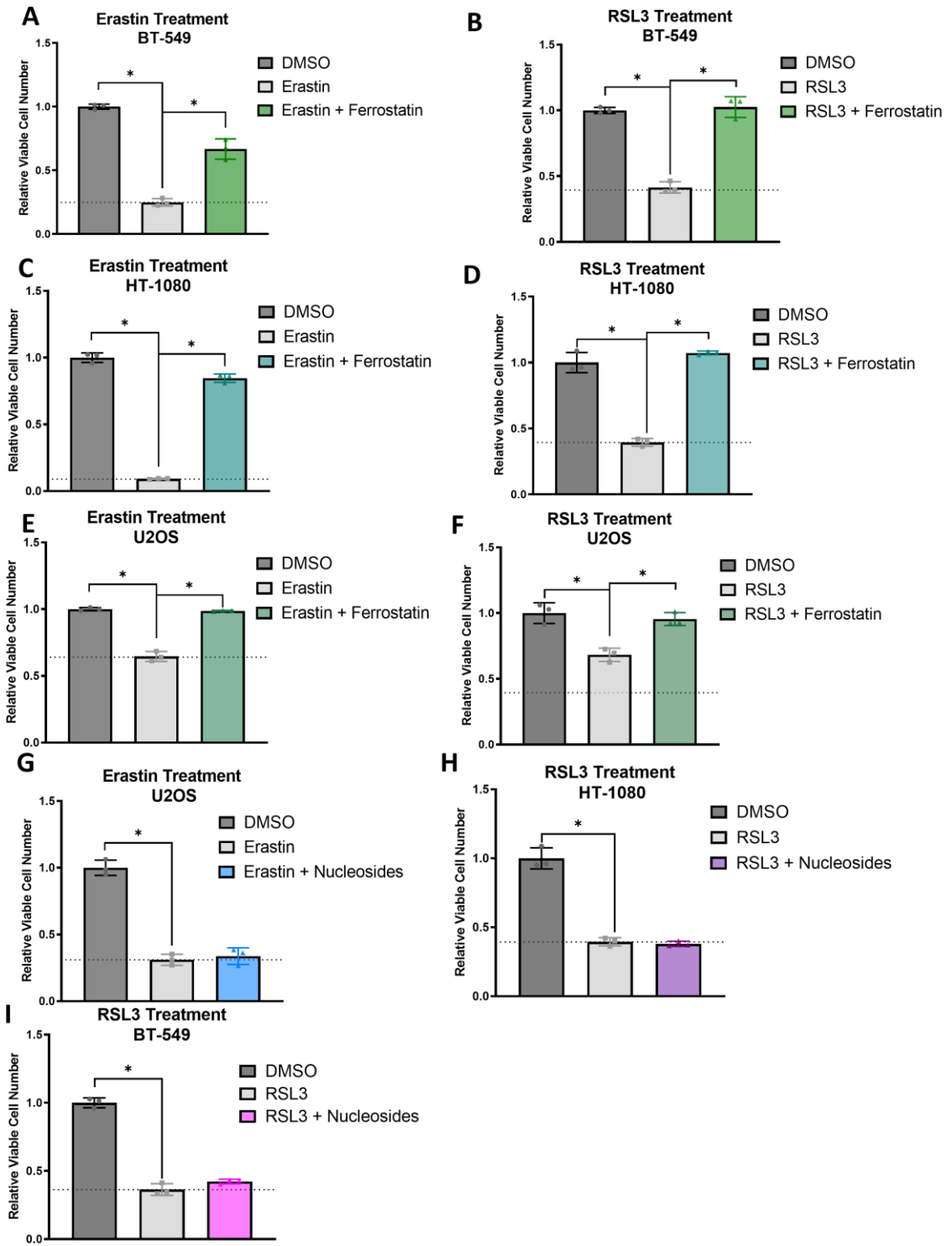
Figure 32: Supplemental-Exogenous nucleosides rescue viable cell number under erastin treatment

Relative viable cell number in:

A) BT-549 cells treated +/- 3.5 µM erastin and 0.5 µM ferrostatin for 48 hours. B) BT-549 cells treated +/- 75 nM RSL3 and 0.5 µM ferrostatin for 48 hours. C) HT-1080 cells treated +/- 5 µM erastin and 0.5 µM ferrostatin for 48 hours. D) HT-1080 cells treated +/- 75 nM RSL3 and 0.5 uM Ferrostatin for 48 hours. . E) U2OS cells treated +/- 5 µM erastin and 0.5 µM ferrostatin for 48 hours. F) U2OS cells treated +/- 1 µM RSL3 and 0.5 µM ferrostatin for 48 hours. G) U2OS cells treated +/- 5 µM erastin and 1x nucleosides for 48 hours. H) HT-1080 cells treated +/- 75 nM RSL3 and 1x nucleosides for 48 hours I) BT-549 cells treated +/- 75 nM RSL3 and 1x nucleosides for 48 hours.

For Figs. A-I a one-way ANOVA was performed and followed by an uncorrected Fisher's LSD test when $p < 0.05$ for ANOVA. * indicates $p < 0.05$ in Fisher's LSD test.

Bar is plotted at mean and error bars show standard deviation. Each dot represents one biological replicate.

4.2.5 Nucleotide and central carbon metabolism are altered in male w1118 *Drosophila melanogaster* fed a cysteine-deprived diet

We next sought to explore an in-vivo model of cysteine and glutathione

depletion to determine: 1) whether glutathione depletion can be achieved through

dietary means and 2) whether similar nucleotide alterations are observed *in vivo* when

cysteine and glutathione are depleted. We speculated that long-term cysteine and

glutathione depletion would decrease fly lifespan. Since cysteine is a conditionally

essential amino acid and can be synthesized from methionine, we did not know whether

dietary cysteine depletion alone would affect fly survival. We therefore depleted

cysteine, methionine, or both in the food of male or virgin female w^{1118} *Drosophila*

melanogaster and assessed survival as compared to flies fed a control chemically defined

122

diet. In male flies, cysteine depletion alone did not affect survival and methionine

depletion alone slightly increased median survival, but the depletion of both dietary

cysteine and methionine significantly decreased median survival (Fig. 33A and B). In

female flies, we saw similar patterns, but changes were not statistically significant (Fig.

34A, B), so we decided to investigate potential dietary-induced metabolic changes in

male flies. We fed male flies a control or cysteine and methionine free chemically

defined diet for three weeks, and then collected fly bodies and heads for separate

metabolic profiling. Fly bodies and heads from flies fed the cysteine and methionine-free

diets showed significantly depleted cysteine and glutathione levels (Fig. 33C and 34C),

demonstrating that diet-mediated glutathione depletion is possible. Next, we assessed

whether nucleotide alterations occurred in cysteine and methionine-deprived flies and

found significant depletions in nucleotide monophosphates in both the fly head (Fig.

34E) and body (Fig. 33E). We also found significant depletions in nucleotide

diphosphates in the fly body (Fig. 33F) but not the head (Fig. 34F). ATP was the only

nucleotide triphosphate that was measured in the flies, but it was not significantly

depleted in the head or body (Fig. 34G and 33G). We also observed significant

differences in citric acid cycle intermediates in both the head and body (Fig. 33H and

34H) and significantly depleted NADH levels in the body (Fig. 33I). We wondered

whether supplementing nucleosides into the diet of cysteine and methionine-deprived

flies could alter survival. We did not know whether this strategy would be effective *in*

vivo since it would depend on the digestion, absorption, and distribution of dietary

nucleosides throughout the body, and because nucleotide depletions may only play a

small role in the decreased survival observed in cysteine and methionine-deprived flies.

However, in light of these complications, supplementing 2.5 mM nucleosides into the

diet caused a small but significant increase in survival of cysteine and methionine-

deprived male flies (Fig. 33J). Together, these data show that long-term dietary cysteine

and glutathione depletion decrease survival and trigger similar *in vivo* metabolic

alterations involving nucleotide metabolism and the citric acid cycle as observed in

cultured cells.
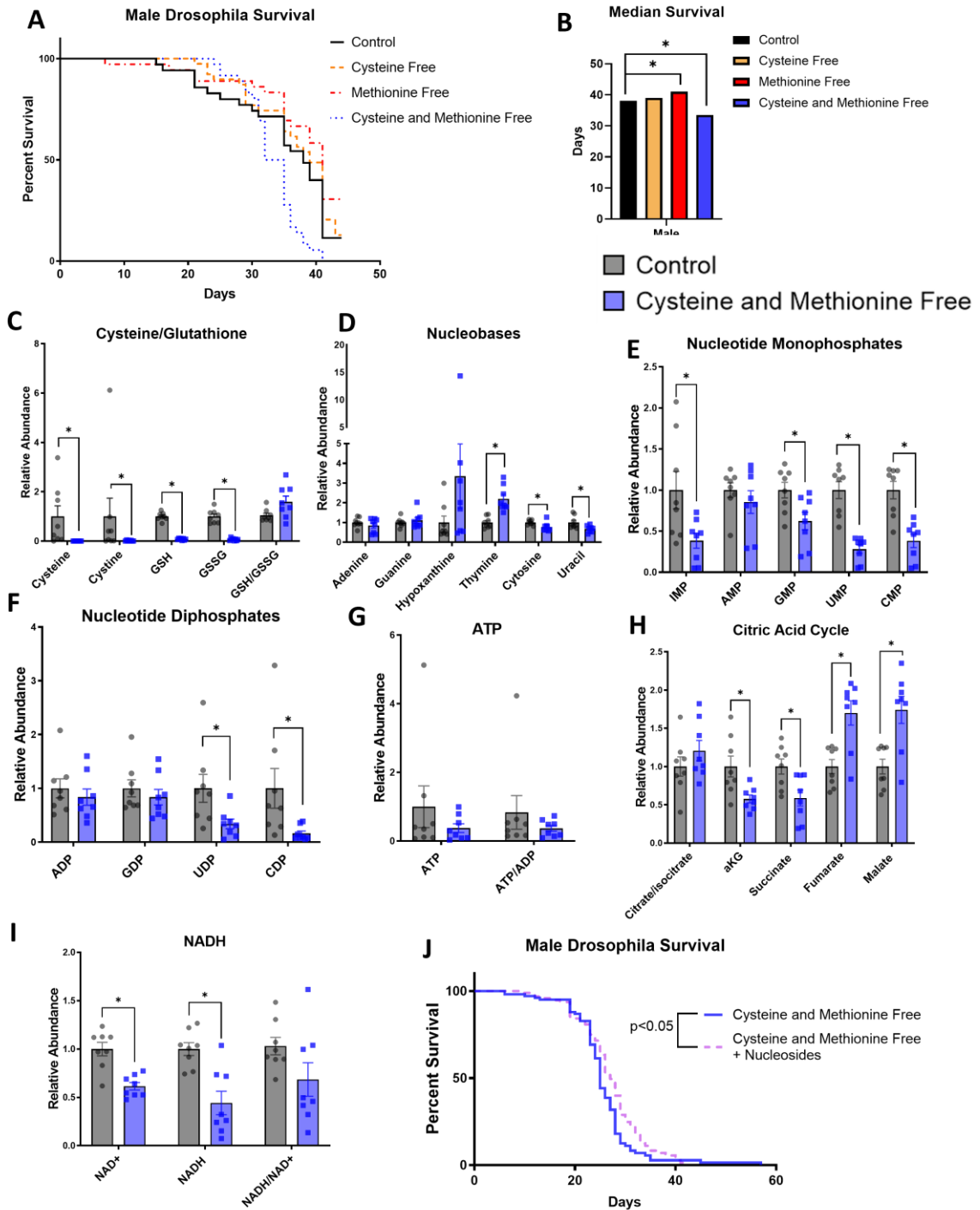
Figure 33: Nucleotide and central carbon metabolism are altered in male w1118
Drosophila melanogaster **fed a cysteine-deprived diet**

A) Male *w1118 drosophila* survival when fed chemically defined diets with or without cysteine and methionine. B) Median survival of male flies from survival curves shown in Fig. 33A.C-I) The relative abundance of selected metabolites from male *drosophila* bodies fed the indicated diets for 3 weeks. Each dot represents one fly. J) Male *w1118 drosophila* survival when fed chemically defined diets without cysteine and methionine +/- nucleosides. Nucleosides added into the diet were Inosine, Uridine, Adenosine, Guanosine, Cytidine, and Thymidine (2.5 mM).

For Fig. B, multiple log-rank Mantel-Cox tests were performed to compare male fly survival differences on control versus cysteine/methionine free diets. * indicates $p < 0.05$ for these tests, while no star indicates $p > 0.05$. For Figs. C-I, a two-way repeated measures ANOVA performed on log-transformed values and followed by an uncorrected Fisher's LSD test if interaction term < 0.05. * indicates $p < 0.05$ for Fisher's LSD test. For Fig. J, a log-rank Mantel-Cox test was performed to compare fly survival on cysteine and methionine free versus cysteine and methionine free + nucleosides diets.
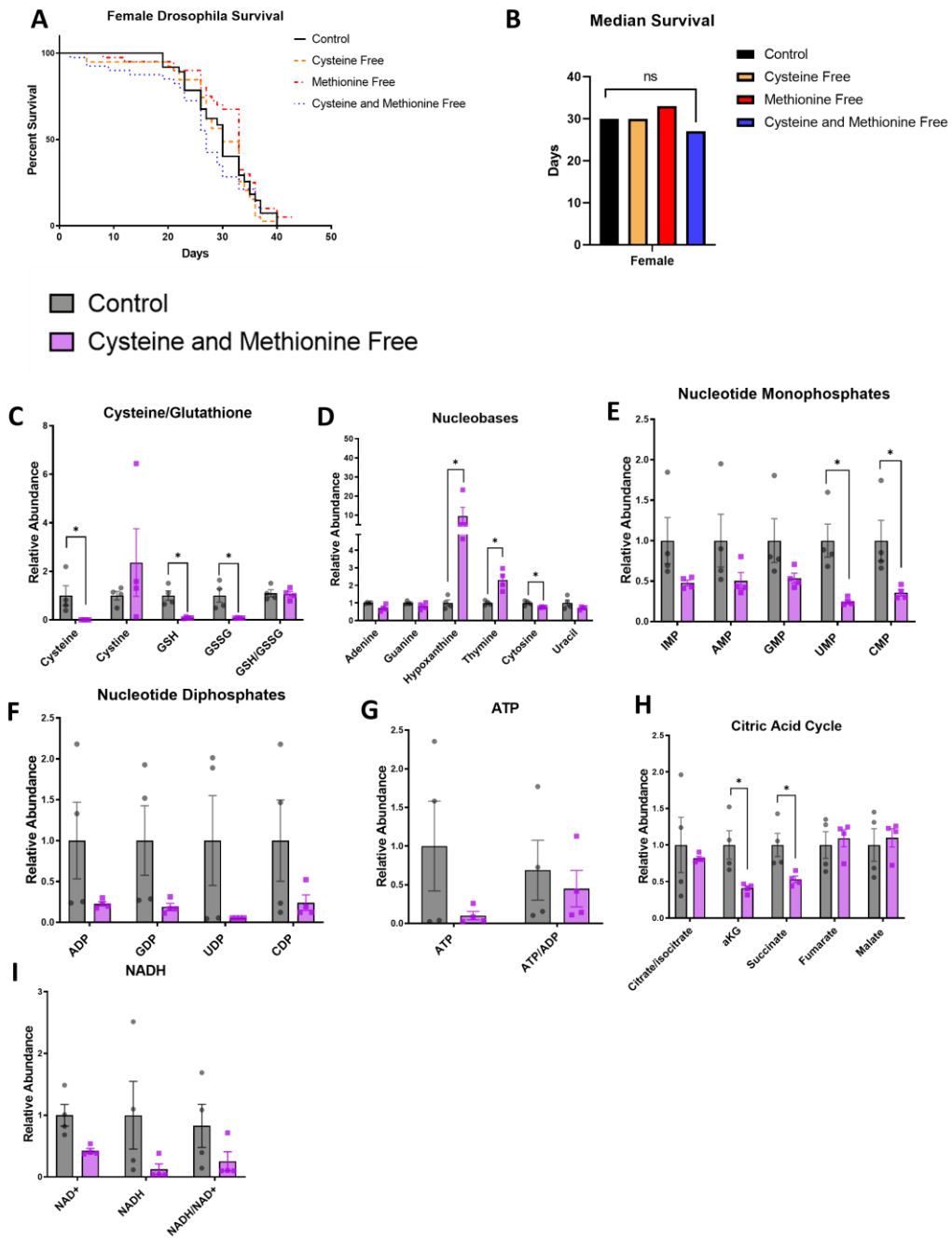
Figure 34: Supplemental-Nucleotide and central carbon metabolism are altered in male w1118 *Drosophila melanogaster* fed a cysteine-deprived diet

A) Virgin female *w1118 drosophila* survival when fed chemically defined diets with or without cysteine and methionine. B) Median survival of female flies from survival

curves shown in Fig. 34A. C-I) The relative abundance of selected metabolites from male *drosophila* heads fed the indicated diets for 3 weeks. Two heads were pooled together, and each dot represents a pooled sample.

For Fig. B, multiple log-rank Mantel-Cox tests were performed to compare female fly survival differences on control versus cysteine/methionine free diets. * indicates $p<0.05$ for these tests, while no star indicates $p>0.05$. For Figs. C-I, a two-way repeated measures ANOVA was performed on log-transformed values and followed by an uncorrected Fisher's LSD test if interaction term <0.05. * indicates $p<0.05$ for Fisher's LSD test. Bars are plotted at mean and error bars show standard deviation.

4.3 Discussion

Previous studies have linked ferroptosis to nucleotide metabolism through dihydroorotate dehydrogenase[242] and through ribonucleotide reductase[243]. Here, we show that alterations in nucleotide metabolism account for some of the largest changes in the metabolome of cells treated with ferroptosis inducers erastin and RSL3. This metabolic profile included alterations which have previously been observed in RSL3-treated cells including depleted pyrimidine precursor N-carbamoyl-L-aspartate and elevated uridine[242], but also showed a much wider set of nucleotide alterations in both erastin and RSL3-treated cells including elevated levels of other nucleosides such as adenosine, guanosine, and cytidine, and broadly depleted nucleotide di- and triphosphate levels.

We investigated two mechanisms through which the nucleotide alterations observed in erastin-treated cells could occur. Tracing with ^{13}C glucose showed that erastin decreases m+5 labeling on pyrimidines in HT-1080 and BT-549 cells, and on

purines in BT-549 cells. Because m+5 ribose was unaffected, decreased *de novo* nucleotide synthesis under erastin treatment is not likely due to altered pentose phosphate pathway activity, and because nucleotides upstream of RNR showed altered labeling, RNR is also unlikely to cause altered nucleotide biosynthesis during erastin treatment. Decreased *de novo* nucleotide synthesis can partially explain why nucleotide depletions occur during erastin treatment, but it does not explain why higher-energy nucleotide di- and triphosphates were depleted while lower-energy nucleotide monophosphates and nucleosides either accumulated or showed smaller depletions. It also does not explain why purines such ADP, GDP, ATP, and GTP were depleted in erastin-treated HT-1080 cells when *de novo* purine synthesis was unaffected. Decreased levels of the ATP/AMP and NADH/NAD+ ratio in erastin-treated cells can better explain why these nucleotides are depleted. Decreased energy production can also affect *de novo* nucleotide synthesis because nucleotide synthesis requires significant energy input[244].

Our study did not directly measure the source of energy depletion during erastin treatment, but the altered ^{13}C glucose labeling seen on glycolysis and TCA intermediates shows that these energy-producing pathways were affected by erastin. Both cell lines showed decreased glycolysis over time under erastin treatment as indicated by altered pyruvate and lactate m+3 pools. This likely contributed to at least some of the energy depletion caused by erastin. Many metabolic enzymes, including several glycolytic and TCA enzymes, are affected by reactive oxygen species[245], and the significant glutathione

depletion caused by erastin treatment is likely to affect one or more of these enzymes through loss of redox homeostasis[246]. Lipid peroxidation has been observed in mitochondria[185,187] and could also target enzymes in these and other pathways. A limitation of the study was only focusing on possible mechanisms of erastin-induced nucleotide alterations and not those of other ferroptosis inducers such as RSL3.

Previous studies have found that increased ROS generation by mitochondria can contribute to ferroptosis[247,248] and that erastin-induced ferroptosis can be inhibited by suppressing the TCA[185]. It has also been suggested that erastin increases mitochondrial metabolism through the opening of voltage-dependent anion channels in the outer mitochondrial membrane[247]. Our study found that TCA intermediates were depleted in erastin-treated HT-1080 and BT-549 cells. However, the two cell lines had opposite patterns in terms of ^{13}C glucose labeling of TCA intermediates through pyruvate dehydrogenase, with HT-1080 cells showing increased glucose usage in the TCA and BT-549 cells showing decreased. Increased glucose usage in the TCA in erastin-treated HT-1080 cells may partially compensate for loss of glycolytic activity or decreased use of other TCA fuel sources. We did not determine whether blocking mitochondrial metabolism contributed to or suppressed erastin-induced cell death, but our results do show that mitochondrial metabolism is affected differently in different cell lines, and caution should be used when generalizing the results obtained from a single model.

Our results show that a major effect of erastin-treated cells is nucleotide depletion, and that supplementing erastin-treated cells with exogenous nucleosides can partially rescue cell proliferation at intermediate doses of erastin. These results indicate that the nucleotide changes observed in the metabolic profile of erastin-treated cells have a functional impact on cellular fitness. Restored nucleotide levels likely improve the rates of macromolecule biosynthesis and repair[244]. Glutathione depletion by erastin and other methods has shown to synergize with numerous chemotherapies including those that interfere with nucleotide synthesis[249]. Our study offers a plausible mechanism for why these synergisms occur. RSL3-treated cells showed a very similar metabolic profile to erastin-treated cells, but exogenous nucleosides did not rescue viable cell number under RSL3 treatment in any cell line tested. We did not investigate why this is but speculate that it may have to do with differences in the onset, strength, and location of lipid peroxidation caused by erastin versus RSL3. The efficacy of whether the exogenous nucleoside cocktail rescues viable cell number and nucleotide levels in erastin-treated cells likely depends on several factors including the extent to which nucleotide depletions are caused by insufficient de novo nucleotide production and salvage versus insufficient energy levels, the speed and ability of cells to salvage the nucleosides from the cocktail, and the role reduced nucleotide levels play in decreasing cellular fitness in different cell lines and conditions.

Our study also showed that glutathione depletion can be achieved through dietary methods. Long-term cysteine and methionine restriction significantly decreased the lifespan of male flies and had a similar effect on virgin female flies that was not statistically significant. We also observed similar nucleotide and TCA cycle changes in the metabolic profile of male flies subjected to a cysteine and methionine-free diet as seen in cultured cancer cells treated with erastin. Because ferroptosis has been implicated in neurological disease[177,250], we questioned whether the metabolic profile of fly heads would differ from fly bodies but found almost identical metabolic changes. Supplementing nucleosides into the diet of the cysteine-deprived cells caused a small but statistically significant increase in median survival, suggesting that the nucleotide depletions observed in the metabolic profile of cysteine-deprived cells may play a role in their decreased survival.

In summary, our study shows that nucleotide metabolism is a target of ferroptosis which can play a role in diminished survival and proliferation in certain contexts. Further, it also establishes that glutathione depletion causes alterations to nucleotide synthesis through several mechanisms but not entirely through a single step involving an enzyme such as RNR or DHODH. Given these links many questions in disease biology such as cancer and neuropathology are open for further investigation.

4.4 Methods

4.4.1 Cell Culture

BT-549, HT-1080, and U2OS cells were purchased from the Duke Cell Culture Facility and cultured in RPMI 1640 (Gibco) supplemented with 10% heat-inactivated fetal bovine serum (Sigma, F2442). Cells were cultured in a 37 °C, 5% CO_2 atmosphere. All cell lines tested negative for mycoplasma contamination.

4.4.2 Cell Viability Assays

Cells were seeded at a density of 2-4 x 10^3 cells per well in 96-well plates with water in the outside wells and allowed to adhere overnight. Cells were treated the following day by replacing the seeding media with 100 μL treatment media containing drug treatments or nutrient restricted media and any rescue agents. Cells were incubated in treatment media for the indicated period of time and then MTS reagent ((3-(4,5-dimethylthiazol-2-yl)-5-(3-carboxymethoxyphenyl)-2-(4-sulfophenyl)-2H-tetrazolium) purchased from Abcam, (ab197010) was mixed 1:1 with sterile PBS and 20 μL of the mixture was added to each well. Cells were incubated with MTS reagent for 2 hours, and after brief shaking absorbance was read at 490 nm on a microplate reader.

4.4.3 IC_{50} Dose Determinations

For each cell line, IC_{50} doses of erastin and RSL3 were determined by seeding cells at a density of 2-4 x 10^3 cells per well in 96-well plates with water in the outside wells. Doses of erastin ranging from 0-50 μM were added to wells in triplicate, and

doses of RSL3 ranging from 0-1.5 μM were added to wells in triplicate. Cells were

incubated with erastin/RSL3 for 24 hours, and then MTS cell viability assays were

performed as previously described. IC_{50} dose curves were plotted and an IC_{50} dose for

each drug in each cell line was calculated based off the curve.

4.4.4 Drugs and Rescue Agents

Erastin (17754), RSL3 (19288), and Ferrostatin-1 (17729) were purchased from

Cayman Chemical. The "1x nucleosides" were EmbryoMax Nucleosides purchased from

MilliporeSigma (ES-008-D).

4.4.5 Cystine Deprivation

Low cystine media was made from RPMI without L-glutamine, L-cystine, L-

methionine, and L-cysteine (MP Biomedicals 1646454) supplemented with 10% dialyzed

heat-inactivated fetal bovine serum (VWR SH30079.03). L-methionine (Amresco E801)

and L-glutamine (Amresco 0374) were added back to the media to the concentration

found in RPMI 1640 and L-Cystine (Amresco J993) was added back to control media but

not to cystine free media. Both control and cystine free media were adjusted to pH 7.4

and then sterilized using a 0.10 μm filter (MilliporeSigma S2VPU02RE). To find an

equivalent level of cystine deprivation that matched the level of cell

viability/proliferation reduction caused by erastin in HT-1080 cells, we added varying

levels of control media to the cystine free media and measured cell viability after 24

hours (the same way IC_{50} doses of erastin were found) and selected 7.5% cystine for the low-cystine media used in the rescue experiment.

4.4.6 Cell Counting

Cells were seeded at a density of 4×10^4 cells per well in six-well plates and allowed to adhere overnight. Cells were treated the following day by replacing media with 2 mL treatment media containing drug treatments and rescue agents. After 1 or 3 days of treatment, cells were trypsinized and then counted on a MOXI Z automated cell counter (Orflo).

4.4.7 Microscopy

Cells were seeded at a density of 8×10^4 cells per well in six-well plates and allowed to adhere overnight prior to treatment. Cells were incubated in treatment media for 48 hours prior to imaging. Images were captured using a Leica DM IL LED microscope equipped with a Leica MC170HD camera at x10 objective using LAS EZ software (Leica). Scale bars = 100 μm.

4.4.8 Stable Isotope Labeling

Cells were seeded at 8×10^4 cells per well into six-well plates and allowed to adhere overnight prior to treatment. Treatment media was added to cells for 4 hours, and then replaced with U-^{13}C Glucose-containing treatment media, which cells were cultured in for 12 hours. The U-^{13}C Glucose-containing treatment media was made from glucose-free RPMI (Gibco 11879-020) supplemented with 10% heat-inactivated fetal

bovine serum (Sigma, F2442) with [U-13C] glucose (Cambridge Isotope Laboratories,

#CLM-1396) added at 2 g/L. Metabolites were then extracted and measured via LC-MS

according to the protocols below.

4.4.9 Polar Metabolite Extraction from Cells

Polar metabolite extraction was conducted as previously described[206,234]. Briefly,

8-12 x 10⁴ cells per well were seeded into six-well plates and allowed to adhere

overnight prior to treatment.

Cell confluence was equal across conditions at the time of extraction. Following

treatment, medium was quickly aspirated, plates were placed on dry ice, and 1 mL of

80% methanol/water extraction solvent (Optima LC-MS grade, Fisher; methanol, #A456;

water, #W6) pre-cooled to −80°C was immediately added to each well prior to

transferring the plates to −80 °C for 15 min. The plates were then removed, placed on

dry ice, and the cells were scraped into the extraction solvent and transferred to

Eppendorf tubes. Metabolite extracts were then centrifuged at 20,000 × g at 4 °C for 10

min. The solvent in each sample was then transferred to a new Eppendorf tube and

evaporated using a speed vacuum.

4.4.10 Polar Metabolite Extraction from Flies

Flies were immobilized on ice and fly heads were separated from the thorax and

abdomen ("body") using tweezers, then both the head and both were flash-frozen in

Eppendorf tubes using liquid nitrogen. Two heads a diet group were pooled together to

have enough material for extraction. During extraction, the Eppendorf tubes were placed on dry ice and 200 μL 80% methanol pre-cooled to −80°C was added to each tube. The fly bodies and pooled heads were then homogenized using a tissue homogenizer. After homogenization, an additional 300 μL pre-cooled 80% methanol was added to each tube and tubes were vortexed and then centrifuged at 20,000 × g at 4 °C for 10 min. The solvent in each sample was then transferred to a new Eppendorf tube and evaporated using a speed vacuum. (note: solvents were the same as used in Polar Metabolite Extraction from Cells.

4.4.11 Liquid chromatography

For polar metabolite analysis, the evaporated cell extracts were first dissolved in 15 μL LC-MS grade water and then15 μL methanol/acetonitrile (1:1 v/v) (Optima LC-MS grade, Fisher; methanol, #A456; acetonitrile, #A955) was added. Finally, samples were centrifuged at 20,000 × g at 4 °C for 10 min, and the supernatants were transferred to LC vials prior to HPLC injection (3 μL).

An XBridge amide column (100 x 2.1-mm inner diameter, 3.5 μm; Waters) was used on a Dionex (Ultimate 3000 UHPLC) for compound separation at room temperature. Mobile phase A was water with 5 mM ammonium acetate, pH 6.9, and mobile phase B was 100% acetonitrile. The gradient is linear as follows: 0 min, 85% B; 1.5 min, 85% B; 5.5 min, 35% B; 10 min, 35% B; 10.5 min, 35% B; 10.6 min, 10% B; 12.5 min, 10% B; 13.5 min, 85% B; and 20 min, 85% B. The flow rate was 0.15 ml/min from 0 to 5.5

min, 0.17 ml/min from 6.9 to 10.5 min, 0.3 ml/min from 10.6 to 17.9 min, and 0.15 ml/min

from 18 to 20 min. All solvents are LC-MS grade and were purchased from Fisher.

4.4.12 Mass spectrometry

The Q Exactive Plus mass spectrometer (Thermo Scientific) is equipped with a

heated electrospray ionization probe, and the relevant parameters are listed: evaporation

temperature,

120 °C; sheath gas, 30; auxiliary gas, 10; sweep gas, 3; spray voltage, 3.6 kV for

positive mode and 2.5 kV for negative mode. Capillary temperature was set at 320 °C,

and S lens was 55. A full scan range from 70 to 900 (m/z) was used. The resolution was

set at 70,000. The maximum injection time was 200 ms. Automated gain control was

targeted at 3×10^6 ions.

4.4.13 Peak extraction and data analysis

Raw data collected from LC-Q Exactive Plus MS was processed on Sieve 2.0

(Thermo Scientific). Peak alignment and detection were performed according to the

protocol described by Thermo Scientific. For a targeted metabolite analysis, the method

"peak alignment and frame extraction" was applied. An input file of theoretical m/z and

detected retention time was used for targeted metabolite analysis, and the m/z width

was set to 5 ppm. An output file including detected m/z and relative intensity in

different samples was obtained after data processing. If the lowest integrated mass

spectrometer signal (MS intensity) was less than 1,000 and the highest signal was less

than 10,000, then this metabolite was considered below the detection limit and excluded

for further data analysis. If the lowest signal was less than 1,000, but the highest signal

was more than 10,000, then a value of 1,000 was imputed for the lowest signals. For

isotope tracing experiments, the mass isotopomer distributions were calculated and

normalized by comparing the ratio of labeled to unlabeled metabolites in each sample.

4.4.14 Fly stocks and maintenance

w^{1118} stocks were kindly provided by Dr. Don Fox. Flies were maintained on

Nutri-fly food (Genesee Scientific 66-112) at room temperature between experiments.

4.4.15 Fly Survival

Newly emerged adult male and virgin female flies were collected and sorted

under CO_2 anesthesia for three days prior to the start of survival experiments. On day 0,

flies were again subjected to CO_2 anesthesia to be randomized to their diet group and

were put onto food containing their assigned diet (male and female flies were kept in

separate vials with 30-40 flies/vial at the start of the experiment). During the experiment,

flies were moved to a new vial of food every 3-4 days. Vials were visually inspected for

dead flies and deaths were recorded daily each week from Monday-Friday. Flies were

reared on benchtops at room temperature, with each different diet group subjected to

the same conditions.

4.4.16 *Drosophila* Chemically Defined Diets

Drosophila diet formulations were derived from previous recipes[251,252] with the following modifications: (1) the type of Agar (Micropropagation Agar-Type II; Caisson Laboratories #A037), (2) the final percentage of Agar (1%), 3) the amount of sucrose (25 g), 4) the amino acids that were added to stock solutions before or after autoclaving[253] whose order is described below and 5) the exclusion of inosine and uridine from the all diets except for the "cysteine and methionine free + nucleosides diet", which contained 2.5 mM inosine, uridine, adenosine, guanosine, cytidine, and thymidine added into the "Other Nutrients" solution. The amino acid composition of the diet were based on the exome-matched (i.e. the concentrations used for a given amino acid correspond with the prevalence of exons for that amino acid in the Drosophila genome) Drosophila diet formulation developed in a previous study[252] that was found to be optimal for growth and fecundity without compromising lifespan. The rationale for which amino acids were part of the autoclaving process was based on solubility considerations[253].

The complete procedure, formula, and stock solutions for food production are as follows:

Procedure:

1) Prepare "Part 2" (see below) Mixture and set aside;

2) Prepare "Part 1" (see below) Mixture, adding everything but agar (not everything will go into solution at this point);

3) Add agar to "Part 1" Mixture, stir using stir bar;

4) Autoclave "Part 1" Mixture for 15 minutes;

5) Remove "Part 1" Mixture from autoclave, then combine with "Part 2" Mixture and stir;

6) Quickly pipette food into Drosophila vials (5-10 mL food/vial);

7) Allow food to solidify/cool for roughly an hour, then cover vials (either with cotton

plugs or with plastic wrap) and store food at 4°C.

Food is good for about one month at 4°C (will shrink and pull away from sides of vials due to loss of water after this).

Note:

After autoclaving, "Part 1" Mixture containing agar can start solidifying (both before and after the two mixtures are combined, but combining the two mixtures will cause food to cool down quite a bit and solidify faster). Quickly combine and pour food while autoclaved mixture is still hot to avoid this. Adding water to the autoclave tray

and keeping the "Part 1" Mixture in this hot water until ready to combine and pour

helps keep it hot and helps prevent premature solidification.

Table 1: Drosophila Chemically Defined Diet Recipe Part 1 & 2

	Category	Ingredient	Amount of stock per liter
Part 1			
	Gelling Agent	Agar-Type II	10 g
	Sugar	Sucrose	25 g
	Metal Ions	CaCl2*6h2o	1 mL
		CuSO4*5h2o	1 mL
		FeSO4*7h2o	1 mL
		MgSO4 (anhydrous)	1 mL
		MnCl2*4h2o	1 mL
		ZnSO4*7h2o	1 mL
	Cholesterol	Cholesterol	15 mL
	Amino Acids	Tyrosine	0.93g
	Amino Acids	Histidine	50 mL
		Isoleucine	50 mL
		Methionine	50 mL
		Phenylalanine	50 mL
		Threonine	50 mL
		Valine	50 mL
	Water	Water (milliQ)	158 mL

**AUTOCLAVE 15 minutes

	Category	Ingredient	Amount of stock per liter
Part 2			

Base	Buffer	100 ml
Amino Acids	Arginine	10 mL
	Cysteine	10 mL
	Glutamate	10 mL
	Glycine	10 mL
	Lysine	10 mL
	Proline	10 mL
	Serine	10 mL
Amino Acids	Alanine	50 mL
	Asparagine	50 mL
	Aspartate	50 mL
	Glutamine	50 mL
	Leucine	50 mL
	Tryptophan	50 mL
Vitamin Solution		21 mL
Folic Acid	Folic Acid	1 mL
Other Nutrients Solution		8 mL
Preservatives	Propionic acid	6 mL
	methyl 4-hydroxybenzoate	15 mL

Table 2: Stock Solutions for Drosophila Chemically Defined Diet

Amino Acids	Catalog Number	g/50mL	Suspend in:
L-Alanine	Sigma, A7469	1.10	H2O
L-Asparagine	Amresco, 94341	1.03	H2O
L-Aspartic Acid	Alfa Aesar, A13520	1.17	0.5N NaOH
L-Glutamine	Amresco, 0374	1.12	H2O
L-Histidine	Amresco, 1B1164	0.65	H2O
L-Isoleucine	Amresco, E803	1.12	H2O
L-Leucine	Sigma, L8912	2.03	0.2N HCl
L-Methionine	Amresco, E801	0.60	H2O
L-Phenylalanine	Sigma, P5482	1.01	H2O
L-Threonine	Sigma, T8441	1.11	H2O

L-Tryptophan	Amresco, E800	0.32	H2O
L-Valine	Amresco, 1B1102	1.20	H2O
L-Arginine HCl	Amresco, 0877	8.16	H2O
L-Cysteine	Sigma, 30089	1.71	1N HCl
L-Glutamic acid	Alfa Aesar, A12919	7.59	H2O
L-Glycine	Alfa Aesar, A13816	3.84	H2O
L-Lysine HCl	Amresco, 0437	6.83	H2O
L-Proline	Sigma, P5607	4.89	H2O
L-Serine	Sigma, S4311	6.89	H2O
L-Tyrosine	Sigma, T8566	**add Tyr powder	
Vitamin solution	**Catalog Number**	**g/50mL**	**Suspend in:**
Biotin	Sigma, B4501	0.001	H2O
Ca pantothenate	Sigma, 21210	0.039	H2O
Nicotinic acid	Sigma, N4126	0.030	H2O
Pyridoxine HCl	Sigma, P9755	0.006	H2O
Riboflavin	Sigma, R4500	0.003	H2O
Thiamine (aneurin)	Sigma, T4625	0.005	H2O
Folic acid solution	**Catalog Number**	**g/50mL**	**Suspend in:**
Folic acid	Sigma F8758	0.0250	0.004N NaOH
Other Nutrients solution	**Catalog Number**	**g/50mL**	**Suspend in:**
Choline chloride	MP Biomedicals, 194639	0.3125	H2O
Myo-Inositol	Sigma, I7508	0.0315	H2O
Methyl 4-hydroxybenzoate solution	**Catalog Number**	**g/50mL**	**Suspend in:**
Methyl 4-hydroxybenzoate	Sigma, H3647	5.0	95% EtOH
Buffer	**Catalog Number**	**50mL stock**	
Glacial Acetic Acid	Millipore, AX0074	1.5 mL	
KH2PO4	JT Baker, 3246	1.5 g	
NaHCO3	Sigma, S8875	0.5 g	
Water		Up to 50mL	
Metal Ions	**Catalog Number**	**g/50mL**	**Suspend in:**
CaCl2*6h2o	Sigma, 21108	12.5	H2O
CuSO4*5h2o	Sigma, C7631	0.125	H2O
FeSO4*7h2o	Sigma, F7002	1.25	H2O (store -20C)
MgSO4 (anhydrous)	Sigma, M7506	12.5	H2O
MnCl2*4h2o	Sigma, M3634	0.05	H2O
ZnSO4*7h2o	Sigma, Z0251	1.25	H2O
Cholesterol solution	**Catalog Number**	**g/50mL**	**Suspend in:**
Cholesterol	Sigma, C8253	1	EtOH

Catalog Numbers for other reagents:

Sucrose: Sigma, S7903

Agar: Caisson, A037

Propionic acid: Sigma, P5561

Inosine: Sigma, I4125

Uridine: Sigma,U3003

Adenosine: Sigma, A4036

Guanosine: Sigma, G6264

Cytidine: Sigma, C4654

Thymidine: Sigma, T1895

Stocks can be stored at 4°C for several months unless otherwise specified.

4.4.17 Statistics

Details on individual statistical tests are described in figure legends. Unless stated otherwise, bar graphs plot the mean and error bars show standard deviation. Individual dots represent one biological replicate.

5. Dietary impact on mouse metabolism and physiology

5.1 Background and Context

As discussed in Sections 1.3 and 1.4, diet can have profound effects on health and aging. Diet can change metabolism, which in turn impacts health and physiology. Calorie restriction, protein restriction, methionine restriction, and ketogenic diet are all dietary interventions which have been investigated for their potential ability to increase lifespan (Section 1.4.1-1.4.4), but the metabolic effects of these diets could be better understood. One outstanding question is whether each of these diets impacts health and metabolism in a unique way, or whether multiple diets convergently affect the same metabolic pathways. We sought to investigate this question by metabolically profiling the blood and tissues of mice fed these diets or a control diet.

We also wanted to explore the impact of these diets on tissue-specific glucose usage. Tissues are known to prefer certain nutrients as energy and anaplerotic sources[227,254,255], however the extent to which these preferences are impacted by diet is unknown. Recently, *in-vivo* isotope labeling studies combined with metabolomics and a mathematical method called metabolic flux analysis (MFA)[256,257] have allowed for better measurement of tissue-specific nutrient usage and nutrient circulatory flux[258-260]. Flux measurements also offer more specific information about metabolic activity than simple metabolite level measurements, because flux defines actual metabolic pathway activity, whereas metabolite levels can only offer clues to pathway activity[257]. We therefore

wanted to employ these techniques to determine whether diet influences nutrient circulatory flux and tissue-specific glucose usage in pathways such as the citric acid cycle. While this study is still on-going, we expect the final results to better define how basic physiology is impacted by diet, and also offer mechanisms through which diet can impact diseases such as cancer.

5.2 Results

5.2.1 Study setup and preliminary physiological findings

To study the effects diet on whole-body metabolism and physiology, in collaboration with the Vanderbilt Mouse Metabolic Phenotyping Center, we divided 40 twelve-week-old female C57BL/6J mice into five diet groups: Control, 20% Calorie Restriction (CR), Low Protein (LP), Ketogenic Diet (KD), and Methionine Restriction (MR) (Fig. 35A-C, Table 3). To control feeding, mice were singly housed, and all diet groups except for CR were fed an eucaloric equivalent to 2.7 g of control mouse food a day, which was determined to be the average ad-libitum amount of food consumed by these mice fed our control diet before the start of the study. Mice were weighed weekly, and mice fed the KD weighed more than control mice throughout the study despite consuming the same number of calories as control mice (Fig. 36A). This was not necessarily unexpected, as there have been conflicting reports of whether KD causes weight gain[157,160] or not[156,161]. CR mice weighed less than control mice, and mice fed low-protein (LP) and methionine restricted (MR) diets did not have significantly different

weights than control mice throughout the study (Fig. 36A). The body composition, blood

pressure, and heart rate of mice were measured 10 weeks after starting the diets. CR and

KD mice had a significantly higher body fat percentage than control mice (Fig. 36B).

Increased body fat percentage in female C57BL/6J mice fed a 20% CR diet has previously

been observed and is thought to play a protective effect[261,262]. No significant

cardiovascular differences were observed between diet groups (Fig. 36C and D),

although CR mice tended to have lower heart rates. The lack of differences between

groups may be due to the relatively young age (22 weeks) of mice at the time of the test

and the relatively short duration of dietary intervention in our study compared to other

studies[131]. We did, however, observe that CR, MR, and LP diets significantly decreased

fasting blood glucose levels as compared to control mice (37A and B). Despite the

extreme limitation of dietary carbohydrates, KD mice did not have lower fasting blood

glucose levels, but their blood glucose was significantly lower than control mice

postprandially (Fig. 37B). KD mice also had dramatically worsened glucose tolerance

(Fig. 37 C and D), which has previously been reported[160]. In summary, these physiologic

tests showed that our dietary interventions produced effects that are mostly consistent

with what has previously been reported. Other physiologic data, including respiratory

quotient, energy expenditure, and exercise stress tests, are still being analyzed.
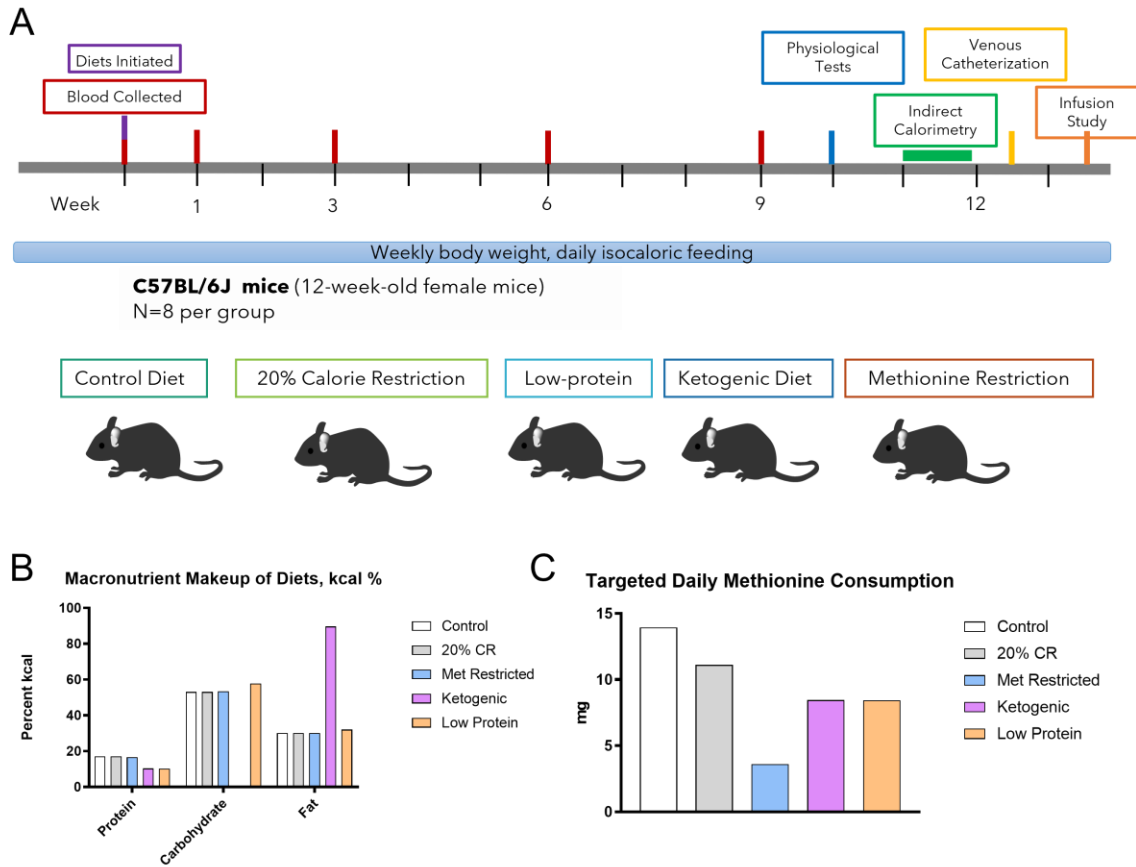
Figure 35: Study design

A) Schematic showing diet groups and timeline of study. B) Caloric composition of each diet used in the study C) Amount of methionine to be consumed by mice in different diet groups each day based on the methionine content of their food and the amount of food they were given.
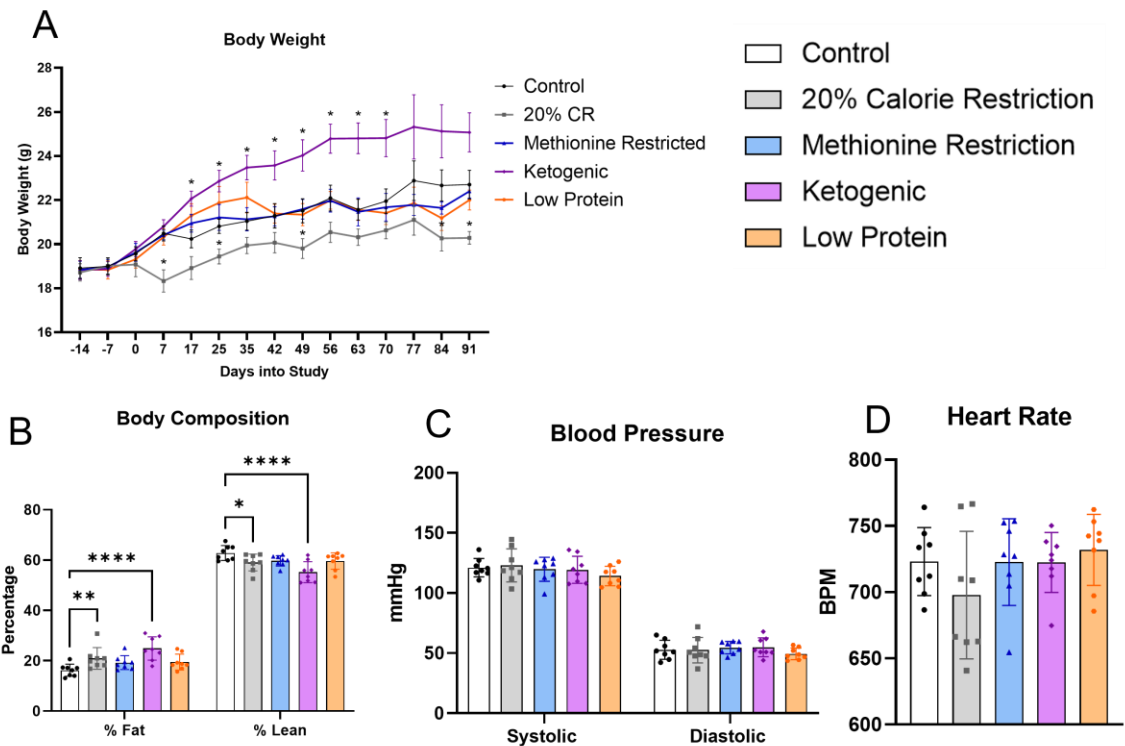
Figure 36: Physiologic effects of diets

A) Body weights of mice throughout the study. B) Body composition as measured on week 11 after diet initiation by quantitative magnetic resonance C) Blood pressure and D) heart rate as measured on week 9 after diet initiation

For A, a two-way repeated measures ANOVA was performed and followed by an uncorrected Fisher's LSD test which compared the weight of control mice vs the weight of every other diet at each timepoint if interaction term was significant. *$p<0.05$ for Fisher's LSD test.

For B and C, a two-way repeated measures ANOVA was performed and followed by an uncorrected Fisher's LSD test which compared control mice to other diet groups if interaction term was significant. *$p<0.05$, **$p<0.01$, ***$p<0.001$, ****$p<0.0001$ for Fisher's LSD test.

For D, a one-way ANOVA was performed and found no significant difference among means.
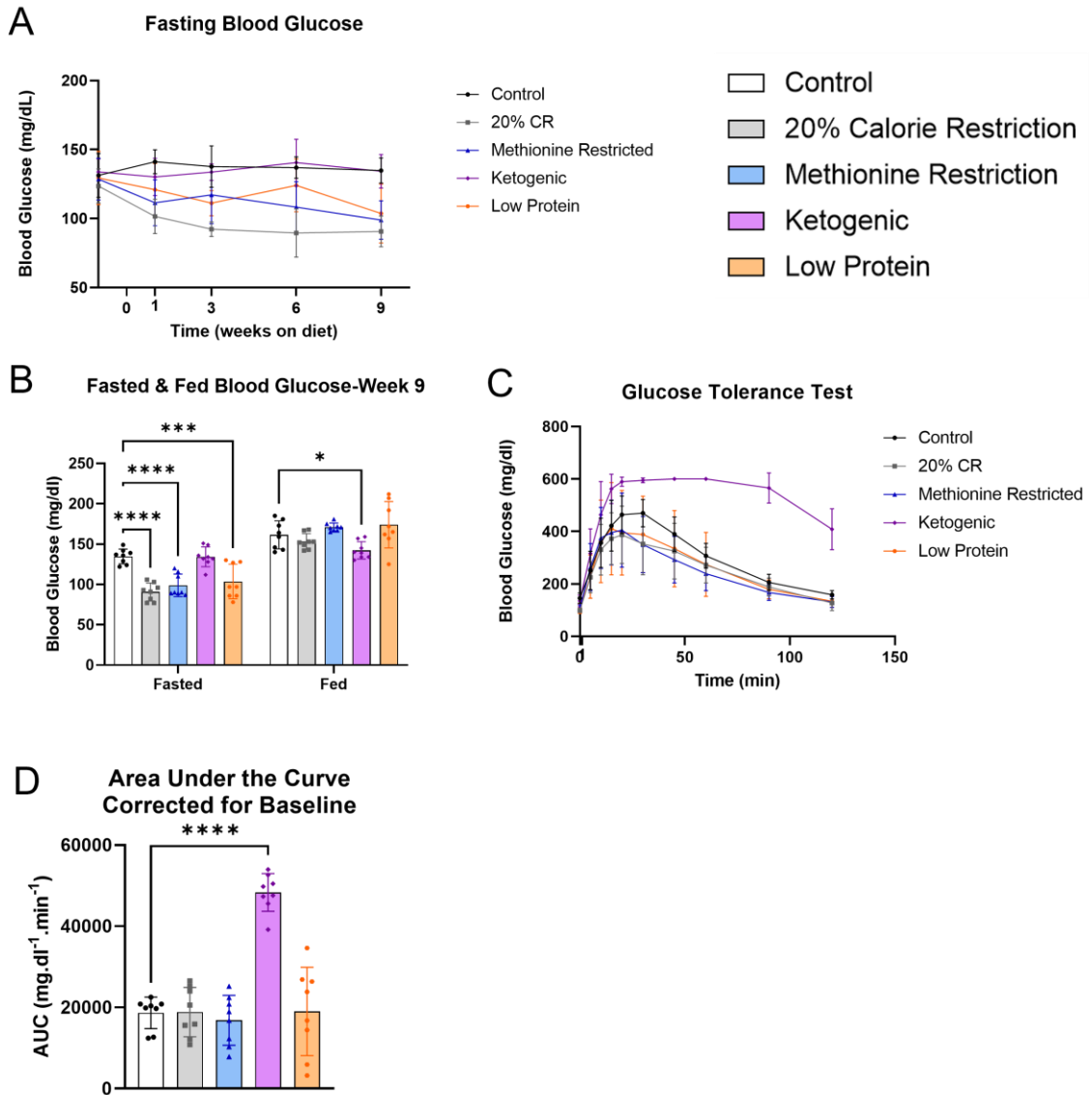
Figure 37: Dietary effects on blood glucose and glucose tolerance

A) Fasting blood glucose levels as measured by glucometer throughout the study. B) Blood glucose levels as measured by glucometer 9 weeks after diet initiation C) Blood glucose levels over time after intraperitoneal injection of 2g/kg glucose. 600 mg/dL was the upper detection limit of the glucometer. D) Area under the curve from C.

For B, a two-way repeated measures ANOVA was performed and followed by an uncorrected Fisher's LSD test which compared control mice to other diet groups if interaction term was significant. *p<0.05, **p<0.01, ***p<0.001, ****p<0.0001 for Fisher's LSD test.

For D, a one-way ANOVA was performed and followed by an uncorrected Fisher's LSD test which compared control mice to other diet groups if interaction term was significant. *$p<0.05$, **$p<0.01$, ***$p<0.001$, ****$p<0.0001$ for Fisher's LSD test.

Blood plasma was collected from mice at multiple timepoints throughout the study and analyzed by LC-MS. We looked at the methionine levels and at the levels of ketone bodies acetoacetate and beta-hydroxybutyrate after 1, 3, and 9 weeks of diet initiation to assess whether methionine restriction and ketogenic diet caused their expected effects. Methionine levels were marginally lower in the plasma of MR mice while fasting and in the fed state after 1 week, but significantly lower in the fed state at 3 and 9 weeks (Fig. 38A-C). Decreased methionine levels were also observed in KD and LP mice after feeding at these timepoints. Acetoacetate and beta-hydroxybutyrate levels were significantly increased in KD mice in both fasting and fed states at all timepoints, as expected (Fig 38D-I). CR mice also showed elevated levels of ketone bodies while fasting at both 1, 3, and 9 weeks. Analysis of relative plasma amino acid levels showed that LP and KD mice had significantly lower levels of many essential amino acids compared to control mice while fasting (Table 3), and KD mice also had significantly lower levels of essential amino acids while fed (Table 4). The levels of essential amino acids in fed LP mice were also lower, but most were not significantly lower (Table 4). Several non-essential amino acids were also significantly lower in KD and LP mice while fasting and fed (Tables 5 and 6), and the levels of many amino acids were lower in CR mice while fasting (Table 5). Together, these data show that the as assessed by plasma

152

metabolite levels, the diets produced their intended effect. Additional analysis including

metabolic pathway analysis and metabolic profiling of metabolite levels from mouse

tissues are needed to answer the question of whether these different diets affect

metabolism in similar or unique ways.
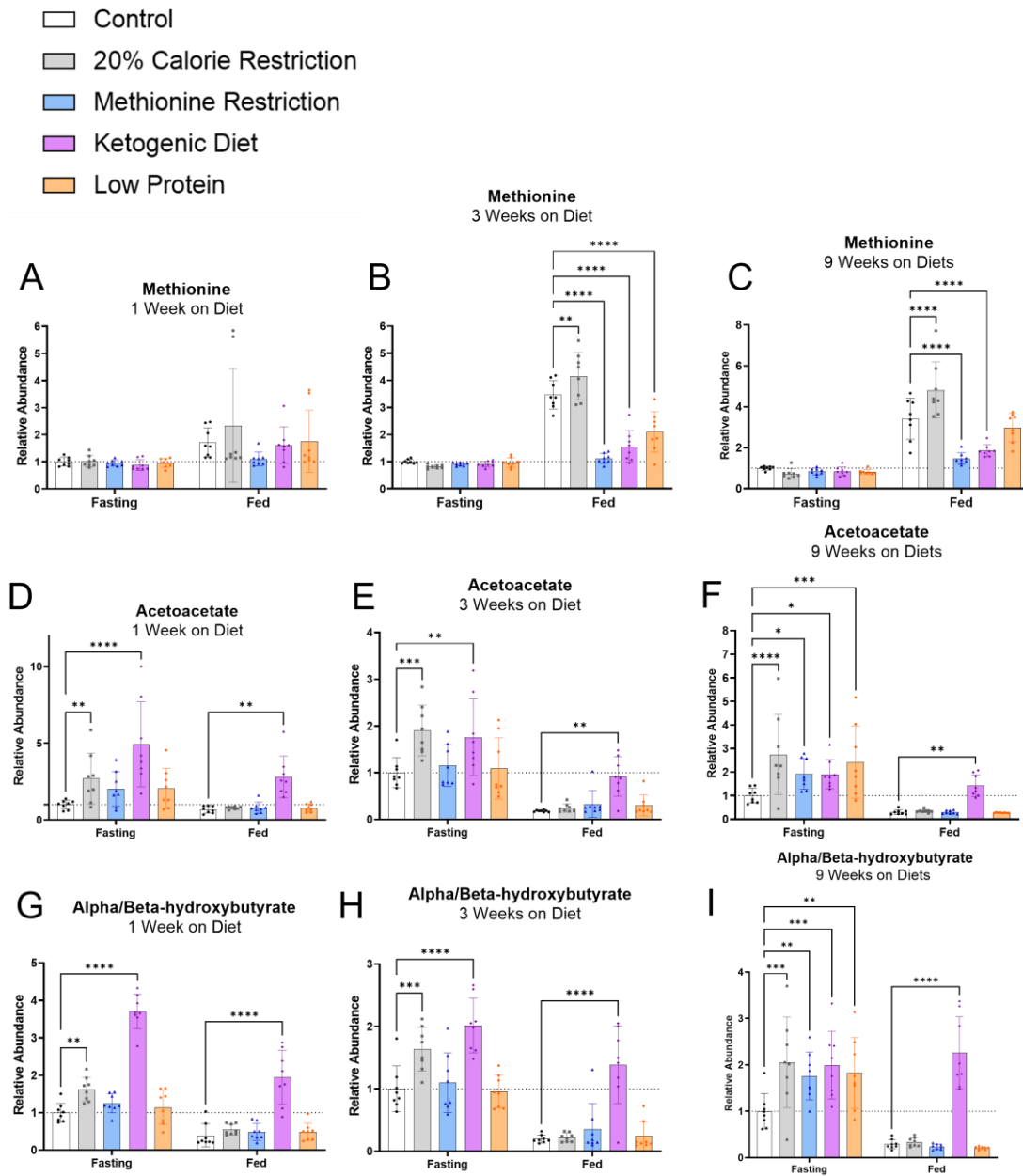
Figure 38: Dietary Effects on Blood Methionine and Ketone Body Levels

A-I) The relative plasma methionine, acetoacetate, or alpha/beta-hydroxybutyrate level while mice were either fasting or fed after 1, 3, or 9 weeks of diet initiation.

For A-I, a two-way repeated measures ANOVA was performed and followed by an uncorrected Fisher's LSD test which compared control mice to other diet groups if

interaction term was significant. *p<0.05, **p<0.01, ***p<0.001, ****p<0.0001 for Fisher's LSD test.

Table 3: Relative Fasting Essential Amino Acid Levels at 9 Weeks

p-values shown are from uncorrected Fisher's LSD test comparing control to every other diet group

9 Weeks-Fasting	CR		MR		KD		LP	
Essential Amino Acids	Fold Change	p-value	Fold Change	p-value	Fold Change	p-value	Fold Change	p-value
Histidine	**0.7284**	**0.0298**	0.8025	0.0516	**0.6796**	**0.0038**	0.8810	0.2737
Leuicine/Isoleucine	0.9076	0.0618	0.9576	0.3035	**0.8367**	**0.0142**	**0.8812**	**0.0453**
Lysine	**0.5982**	**<0.0001**	**0.7432**	**0.0049**	**0.5190**	**<0.0001**	**0.7088**	**0.0007**
Methionine	**0.7298**	**0.0141**	**0.8393**	**0.0298**	0.8421	0.0909	**0.8141**	**0.0032**
Phenylalanine	**0.8471**	**0.0030**	**0.8959**	**0.0498**	**0.7963**	**0.0043**	**0.8418**	**0.0089**
Threonine	0.9107	0.6519	0.7817	0.1310	**0.6955**	**0.0494**	**0.8027**	**0.0595**
Tryptophan	0.9882	0.8673	0.9552	0.4427	**0.7696**	**0.0014**	0.9972	0.9647
Valine	0.9657	0.4381	0.9307	0.1764	**0.7372**	**0.0006**	**0.8473**	**0.0077**
Total Increased	**0**		**0**		**0**		**0**	
Total Decreased	**4**		**3**		**7**		**6**	

Table 4: Relative Fed Essential Amino Acid Levels at 9 Weeks

p-values shown are from uncorrected Fisher's LSD test comparing control to every other diet group

9 Weeks-Fasting	CR		MR		KD		LP	
Essential Amino Acids	Fold Change	p-value	Fold Change	p-value	Fold Change	p-value	Fold Change	p-value
Histidine	**0.7284**	**0.0298**	0.8025	0.0516	**0.6796**	**0.0038**	0.8810	0.2737
Leucine/Isoleucine	0.9076	0.0618	0.9576	0.3035	**0.8367**	**0.0142**	**0.8812**	**0.0453**
Lysine	**0.5982**	**<0.0001**	**0.7432**	**0.0049**	**0.5190**	**<0.0001**	**0.7088**	**0.0007**
Methionine	**0.7298**	**0.0141**	**0.8393**	**0.0298**	0.8421	0.0909	**0.8141**	**0.0032**
Phenylalanine	**0.8471**	**0.0030**	**0.8959**	**0.0498**	**0.7963**	**0.0043**	**0.8418**	**0.0089**
Threonine	0.9107	0.6519	0.7817	0.1310	**0.6955**	**0.0494**	**0.8027**	**0.0595**
Tryptophan	0.9882	0.8673	0.9552	0.4427	**0.7696**	**0.0014**	0.9972	0.9647
Valine	0.9657	0.4381	0.9307	0.1764	**0.7372**	**0.0006**	**0.8473**	**0.0077**
Total Increased	**0**		**0**		**0**		**0**	
Total Decreased	**4**		**3**		**7**		**6**	

Table 5: Relative Fasting Non-Essential Amino Acid Levels at 9 Weeks

p-values shown are from uncorrected Fisher's LSD test comparing control to every other diet group

9 Weeks-Fasting	CR		MR		KD		LP	
Non-Essential Amino Acids	Fold Change	p-value	Fold Change	p-value	Fold Change	p-value	Fold Change	p-value
Alanine	**0.6078**	**0.0106**	0.81	0.084	**0.6585**	**0.0121**	0.8539	0.1783
Arginine	**0.7342**	**<0.0001**	0.9582	0.5005	**0.8067**	**0.0011**	**0.8633**	**0.0068**
Asparagine	**0.7071**	**0.0169**	0.927	0.433	0.9282	0.4146	0.9354	0.5598
Aspartate	1.168	0.2112	1.128	0.1967	1.172	0.1561	1.055	0.5502
Cystine	0.7229	0.0609	1.096	0.5354	1.09	0.48	0.9435	0.6745
Cysteine	0.7512	0.2202	**0.6773**	**0.0053**	**0.6342**	**0.0395**	**0.661**	**0.024**
Glutamine	0.902	0.2162	1.05	0.3259	1.032	0.6462	1.029	0.6345
Glutamate	**0.6271**	**0.0017**	1.232	0.4238	0.9358	0.7264	0.9273	0.6436
Glycine	**0.6231**	**0.0027**	**0.8992**	**0.2363**	0.8381	0.2295	0.8946	0.1768
Proline	0.9654	0.8243	0.9234	0.282	1.037	0.7485	0.9291	0.2748
Serine	**0.7989**	**0.0288**	0.9152	0.1484	0.9356	0.3059	0.9387	0.2668
Tyrosine	0.9406	0.6634	**0.8349**	**0.0391**	1.21	0.0847	**0.7822**	**0.0077**
Total Increased	**0**		**0**		**0**		**0**	
Total Decreased	**6**		**3**		**3**		**3**	

Table 6: Relative Fed Non-Essential Amino Acid Levels at 9 Weeks

p-values shown are from uncorrected Fisher's LSD test comparing control to every other diet group

9 Weeks-Fed	CR		MR		KD		LP	
Non-Essential Amino Acids	Fold Change	p-value	Fold Change	p-value	Fold Change	p-value	Fold Change	p-value
Alanine	1.297	0.0644	1.319	0.1428	**0.5534**	**0.0075**	1.112	0.5422
Arginine	0.883	0.3104	0.9797	0.7713	**0.5948**	**0.0002**	**0.7518**	**0.0075**
Asparagine	**1.357**	**0.0236**	1.348	0.0624	0.7505	0.0608	1.051	0.7849
Aspartate	0.9416	0.472	0.9832	0.8539	0.9898	0.9053	1.067	0.6052
Cystine	1.302	0.0677	**1.369**	**0.023**	0.8924	0.3911	1.009	0.9505
Cysteine	**1.873**	**0.02**	1.151	0.5066	0.9861	0.9555	1.395	0.0984
Glutamine	**1.173**	**0.0117**	**1.193**	**0.01**	**1.203**	**0.0041**	1.018	0.7883
Glutamate	0.778	0.077	1.039	0.8054	1.118	0.5185	0.9211	0.5594
Glycine	1.107	0.1687	**1.241**	**0.0066**	1.173	0.0519	1.011	0.9222
Proline	1.335	0.0851	1.226	0.2132	**0.6341**	**0.0351**	0.891	0.517
Serine	**1.394**	**0.0107**	**1.39**	**0.0043**	**0.7992**	**0.0338**	1.037	0.7276
Tyrosine	**1.6**	**0.004**	**1.375**	**0.0121**	**0.619**	**0.0099**	1.023	0.8745
Total Increased	**5**		**5**		**1**		**0**	
Total Decreased	**0**		**0**		**5**		**1**	

The goal of the ^{13}C glucose infusions was to infuse isotopically labeled glucose at a rate that did not dramatically alter blood glucose levels or cause insulin release, so that metabolism can be studied in an unperturbed state. However, the ^{13}C glucose also needed to be infused at a rate that produced sufficient labeling of glucose and its downstream metabolites to be measured using LC-MS. We found that infusing ^{13}C glucose at a rate of 10 mg/kg/min caused a steady increase in the levels of isotopically

labeled plasma glucose (Fig. 39C) while causing minimal perturbations[258] in blood

glucose and insulin levels in all but KD mice (Figs. 39A and B). We infused uniformly

labeled ^{13}C glucose (U-^{13}C glucose) at this rate for 180 minutes and then collected mouse

tissues for analysis via LC-MS. Flux data is still being analyzed, but initial analysis of

isotopomer distributions shows differences between diet groups in the labeling patterns

of several TCA intermediates collected from the heart, including citrate and alpha-

ketoglutarate (aKG). Citrate and aKG fractional labeling was decreased in CR, MR, and

LP mice as compared to control mice, and significantly increased in KD mice (Fig. 39D

and E). These results indicated that diet may affect cardiac glucose usage in the TCA

cycle.
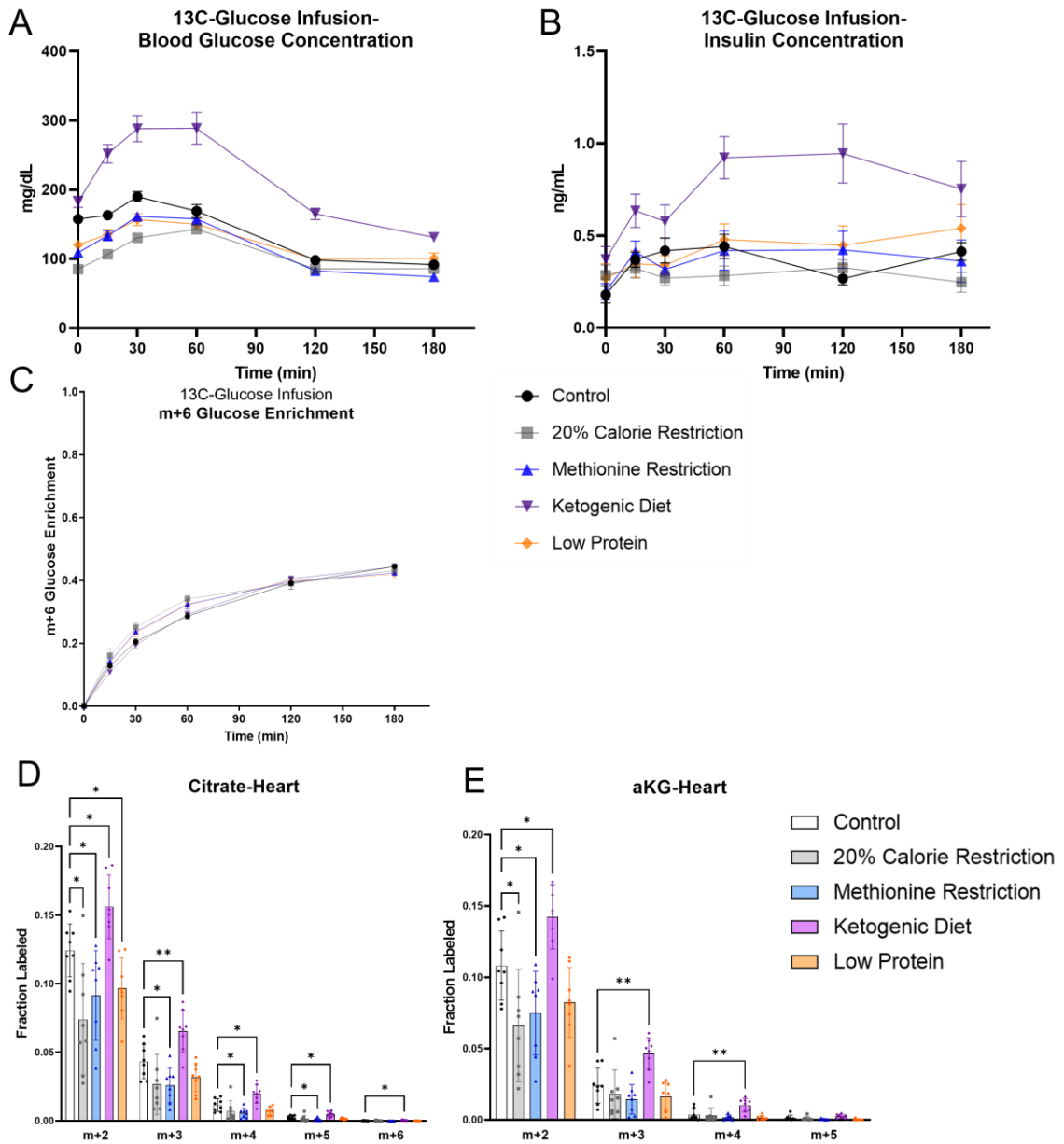
Figure 39: Initial data from ^{13}C glucose infusions

A) Blood glucose levels throughout infusions. B) Insulin levels throughout infusions. C) Ratio of m+6 glucose in plasma of mice throughout infusions. D) Fractional labeling of relevant isotopomers of cardiac citrate. E) Fractional labeling of relevant isotopomers of cardiac alpha-ketoglutarate (aKG).

For D and E, a two-way repeated measures ANOVA was performed and followed by an uncorrected Fisher's LSD test which compared control mice to other diet groups if interaction term was significant. $*p<0.05$, $**p<0.01$, $***p<0.001$, $****p<0.0001$ for Fisher's LSD test.

5.3 Discussion

This study set out to answer two separate but related questions-whether different "life-extending" diets impact metabolism in similar or unique ways, and whether diet affects tissue glucose usage. As of now, these questions are still under investigation. However, our current results show that calorie restriction, methionine restriction, and low protein diet affect the metabolic physiology of young female C57BL/6J mice in similar ways. We observed lower fasting blood glucose levels in these three groups and saw that glucose usage in cardiac TCA metabolism may be decreased. Ketogenic diet had a large impact on metabolism and physiology, causing weight gain and lowered glucose tolerance. This has been observed previously under KD [157,160], but the studies reporting a life-extending effect of KD did not observe these effects[156,161]. It is uncertain why different studies show such large differences in the physiological effects of KD, and whether these differing effects could explain the mixed results in the anti-cancer effects of KD discussed in Section 1.3.1.2.2. Plasma metabolite levels showed that methionine restriction did alter plasma methionine levels while mice were fasting, and that KD induced ketosis. Plasma amino acid levels were lower in LP and KD mice, as was expected due to the lower protein content of these diets. Pathway analysis of altered

161

metabolites is needed to assess whether these diets affect similar metabolic pathways in the tissues collected, and metabolic flux analysis will formally assess how the whole-body flux of glucose through circulation and into pathways such as the citric acid cycle is affected by diet.

5.4 Methods

5.4.1 Animal Details

All mouse work was performed by the Vanderbilt Mouse Metabolic Phenotyping Center and approved by the Vanderbilt Institutional Animal Care and Use Committee. Forty 10-week old C57BL/6J female mice were purchased from the Jackson Laboratory and single housed after 1 week of acclimation. At 12 weeks old, mice were randomized into diet groups by weight and experimental diets were started. Body weight was measured weekly.

5.4.2 Diet Details

Diets are described in Table 7 and were purchased from Research Diets. MR, LP, and KD mice were fed isocaloric amounts of food to control mice, which was the equivalent of 2.7g control mouse food/day. CR mice ate 20% fewer calories than control mice.

Table 7: Diet Composition

Product#	A19053003		A19053004		A19053005		A19053006		A19053008	
	Control		20% CR		Met Restricted		Ketogenic		Low Protein	
	gm%	kcal%	gm%	kcal%	gm%	kcal%	gm%	kcal%	gm%	kcal%
Protein	18.1	17	17.6	17	17.7	16.6	16.9	10.3	11	10.2
Carbohydrate	56.4	53	54.9	53	56.8	53.4	0.2	0.1	62.2	57.7
Fat	14.2	30	13.8	30	14.2	30	65.6	89.6	15.3	32
Total		100		100		100		100		100
kcal/gm	4.26		4.14		4.26		6.58		4.31	
Ingredient	gm	kcal	gm	kcal	gm	kcal	gm	kcal	gm	kcal
L-Alanine	4.8	19.2	4.8	19.2	4.8	19.2	2.9	11.6	2.9	11.6
L-Arginine	5.6	22.4	5.6	22.4	5.6	22.4	3.4	13.6	3.4	13.6
L-Asparagine	6.7	26.8	6.7	26.8	6.7	26.8	4	16	4	16
L-Aspartate	4.8	19.2	4.8	19.2	4.8	19.2	2.9	11.6	2.9	11.6
L-Cystine	4.1	16.4	4.1	16.4	4.1	16.4	2.2	8.8	2.2	8.8
L-Glutamine	16.2	64.8	16.2	64.8	16.2	64.8	9.8	39.2	9.8	39.2
L-Glutamate	19.7	78.8	19.7	78.8	19.7	78.8	11.9	47.6	11.9	47.6
Glycine	2.9	11.6	2.9	11.6	2.9	11.6	1.7	6.8	1.7	6.8
L-Histidine-HCl-H2O	4.3	17.2	4.3	17.2	4.3	17.2	2.6	10.4	2.6	10.4
L-Isoleucine	7.1	28.4	7.1	28.4	7.1	28.4	4.3	17.2	4.3	17.2
L-Leucine	14.9	59.6	14.9	59.6	14.9	59.6	9	36	9	36
L-Lysine-HCl	12.4	49.6	12.4	49.6	12.4	49.6	7.5	30	7.5	30
L-Methionine	4.8	19.2	4.8	19.2	1.24	4.96	2.9	11.6	2.9	11.6
L-Phenylalanine	8	32	8	32	8	32	4.8	19.2	4.8	19.2

L-Proline	16.7	*66.8*	16.7	*66.8*	16.7	*66.8*	10.1	*40.4*	10.1	*40.4*
L-Serine	9.4	*37.6*	9.4	*37.6*	9.4	*37.6*	5.7	*22.8*	5.7	*22.8*
L-Threonine	6.7	*26.8*	6.7	*26.8*	6.7	*26.8*	4.1	*16.4*	4.1	*16.4*
L-Tryptophan	2	*8*	2	*8*	2	*8*	1.2	*4.8*	1.2	*4.8*
L-Tyrosine	8.6	*34.4*	8.6	*34.4*	8.6	*34.4*	5.2	*20.8*	5.2	*20.8*
L-Valine	8.7	*34.8*	8.7	*34.8*	8.7	*34.8*	5.3	*21.2*	5.3	*21.2*
Corn Starch	295.95	*1184*	295.95	*1184*	299.5	*1198*	0	*0*	343	*1372*
Maltodextrin 10	150	*600*	150	*600*	150	*600*	0	*0*	150	*600*
Sucrose	68.8	*275*	66.3	*265*	68.8	*275*	0	*0*	68.8	*275*
Cellulose	50	*0*	62.5	*0*	50	*0*	50	*0*	50	*0*
Soybean Oil	25	*225*	25	*225*	25	*225*	25	*225*	25	*225*
Lard	107	*963*	107	*963*	107	*963*	369.5	*3326*	116	*1044*
Mineral Mix S10026	10	*0*	12.5	*0*	10	*0*	10	*0*	10	*0*
DiCalcium Phosphate	13	*0*	16.3	*0*	13	*0*	13	*0*	13	*0*
Calcium Carbonate	5.5	*0*	6.9	*0*	5.5	*0*	5.5	*0*	5.5	*0*
Potassium Citrate, 1 H2O	16.5	*0*	20.6	*0*	16.5	*0*	16.5	*0*	16.5	*0*
Sodium Bicarbonate	7.5	*0*	9.4	*0*	7.5	*0*	7.5	*0*	7.5	*0*
Vitamin Mix	10	*40*	12.5	*50*	10	*40*	0	*0*	10	*40*

V10001										
Vitamin Mix V10001C	0	*0*	0	*0*	0	*0*	1	*4*	0	*0*
Choline Bitartrate	2	*0*	2.5	*0*	2	*0*	2	*0*	2	*0*
FD&C Yellow Dye #5	0.05	*0*	0	*0*	0	*0*	0.025	*0*	0.025	*0*
FD&C Red Dye #40	0	*0*	0.05	*0*	0	*0*	0.025	*0*	0	*0*
FD&C Blue Dye #1	0	*0*	0	*0*	0.05	*0*	0	*0*	0.025	*0*
Total	**929.7**	*3961*	**955.9**	*3961*	**929.69**	*3961*	**601.55**	*3961*	**918.85**	*3962*
To feed 20% fewer calories, feed 0.82 gm for every gram of the Control Diet										

5.4.3 Plasma Metabolite Profiling

Blood was collected from mice and kept on ice until plasma was separated and flash frozen at the following timepoints throughout the study: Day 0, 7, 21, 42, 63, and 84 (days after diet initiation). At each timepoint, two plasma samples were collected: one after a four-hour fast (fasting sample), and one again the following morning after being refed overnight (fed sample). Plasma samples were analyzed by LC-MS as described below.

5.4.4 Blood Glucose Measurements

At the same timepoints blood was collected for metabolite profiling, blood glucose was measures via glucometer in both fasting and fed states.

5.4.5 Blood Pressure and Heart Rate

After 9 weeks of diet initiation, heart rate was measured and blood pressure was measured via tail cuff.

5.4.6 Exercise Stress Test

An exercise stress test was performed 10 weeks after diet initiation. Acclimated mice exercised on treadmills at 10 m/min, 0° grade, increased to 14 m/min, 3 minutes later and then increased by 4 m/min a every 3 min thereafter up to 46 m/min or until mouse was exhausted. Exhaustion was defined as the mouse sitting on the shock pad and unable to get off. Time to exhaustion, maximum run speed, total distance run, and work defined as Work = distance * body weight were measured.

5.4.7 Glucose Tolerance Test

A glucose tolerance test was performed 10 weeks after diet initiation. 2g/kg glucose was delivered via intraperitoneal injection after a 5 hr fast. 600 mg/dL was the upper detection limit of the glucometer.

5.4.8 Body Composition

Body composition was measured 11 weeks after diet initiation via quantitative magnetic resonance (QMR)[263].

5.4.9 Indirect Calorimetry

11 weeks after diet initiation, whole body VO2 and VCO2 was measured continuously in conscious mice using a Promethion system (Sable Systems Int) and used to calculate energy expenditure and respiratory quotient. Activity was measured using beam breaks and converted to pedestrian locomotion. All mice remained in the Promethion cages for 4 days.

5.4.10 ^{13}C Glucose Infusions

Mice had catheters surgically placed in the jugular vein 12 weeks after diet initiation and allowed to recover for 3-5 days prior to infusions. On the day of the infusion, mice were fasted for 6 hours and infused with uniformly labeled ^{13}C glucose (Cambridge Isotope Laboratories, #CLM-1396) at a rate of 10mg/kg/min) while washed donor red blood cells were continuously infused (2.5ul/min) to maintain hematocrit. Plasma samples were collected by tail throughout the infusion and used to measure plasma ^{13}C glucose enrichment and blood glucose and insulin levels. After 180 minutes, mice were anesthetized with phenobarbital, after which tissues were quickly collected and flash frozen.

5.4.11 Tissue Metabolite Extraction

Tissues were dipped into liquid nitrogen, and then broken down over dry ice using a hammer. Approximately 10 mg of tissue was weighed out and homogenized in 200 μL ice cold 80% HPLC-grade methanol. Another 300 μL ice cold 80% methanol was

added, and mixture was vortexed, then centrifuged at 20,000 rcf for 10 min at 4°C. The

supernatant was transferred into two new Eppendorf tubes, with the volume adjusted

so the same amount of material was transferred to the new tubes between different

samples. These tubes were dried at room temperature using a speed vacuum, and dried

samples were stored at -80°C until analysis via LC-MS.

5.4.12 Plasma Metabolite Extraction

Plasma was thawed on ice, after which 20 μL plasma was added to a new

Eppendorf tube containing 80 μL ice cold water (HPLC grade). Then 400 μL ice cold

methanol (HPLC grade) was added to the tube (final methanol concentration: 80%, v/v),

and vortexed rigorously. After 10 minutes on ice, tubes were centrifuged at 20,000 rcf

for 10 min, 4°C. The supernatant was transferred into two tubes and dried at room

temperature using a speed vacuum. Dried samples were stored at -80°C until analysis

via LC-MS.

5.4.13 Liquid chromatography

For polar metabolite analysis, the evaporated metabolite extracts were first

dissolved in 15 μL LC-MS grade water and then15 μL methanol/acetonitrile (1:1 v/v)

(Optima LC-MS grade, Fisher; methanol, #A456; acetonitrile, #A955) was added. Finally,

samples were centrifuged at 20,000 × g at 4 °C for 10 min, and the supernatants were

transferred to LC vials prior to HPLC injection (3 μL).

An XBridge amide column (100 x 2.1-mm inner diameter, 3.5 μm; Waters) was used on a Dionex (Ultimate 3000 UHPLC) for compound separation at room temperature. Mobile phase A was water with 5 mM ammonium acetate, pH 6.9, and mobile phase B was 100% acetonitrile. The gradient is linear as follows: 0 min, 85% B; 1.5 min, 85% B; 5.5 min, 35% B; 10 min, 35% B; 10.5 min, 35% B; 10.6 min, 10% B; 12.5 min, 10% B; 13.5 min, 85% B; and 20 min, 85% B. The flow rate was 0.15 ml/min from 0 to 5.5 min, 0.17 ml/min from 6.9 to 10.5 min, 0.3 ml/min from 10.6 to 17.9 min, and 0.15 ml/min from 18 to 20 min. All solvents are LC-MS grade and were purchased from Fisher.

5.4.14 Mass spectrometry

The Q Exactive Plus mass spectrometer (Thermo Scientific) is equipped with a heated electrospray ionization probe, and the relevant parameters are listed: evaporation temperature,

120 °C; sheath gas, 30; auxiliary gas, 10; sweep gas, 3; spray voltage, 3.6 kV for positive mode and 2.5 kV for negative mode. Capillary temperature was set at 320 °C, and S lens was 55. A full scan range from 70 to 900 (m/z) was used. The resolution was set at 70,000. The maximum injection time was 200 ms. Automated gain control was targeted at 3 x 106 ions.

5.4.15 Peak extraction and data analysis

Raw data collected from LC-Q Exactive Plus MS was processed on Sieve 2.0

(Thermo Scientific). Peak alignment and detection were performed according to the

protocol described by Thermo Scientific. For a targeted metabolite analysis, the method

"peak alignment and frame extraction" was applied. An input file of theoretical m/z and

detected retention time was used for targeted metabolite analysis, and the m/z width

was set to 5 ppm. An output file including detected m/z and relative intensity in

different samples was obtained after data processing. If the lowest integrated mass

spectrometer signal (MS intensity) was less than 1,000 and the highest signal was less

than 10,000, then this metabolite was considered below the detection limit and excluded

for further data analysis. If the lowest signal was less than 1,000, but the highest signal

was more than 10,000, then a value of 1,000 was imputed for the lowest signals. For

isotope tracing experiments, the mass isotopomer distributions were calculated and

normalized by comparing the ratio of labeled to unlabeled metabolites in each sample.

6. Conclusion

In this dissertation, I describe four different projects, all with the uniting theme of impacting metabolism by restricting nutrients and nutrient-metabolizing pathways, either by pharmacologic or dietary methods, and by studying these metabolic alterations using LC-MS-based metabolomics.

In the first, a pharmacologic inhibitor of the serine synthesis pathway was used to help us understand why this pathway is so important to certain cancers even when extracellular serine is abundant. We found that flux through the serine synthesis pathway, which is an offshoot of glycolysis, helps coordinate flux into other glycolytic offshoots, namely the pentose phosphate pathway and the citric acid cycle. When the serine synthesis pathway was inhibited, less glucose flowed into these pathways, and since both of these pathways in turn feed nucleotide metabolism, we also saw that nucleotide synthesis and cell growth was slowed. Serine limitation was already known to affect nucleotide metabolism through one-carbon metabolism, but our study showed a new way serine metabolism and nucleotide metabolism are connected. From this study, we can conclude that restricting serine through diet or in the media of cells has different effects than pharmacologically targeting serine synthesis.

In the second study we evolved cancer cell resistance against the unique pharmacologic inhibitor of glycolysis, Koningic Acid (KA), which targets the enzyme GAPDH. GAPDH exerts different regulatory control over glycolysis depending on the

state of glycolysis and reduces glycolytic flux more in cells displaying high Warburg

Effect (WE) than in those with low WE. KA-resistant cells lost the WE but continued to

conduct glycolysis and remained dependent on glucose as a carbon source despite

increased dependence on fatty acid metabolism. We also saw that KA-resistant cells had

many changes in nucleotide metabolism and a slower growth rate. Relevant to the topic

of this dissertation, we again see how targeting a pathway pharmacologically affects

metabolism differently than limiting directly depleting a nutrient, in this case glucose.

KA-resistant cells were still sensitive the depletion of glucose in the media, but resistant

to the effects of an inhibitor which targets glycolysis in the state of Warburg Effect.

In the third study, I examine the global metabolic impacts of cysteine restriction

in cancer cells and in flies. Cysteine is essential for the production of the antioxidant

glutathione (GSH), the depletion of which causes oxidative damage to cells and can lead

to cell death. In fact, a non-apoptotic form of cell death called ferroptosis, which involves

iron-mediated lipid peroxidation, has been observed to occur when cysteine and GSH

are limited. The small molecule erastin leads to intracellular cysteine depletion and

ferroptosis. I found that during ferroptosis, central carbon metabolism and nucleotide

metabolism are disrupted, which in certain cases can affect cell viability and/or cell

growth. I also found that depleting cysteine in the food of flies led to similar metabolic

changes in the body and head. This study again shows how maintenance of nucleotide

metabolism in cancer cells is important for their growth, and disruption of this pathway

172

can be achieved by targeting seemingly unrelated pathways. Induction of ferroptosis by cysteine limitation could be a useful anti-cancer strategy, but as observed by the shortened lifespan of flies subjected to long-term cysteine restriction, chronic cysteine limitation could lead to adverse health effects and premature aging.

Finally, I present preliminary findings from a fourth study, which examines dietary nutrient restriction in mice. We investigated the metabolic effects of four different diets that have been shown previously to positively impact mouse health in diseases such as cancer and prolong lifespan: calorie restriction (CR), methionine restriction (MR), low-protein diet (LP), and ketogenic diet (KD). We first wanted to confirm that the physiologic response to these diets was similar to what was observed in other studies. We saw that CR, MR, and LP brought about some expected physiologic changes in mice such as decreased fasting glucose levels. However, KD was obesogenic, which was not observed in studies showing it has a positive impact on health and lifespan. KD also did not affect fasting blood glucose, although it did have a small impact on postprandial blood glucose levels. As mentioned in Section 1.3.1.2, CR and KD are two diets which have been proposed could target the Warburg Effect by lowering blood glucose levels and altering glucose metabolism. It is unclear whether either diet could affect blood glucose levels enough to alter tumor glucose availability, but our preliminary results show that tissue glucose usage in the citric acid cycle is impacted by diet, at least in the heart. However, in Section 3, I show that Warburg Effect

173

is more specifically targeted by pharmacologically inhibiting GAPDH than by glucose withdrawal, suggesting this approach is better than a dietary one.

Metabolic profiling of plasma from mice fed the different diets confirmed that the diets caused expected changes in related metabolite levels, confirming that the diets were working as intended. However, further metabolic profiling of mouse plasma and tissues to determine whether each diet affects metabolism in similar or unique ways is still underway. We also conducted ^{13}C glucose infusions in the mice to investigate how diet impacted tissue-specific glucose usage and circulatory flux. While this is still under investigation, differences in the mass isotopomer distribution of citric acid cycle intermediates from the heart show that diet could impact how the heart metabolizes glucose in this important pathway. When this study is finished, we hope to elucidate the questions of whether diet impacts tissue glucose usage and whether difference life-extending diets work through similar metabolic mechanisms.

In conclusion, this dissertation illustrates how the restriction of certain nutrients and their metabolism has large impacts on global metabolism, which impacts cell health and physiology. I show that by blocking serine metabolism, glucose metabolism, and cysteine metabolism, cancer cell growth and nucleotide metabolism are inhibited. In the first two cases, pharmacologic methods of impacting nutrient metabolism lead to different effects than dietary nutrient restriction, which helps demonstrate the functions of the respective metabolic pathways and can inform likely effects of using each method

to clinically affect cancer growth. I also investigated the effects of long-term nutrient restriction in flies and mice. I found that chronic limitation of cysteine shortened fly lifespan, and that carbohydrate-free ketogenic diet led to adverse health effects in mice, whereas calorie restriction, methionine restriction, and low-protein diet improved fasting glucose levels, which has been linked to better health. In summary, modulation of metabolism by restricting nutrients and their metabolism is a powerful tool that can be used to understand and impact health and disease.

References

1   Warburg, O. The Metabolism of Carcinoma Cells. **9**, 148-163, doi:10.1158/jcr.1925.148 %J The Journal of Cancer Research (1925).

2   Warburg, O. On respiratory impairment in cancer cells. *Science* **124**, 269-270 (1956).

3   Crabtree, H. G. Observations on the carbohydrate metabolism of tumours. *Biochemical Journal* **23**, 536-545, doi:10.1042/bj0230536 %J Biochemical Journal (1929).

4   Liberti, M. V. & Locasale, J. W. The Warburg Effect: How Does it Benefit Cancer Cells? *Trends Biochem Sci* **41**, 211-218, doi:10.1016/j.tibs.2015.12.001 (2016).

5   Pavlova, N. N. & Thompson, C. B. The Emerging Hallmarks of Cancer Metabolism. *Cell Metab* **23**, 27-47, doi:10.1016/j.cmet.2015.12.006 (2016).

6   Szablewski, L. Expression of glucose transporters in cancers. *Biochim Biophys Acta* **1835**, 164-169, doi:10.1016/j.bbcan.2012.12.004 (2013).

7   Barbosa, A. M. & Martel, F. Targeting Glucose Transporters for Breast Cancer Therapy: The Effect of Natural and Synthetic Compounds. *Cancers (Basel)* **12**, doi:10.3390/cancers12010154 (2020).

8   Barron, C. C., Bilan, P. J., Tsakiridis, T. & Tsiani, E. Facilitative glucose transporters: Implications for cancer detection, prognosis and treatment. *Metabolism* **65**, 124-139, doi:10.1016/j.metabol.2015.10.007 (2016).

9   Hay, N. Reprogramming glucose metabolism in cancer: can it be exploited for cancer therapy? *Nat Rev Cancer* **16**, 635-649, doi:10.1038/nrc.2016.77 (2016).

10   Dayton, T. L., Jacks, T. & Vander Heiden, M. G. PKM2, cancer metabolism, and the road ahead. *EMBO Rep* **17**, 1721-1730, doi:10.15252/embr.201643300 (2016).

11   Allen, A. E. & Locasale, J. W. Glucose Metabolism in Cancer: The Saga of Pyruvate Kinase Continues. *Cancer Cell* **33**, 337-339, doi:10.1016/j.ccell.2018.02.008 (2018).

12   Christofk, H. R. *et al.* The M2 splice isoform of pyruvate kinase is important for cancer metabolism and tumour growth. *Nature* **452**, 230-233, doi:10.1038/nature06734 (2008).

13   Israelsen, W. J. *et al.* PKM2 isoform-specific deletion reveals a differential requirement for pyruvate kinase in tumor cells. *Cell* **155**, 397-409, doi:10.1016/j.cell.2013.09.025 (2013).

14   Lunt, S. Y. *et al.* Pyruvate kinase isoform expression alters nucleotide synthesis to impact cell proliferation. *Mol Cell* **57**, 95-107, doi:10.1016/j.molcel.2014.10.027 (2015).

15   Morita, M. *et al.* PKM1 Confers Metabolic Advantages and Promotes Cell-Autonomous Tumor Cell Growth. *Cancer Cell* **33**, 355-367 e357, doi:10.1016/j.ccell.2018.02.004 (2018).

16   Shestov, A. A. *et al.* Quantitative determinants of aerobic glycolysis identify flux through the enzyme GAPDH as a limiting step. *Elife* **3**, doi:10.7554/eLife.03342 (2014).

17   Liberti, M. V. *et al.* A Predictive Model for Selective Targeting of the Warburg Effect through GAPDH Inhibition with a Natural Product. *Cell Metab* **26**, 648-659 e648, doi:10.1016/j.cmet.2017.08.017 (2017).

18   Bose, S., Allen, A. E. & Locasale, J. W. The Molecular Link from Diet to Cancer Cell Metabolism. *Mol Cell* **80**, 554, doi:10.1016/j.molcel.2020.10.006 (2020).

19   Fontana, L., Partridge, L. & Longo, V. D. Extending healthy life span--from yeast to humans. *Science* **328**, 321-326, doi:10.1126/science.1172539 (2010).

20   Mattison, J. A. *et al.* Caloric restriction improves health and survival of rhesus monkeys. *Nat Commun* **8**, 14063, doi:10.1038/ncomms14063 (2017).

21   Lv, M., Zhu, X., Wang, H., Wang, F. & Guan, W. Roles of caloric restriction, ketogenic diet and intermittent fasting during initiation, progression and metastasis of cancer in animal models: a systematic review and meta-analysis. *PLoS One* **9**, e115147, doi:10.1371/journal.pone.0115147 (2014).

22   Castejon, M. *et al.* Energy Restriction and Colorectal Cancer: A Call for Additional Research. *Nutrients* **12**, doi:10.3390/nu12010114 (2020).

23   Tran, Q. *et al.* Revisiting the Warburg Effect: Diet-Based Strategies for Cancer Prevention. *Biomed Res Int* **2020**, 8105735, doi:10.1155/2020/8105735 (2020).

24   O'Flanagan, C. H., Smith, L. A., McDonell, S. B. & Hursting, S. D. When less may be more: calorie restriction and response to cancer therapy. *BMC Med* **15**, 106, doi:10.1186/s12916-017-0873-x (2017).

25   Redman, L. M. *et al.* Metabolic Slowing and Reduced Oxidative Damage with Sustained Caloric Restriction Support the Rate of Living and Oxidative Damage Theories of Aging. *Cell Metab* **27**, 805-815 e804, doi:10.1016/j.cmet.2018.02.019 (2018).

26   Bruss, M. D., Khambatta, C. F., Ruby, M. A., Aggarwal, I. & Hellerstein, M. K. Calorie restriction increases fatty acid synthesis and whole body fat oxidation rates. *Am J Physiol Endocrinol Metab* **298**, E108-116, doi:10.1152/ajpendo.00524.2009 (2010).

27   Green, C. L. *et al.* The effects of graded levels of calorie restriction: IX. Global metabolomic screen reveals modulation of carnitines, sphingolipids and bile acids in the liver of C57BL/6 mice. *Aging Cell* **16**, 529-540, doi:10.1111/acel.12570 (2017).

28   Huffman, J. & Kossoff, E. H. State of the ketogenic diet(s) in epilepsy. *Curr Neurol Neurosci Rep* **6**, 332-340, doi:10.1007/s11910-006-0027-6 (2006).

29   Puchalska, P. & Crawford, P. A. Multi-dimensional Roles of Ketone Bodies in Fuel Metabolism, Signaling, and Therapeutics. *Cell Metab* **25**, 262-284, doi:10.1016/j.cmet.2016.12.022 (2017).

30   Allen, B. G. *et al.* Ketogenic diets as an adjuvant cancer therapy: History and potential mechanism. *Redox Biol* **2**, 963-970, doi:10.1016/j.redox.2014.08.002 (2014).

31   Goncalves, M. D. *et al.* High-fructose corn syrup enhances intestinal tumor growth in mice. *Science* **363**, 1345-1349, doi:10.1126/science.aat8515 (2019).

32   Tisdale, M. J. & Brennan, R. A. Loss of acetoacetate coenzyme A transferase activity in tumours of peripheral tissues. *Br J Cancer* **47**, 293-297, doi:10.1038/bjc.1983.38 (1983).

33   Chang, H. T., Olson, L. K. & Schwartz, K. A. Ketolytic and glycolytic enzymatic expression profiles in malignant gliomas: implication for ketogenic diet therapy. *Nutr Metab (Lond)* **10**, 47, doi:10.1186/1743-7075-10-47 (2013).

34   Xia, S. *et al.* Prevention of Dietary-Fat-Fueled Ketogenesis Attenuates BRAF V600E Tumor Growth. *Cell Metab* **25**, 358-373, doi:10.1016/j.cmet.2016.12.010 (2017).

35   Caso, J. *et al.* The effect of carbohydrate restriction on prostate cancer tumor growth in a castrate mouse xenograft model. *Prostate* **73**, 449-454, doi:10.1002/pros.22586 (2013).

36   Klement, R. J., Champ, C. E., Otto, C. & Kammerer, U. Anti-Tumor Effects of Ketogenic Diets in Mice: A Meta-Analysis. *PLoS One* **11**, e0155050, doi:10.1371/journal.pone.0155050 (2016).

37   Allen, B. G. *et al.* Ketogenic diets enhance oxidative stress and radio-chemo-therapy responses in lung cancer xenografts. *Clin Cancer Res* **19**, 3905-3913, doi:10.1158/1078-0432.CCR-12-0287 (2013).

38   Maurer, G. D. *et al.* Differential utilization of ketone bodies by neurons and glioma cell lines: a rationale for ketogenic diet as experimental glioma therapy. *BMC Cancer* **11**, 315, doi:10.1186/1471-2407-11-315 (2011).

39   Levine, M. E. *et al.* Low protein intake is associated with a major reduction in IGF-1, cancer, and overall mortality in the 65 and younger but not older population. *Cell Metab* **19**, 407-417, doi:10.1016/j.cmet.2014.02.006 (2014).

40   Erickson, N., Boscheri, A., Linke, B. & Huebner, J. Systematic review: isocaloric ketogenic dietary regimes for cancer patients. *Med Oncol* **34**, 72, doi:10.1007/s12032-017-0930-5 (2017).

41   Sanderson, S. M., Gao, X., Dai, Z. & Locasale, J. W. Methionine metabolism in health and cancer: a nexus of diet and precision medicine. *Nat Rev Cancer* **19**, 625-637, doi:10.1038/s41568-019-0187-8 (2019).

42   Kaiser, P. Methionine Dependence of Cancer. *Biomolecules* **10**, doi:10.3390/biom10040568 (2020).

43   Ulanovskaya, O. A., Zuhl, A. M. & Cravatt, B. F. NNMT promotes epigenetic remodeling in cancer by creating a metabolic methylation sink. *Nat Chem Biol* **9**, 300-306, doi:10.1038/nchembio.1204 (2013).

44   Eckert, M. A. *et al.* Proteomics reveals NNMT as a master metabolic regulator of cancer-associated fibroblasts. *Nature* **569**, 723-728, doi:10.1038/s41586-019-1173-8 (2019).

45   Wang, Z. *et al.* Methionine is a metabolic dependency of tumor-initiating cells. *Nat Med* **25**, 825-837, doi:10.1038/s41591-019-0423-5 (2019).

46   Luckerath, K. *et al.* 11C-Methionine-PET: a novel and sensitive tool for monitoring of early response to treatment in multiple myeloma. *Oncotarget* **6**, 8418-8429, doi:10.18632/oncotarget.3053 (2015).

47   Glaudemans, A. W. *et al.* Value of 11C-methionine PET in imaging brain tumours and metastases. *Eur J Nucl Med Mol Imaging* **40**, 615-635, doi:10.1007/s00259-012-2295-5 (2013).

48   Sugimura, T., Birnbaum, S. M., Winitz, M. & Greenstein, J. P. Quantitative nutritional studies with water-soluble, chemically defined diets. VII. Nitrogen balance in normal and tumor-bearing rats following forced feeding. *Arch Biochem Biophys* **81**, 439-447, doi:10.1016/0003-9861(59)90224-3 (1959).

49   Guo, H. *et al.* Therapeutic tumor-specific cell cycle block induced by methionine starvation in vivo. *Cancer Res* **53**, 5676-5679 (1993).

50   Poirson-Bichat, F. *et al.* Methionine deprivation and methionine analogs inhibit cell proliferation and growth of human xenografted gliomas. *Life Sci* **60**, 919-931, doi:10.1016/s0024-3205(96)00672-8 (1997).

51   Poirson-Bichat, F., Goncalves, R. A., Miccoli, L., Dutrillaux, B. & Poupon, M. F. Methionine depletion enhances the antitumoral efficacy of cytotoxic agents in drug-resistant human tumor xenografts. *Clin Cancer Res* **6**, 643-653 (2000).

52   Goseki, N. *et al.* Antitumor effect of methionine-depleting total parenteral nutrition with doxorubicin administration on Yoshida sarcoma-bearing rats. *Cancer* **69**, 1865-1872, doi:10.1002/1097-0142(19920401)69:7<1865::aid-cncr2820690732>3.0.co;2-m (1992).

53   Gao, X. *et al.* Dietary methionine influences therapy in mouse cancer models and alters human metabolism. *Nature* **572**, 397-401, doi:10.1038/s41586-019-1437-3 (2019).

54   Jeon, H. *et al.* Methionine deprivation suppresses triple-negative breast cancer metastasis in vitro and in vivo. *Oncotarget* **7**, 67223-67234, doi:10.18632/oncotarget.11615 (2016).

55   Poirson-Bichat, F., Gonfalone, G., Bras-Goncalves, R. A., Dutrillaux, B. & Poupon, M. F. Growth of methionine-dependent human prostate cancer (PC-3) is

inhibited by ethionine combined with methionine starvation. *Br J Cancer* **75**, 1605-1612, doi:10.1038/bjc.1997.274 (1997).

56   Kreis, W. & Hession, C. Isolation and purification of L-methionine-alpha-deamino-gamma-mercaptomethane-lyase (L-methioninase) from Clostridium sporogenes. *Cancer Res* **33**, 1862-1865 (1973).

57   Kawaguchi, K. *et al.* Recombinant methioninase (rMETase) is an effective therapeutic for BRAF-V600E-negative as well as -positive melanoma in patient-derived orthotopic xenograft (PDOX) mouse models. *Oncotarget* **9**, 915-923, doi:10.18632/oncotarget.23185 (2018).

58   Murakami, T. *et al.* Recombinant methioninase effectively targets a Ewing's sarcoma in a patient-derived orthotopic xenograft (PDOX) nude-mouse model. *Oncotarget* **8**, 35630-35638, doi:10.18632/oncotarget.15823 (2017).

59   Igarashi, K. *et al.* Effective Metabolic Targeting of Human Osteosarcoma Cells In Vitro and in Orthotopic Nude-mouse Models with Recombinant Methioninase. *Anticancer Res* **37**, 4807-4812, doi:10.21873/anticanres.11887 (2017).

60   Tan, Y., Zavala, J., Sr., Xu, M., Zavala, J., Jr. & Hoffman, R. M. Serum methionine depletion without side effects by methioninase in metastatic breast cancer patients. *Anticancer Res* **16**, 3937-3942 (1996).

61   Tan, Y. *et al.* Recombinant methioninase infusion reduces the biochemical endpoint of serum methionine with minimal toxicity in high-stage cancer patients. *Anticancer Res* **17**, 3857-3860 (1997).

62   Hoffman, R. M. *et al.* Pilot Phase I Clinical Trial of Methioninase on High-Stage Cancer Patients: Rapid Depletion of Circulating Methionine. *Methods Mol Biol* **1866**, 231-242, doi:10.1007/978-1-4939-8796-2_17 (2019).

63   Bai, J. *et al.* Identification of a natural inhibitor of methionine adenosyltransferase 2A regulating one-carbon metabolism in keratinocytes. *EBioMedicine* **39**, 575-590, doi:10.1016/j.ebiom.2018.12.036 (2019).

64   Quinlan, C. L. *et al.* Targeting S-adenosylmethionine biosynthesis with a novel allosteric inhibitor of Mat2A. *Nat Chem Biol* **13**, 785-792, doi:10.1038/nchembio.2384 (2017).

65   Konteatis, Z. *et al.* Discovery of AG-270, a First-in-Class Oral MAT2A Inhibitor for the Treatment of Tumors with Homozygous MTAP Deletion. *J Med Chem* **64**, 4430-4449, doi:10.1021/acs.jmedchem.0c01895 (2021).

66   Heist, R. S. *et al.* Abstract PR03: A phase 1 trial of AG-270 in patients with advanced solid tumors or lymphoma with homozygous MTAP deletion. **18**, PR03-PR03, doi:10.1158/1535-7163.TARG-19-PR03 %J Molecular Cancer Therapeutics (2019).

67   Zhu, J. *et al.* Transsulfuration Activity Can Support Cell Growth upon Extracellular Cysteine Limitation. *Cell Metab* **30**, 865-876 e865, doi:10.1016/j.cmet.2019.09.009 (2019).

68   Weber, R. & Birsoy, K. The Transsulfuration Pathway Makes, the Tumor Takes. *Cell Metab* **30**, 845-846, doi:10.1016/j.cmet.2019.10.009 (2019).

69   Takeuchi, S. *et al.* Increased xCT expression correlates with tumor invasion and outcome in patients with glioblastomas. *Neurosurgery* **72**, 33-41; discussion 41, doi:10.1227/NEU.0b013e318276b2de (2013).

70   Toyoda, M. *et al.* Prognostic significance of amino-acid transporter expression (LAT1, ASCT2, and xCT) in surgically resected tongue cancer. *Br J Cancer* **110**, 2506-2513, doi:10.1038/bjc.2014.178 (2014).

71   Ji, X. *et al.* xCT (SLC7A11)-mediated metabolic reprogramming promotes non-small cell lung cancer progression. *Oncogene* **37**, 5007-5019, doi:10.1038/s41388-018-0307-z (2018).

72   Polewski, M. D. *et al.* Increased Expression of System xc- in Glioblastoma Confers an Altered Metabolic State and Temozolomide Resistance. *Mol Cancer Res* **14**, 1229-1242, doi:10.1158/1541-7786.MCR-16-0028 (2016).

73   Conrad, M. & Sato, H. The oxidative stress-inducible cystine/glutamate antiporter, system x (c) (-) : cystine supplier and beyond. *Amino Acids* **42**, 231-246, doi:10.1007/s00726-011-0867-5 (2012).

74   Griffith, O. W. Biologic and pharmacologic regulation of mammalian glutathione synthesis. *Free Radic Biol Med* **27**, 922-935 (1999).

75   Dixon, S. J. *et al.* Ferroptosis: an iron-dependent form of nonapoptotic cell death. *Cell* **149**, 1060-1072, doi:10.1016/j.cell.2012.03.042 (2012).

76   Hassannia, B., Vandenabeele, P. & Vanden Berghe, T. Targeting Ferroptosis to Iron Out Cancer. *Cancer Cell* **35**, 830-849, doi:10.1016/j.ccell.2019.04.002 (2019).

77   Sayin, V. I. *et al.* Antioxidants accelerate lung cancer progression in mice. *Sci Transl Med* **6**, 221ra215, doi:10.1126/scitranslmed.3007653 (2014).

78   Piskounova, E. *et al.* Oxidative stress inhibits distant metastasis by human melanoma cells. *Nature* **527**, 186-191, doi:10.1038/nature15726 (2015).

79   Gout, P. W., Buckley, A. R., Simms, C. R. & Bruchovsky, N. Sulfasalazine, a potent suppressor of lymphoma growth by inhibition of the x(c)- cystine transporter: a new action for an old drug. *Leukemia* **15**, 1633-1640, doi:10.1038/sj.leu.2402238 (2001).

80   Guan, J. *et al.* The xc- cystine/glutamate antiporter as a potential therapeutic target for small-cell lung cancer: use of sulfasalazine. *Cancer Chemother Pharmacol* **64**, 463-472, doi:10.1007/s00280-008-0894-4 (2009).

81   Lo, M., Ling, V., Low, C., Wang, Y. Z. & Gout, P. W. Potential use of the anti-inflammatory drug, sulfasalazine, for targeted therapy of pancreatic cancer. *Curr Oncol* **17**, 9-16, doi:10.3747/co.v17i3.485 (2010).

82   Zhang, Y. *et al.* Imidazole Ketone Erastin Induces Ferroptosis and Slows Tumor Growth in a Mouse Lymphoma Model. *Cell Chem Biol* **26**, 623-633 e629, doi:10.1016/j.chembiol.2019.01.008 (2019).

83   Wu, X. *et al.* Regulation of GSK3beta/Nrf2 signaling pathway modulated erastin-induced ferroptosis in breast cancer. *Mol Cell Biochem* **473**, 217-228, doi:10.1007/s11010-020-03821-8 (2020).

84   Gai, C. *et al.* Acetaminophen sensitizing erastin-induced ferroptosis via modulation of Nrf2/heme oxygenase-1 signaling pathway in non-small-cell lung cancer. *J Cell Physiol* **235**, 3329-3339, doi:10.1002/jcp.29221 (2020).

85   Zhao, Y. *et al.* The Role of Erastin in Ferroptosis and Its Prospects in Cancer Therapy. *Onco Targets Ther* **13**, 5429-5441, doi:10.2147/OTT.S254995 (2020).

86   Sato, M. *et al.* The ferroptosis inducer erastin irreversibly inhibits system xc- and synergizes with cisplatin to increase cisplatin's cytotoxicity in cancer cells. *Sci Rep* **8**, 968, doi:10.1038/s41598-018-19213-4 (2018).

87   Chen, L. *et al.* Erastin sensitizes glioblastoma cells to temozolomide by restraining xCT and cystathionine-gamma-lyase function. *Oncol Rep* **33**, 1465-1474, doi:10.3892/or.2015.3712 (2015).

88   Yu, Y. *et al.* The ferroptosis inducer erastin enhances sensitivity of acute myeloid leukemia cells to chemotherapeutic agents. *Mol Cell Oncol* **2**, e1054549, doi:10.1080/23723556.2015.1054549 (2015).

89   Roh, J. L., Kim, E. H., Jang, H. J., Park, J. Y. & Shin, D. Induction of ferroptotic cell death for overcoming cisplatin resistance of head and neck cancer. *Cancer Lett* **381**, 96-103, doi:10.1016/j.canlet.2016.07.035 (2016).

90   Pan, X. *et al.* Erastin decreases radioresistance of NSCLC cells partially by inducing GPX4-mediated ferroptosis. *Oncol Lett* **17**, 3001-3008, doi:10.3892/ol.2019.9888 (2019).

91   Cramer, S. L. *et al.* Systemic depletion of L-cyst(e)ine with cyst(e)inase increases reactive oxygen species and suppresses tumor growth. *Nat Med* **23**, 120-127, doi:10.1038/nm.4232 (2017).

92   Yang, M. & Vousden, K. H. Serine and one-carbon metabolism in cancer. *Nat Rev Cancer* **16**, 650-662, doi:10.1038/nrc.2016.81 (2016).

93   Locasale, J. W. Serine, glycine and one-carbon units: cancer metabolism in full circle. *Nat Rev Cancer* **13**, 572-583, doi:10.1038/nrc3557 (2013).

94   Gonen, N. & Assaraf, Y. G. Antifolates in cancer therapy: structure, activity and mechanisms of drug resistance. *Drug Resist Updat* **15**, 183-210, doi:10.1016/j.drup.2012.07.002 (2012).

95   Longley, D. B., Harkin, D. P. & Johnston, P. G. 5-fluorouracil: mechanisms of action and clinical strategies. *Nat Rev Cancer* **3**, 330-338, doi:10.1038/nrc1074 (2003).

96   Hayashi, S., Tanaka, T., Naito, J. & Suda, M. Dietary and hormonal regulation of serine synthesis in the rat. *J Biochem* **77**, 207-219 (1975).

97   Maddocks, O. D. *et al.* Serine starvation induces stress and p53-dependent metabolic remodelling in cancer cells. *Nature* **493**, 542-546, doi:10.1038/nature11743 (2013).

98   Sullivan, M. R. *et al.* Increased Serine Synthesis Provides an Advantage for Tumors Arising in Tissues Where Serine Levels Are Limiting. *Cell Metab* **29**, 1410-1421 e1414, doi:10.1016/j.cmet.2019.02.015 (2019).

99   Gravel, S. P. *et al.* Serine deprivation enhances antineoplastic activity of biguanides. *Cancer Res* **74**, 7521-7533, doi:10.1158/0008-5472.CAN-14-2643-T (2014).

100   Maddocks, O. D. K. *et al.* Modulating the therapeutic response of tumours to dietary serine and glycine starvation. *Nature* **544**, 372-376, doi:10.1038/nature22056 (2017).

101   Tajan, M. *et al.* Serine synthesis pathway inhibition cooperates with dietary serine and glycine limitation for cancer therapy. *Nat Commun* **12**, 366, doi:10.1038/s41467-020-20223-y (2021).

102   Snell, K., Natsumeda, Y., Eble, J. N., Glover, J. L. & Weber, G. Enzymic imbalance in serine metabolism in human colon carcinoma and rat sarcoma. *Br J Cancer* **57**, 87-90, doi:10.1038/bjc.1988.15 (1988).

103   Locasale, J. W. *et al.* Phosphoglycerate dehydrogenase diverts glycolytic flux and contributes to oncogenesis. *Nat Genet* **43**, 869-874, doi:10.1038/ng.890 (2011).

104   Mullarky, E., Mattaini, K. R., Vander Heiden, M. G., Cantley, L. C. & Locasale, J. W. PHGDH amplification and altered glucose metabolism in human melanoma. *Pigment Cell Melanoma Res* **24**, 1112-1115, doi:10.1111/j.1755-148X.2011.00919.x (2011).

105   Possemato, R. *et al.* Functional genomics reveal that the serine synthesis pathway is essential in breast cancer. *Nature* **476**, 346-350, doi:10.1038/nature10350 (2011).

106   Antonov, A. *et al.* Bioinformatics analysis of the serine and glycine pathway in cancer cells. *Oncotarget* **5**, 11004-11013, doi:10.18632/oncotarget.2668 (2014).

107   Mullarky, E. *et al.* Identification of a small molecule inhibitor of 3-phosphoglycerate dehydrogenase to target serine biosynthesis in cancers. *Proc Natl Acad Sci U S A* **113**, 1778-1783, doi:10.1073/pnas.1521548113 (2016).

108   Pacold, M. E. *et al.* A PHGDH inhibitor reveals coordination of serine synthesis and one-carbon unit fate. *Nat Chem Biol* **12**, 452-458, doi:10.1038/nchembio.2070 (2016).

109   Wang, Q. *et al.* Rational Design of Selective Allosteric Inhibitors of PHGDH and Serine Synthesis with Anti-tumor Activity. *Cell Chem Biol* **24**, 55-65, doi:10.1016/j.chembiol.2016.11.013 (2017).

110   DeNicola, G. M. *et al.* NRF2 regulates serine biosynthesis in non-small cell lung cancer. *Nat Genet* **47**, 1475-1481, doi:10.1038/ng.3421 (2015).

111   McCay, C. M., Crowell, M. F. & Maynard, L. A. The effect of retarded growth upon the length of life span and upon the ultimate body size. 1935. *Nutrition* **5**, 155-171; discussion 172 (1989).

112   McDonald, R. B. & Ramsey, J. J. Honoring Clive McCay and 75 years of calorie restriction research. *J Nutr* **140**, 1205-1210, doi:10.3945/jn.110.122804 (2010).

113   Kaeberlein, M., Kirkland, K. T., Fields, S. & Kennedy, B. K. Sir2-independent life span extension by calorie restriction in yeast. *PLoS Biol* **2**, E296, doi:10.1371/journal.pbio.0020296 (2004).

114   Partridge, L., Piper, M. D. & Mair, W. Dietary restriction in Drosophila. *Mech Ageing Dev* **126**, 938-950, doi:10.1016/j.mad.2005.03.023 (2005).

115   Omodei, D. & Fontana, L. Calorie restriction and prevention of age-associated chronic disease. *FEBS Lett* **585**, 1537-1542, doi:10.1016/j.febslet.2011.03.015 (2011).

116   Colman, R. J., Beasley, T. M., Allison, D. B. & Weindruch, R. Attenuation of sarcopenia by dietary restriction in rhesus monkeys. *J Gerontol A Biol Sci Med Sci* **63**, 556-559, doi:10.1093/gerona/63.6.556 (2008).

117   Colman, R. J. *et al.* Caloric restriction delays disease onset and mortality in rhesus monkeys. *Science* **325**, 201-204, doi:10.1126/science.1173635 (2009).

118   Mattison, J. A. *et al.* Impact of caloric restriction on health and survival in rhesus monkeys from the NIA study. *Nature* **489**, 318-321, doi:10.1038/nature11432 (2012).

119   Cava, E. & Fontana, L. Will calorie restriction work in humans? *Aging (Albany NY)* **5**, 507-514, doi:10.18632/aging.100581 (2013).

120   Bodkin, N. L., Alexander, T. M., Ortmeyer, H. K., Johnson, E. & Hansen, B. C. Mortality and morbidity in laboratory-maintained Rhesus monkeys and effects of long-term dietary restriction. *J Gerontol A Biol Sci Med Sci* **58**, 212-219, doi:10.1093/gerona/58.3.b212 (2003).

121   Most, J., Tosti, V., Redman, L. M. & Fontana, L. Calorie restriction in humans: An update. *Ageing Res Rev* **39**, 36-45, doi:10.1016/j.arr.2016.08.005 (2017).

122   Most, J. & Redman, L. M. Impact of calorie restriction on energy metabolism in humans. *Exp Gerontol* **133**, 110875, doi:10.1016/j.exger.2020.110875 (2020).

123   Hwangbo, D. S., Lee, H. Y., Abozaid, L. S. & Min, K. J. Mechanisms of Lifespan Regulation by Calorie Restriction and Intermittent Fasting in Model Organisms. *Nutrients* **12**, doi:10.3390/nu12041194 (2020).

124   Redman, L. M. & Ravussin, E. Endocrine alterations in response to calorie restriction in humans. *Mol Cell Endocrinol* **299**, 129-136, doi:10.1016/j.mce.2008.10.014 (2009).

125   Mercken, E. M. *et al.* Calorie restriction in humans inhibits the PI3K/AKT pathway and induces a younger transcription profile. *Aging Cell* **12**, 645-651, doi:10.1111/acel.12088 (2013).

126   Soare, A., Cangemi, R., Omodei, D., Holloszy, J. O. & Fontana, L. Long-term calorie restriction, but not endurance exercise, lowers core body temperature in humans. *Aging (Albany NY)* **3**, 374-379, doi:10.18632/aging.100280 (2011).

127   Zheng, X., Wang, S. & Jia, W. Calorie restriction and its impact on gut microbial composition and global metabolism. *Front Med* **12**, 634-644, doi:10.1007/s11684-018-0670-8 (2018).

128   Ruetenik, A. & Barrientos, A. Dietary restriction, mitochondrial function and aging: from yeast to humans. *Biochim Biophys Acta* **1847**, 1434-1447, doi:10.1016/j.bbabio.2015.05.005 (2015).

129   Mair, W., Piper, M. D. & Partridge, L. Calories do not explain extension of life span by dietary restriction in Drosophila. *PLoS Biol* **3**, e223, doi:10.1371/journal.pbio.0030223 (2005).

130   Grandison, R. C., Piper, M. D. & Partridge, L. Amino-acid imbalance explains extension of lifespan by dietary restriction in Drosophila. *Nature* **462**, 1061-1064, doi:10.1038/nature08619 (2009).

131   Solon-Biet, S. M. *et al.* The ratio of macronutrients, not caloric intake, dictates cardiometabolic health, aging, and longevity in ad libitum-fed mice. *Cell Metab* **19**, 418-430, doi:10.1016/j.cmet.2014.02.009 (2014).

132   Le Couteur, D. G. *et al.* The impact of low-protein high-carbohydrate diets on aging and lifespan. *Cell Mol Life Sci* **73**, 1237-1252, doi:10.1007/s00018-015-2120-y (2016).

133   Mirzaei, H., Suarez, J. A. & Longo, V. D. Protein and amino acid restriction, aging and disease: from yeast to humans. *Trends Endocrinol Metab* **25**, 558-566, doi:10.1016/j.tem.2014.07.002 (2014).

134   Kitada, M., Ogura, Y., Monno, I. & Koya, D. The impact of dietary protein intake on longevity and metabolic health. *EBioMedicine* **43**, 632-640, doi:10.1016/j.ebiom.2019.04.005 (2019).

135   Bruce, K. D. *et al.* High carbohydrate-low protein consumption maximizes Drosophila lifespan. *Exp Gerontol* **48**, 1129-1135, doi:10.1016/j.exger.2013.02.003 (2013).

136   Wahl, D. *et al.* Comparing the Effects of Low-Protein and High-Carbohydrate Diets and Caloric Restriction on Brain Aging in Mice. *Cell Rep* **25**, 2234-2243 e2236, doi:10.1016/j.celrep.2018.10.070 (2018).

137   Song, M. *et al.* Association of Animal and Plant Protein Intake With All-Cause and Cause-Specific Mortality. *JAMA Intern Med* **176**, 1453-1463, doi:10.1001/jamainternmed.2016.4182 (2016).

138   Budhathoki, S. *et al.* Association of Animal and Plant Protein Intake With All-Cause and Cause-Specific Mortality in a Japanese Cohort. *JAMA Intern Med* **179**, 1509-1518, doi:10.1001/jamainternmed.2019.2806 (2019).

139   Fontana, L. *et al.* Decreased Consumption of Branched-Chain Amino Acids Improves Metabolic Health. *Cell Rep* **16**, 520-530, doi:10.1016/j.celrep.2016.05.092 (2016).

140   Cummings, N. E. *et al.* Restoration of metabolic health by decreased consumption of branched-chain amino acids. *J Physiol* **596**, 623-645, doi:10.1113/JP275075 (2018).

141   Lee, B. C., Kaya, A. & Gladyshev, V. N. Methionine restriction and life-span control. *Ann N Y Acad Sci* **1363**, 116-124, doi:10.1111/nyas.12973 (2016).

142   Orentreich, N., Matias, J. R., DeFelice, A. & Zimmerman, J. A. Low methionine ingestion by rats extends life span. *J Nutr* **123**, 269-274, doi:10.1093/jn/123.2.269 (1993).

143   McIsaac, R. S., Lewis, K. N., Gibney, P. A. & Buffenstein, R. From yeast to human: exploring the comparative biology of methionine restriction in extending eukaryotic life span. *Ann N Y Acad Sci* **1363**, 155-170, doi:10.1111/nyas.13032 (2016).

144   Plaisance, E. P. *et al.* Dietary methionine restriction increases fat oxidation in obese adults with metabolic syndrome. *J Clin Endocrinol Metab* **96**, E836-840, doi:10.1210/jc.2010-2493 (2011).

145   Virtanen, J. K. *et al.* High dietary methionine intake increases the risk of acute coronary events in middle-aged men. *Nutr Metab Cardiovasc Dis* **16**, 113-120, doi:10.1016/j.numecd.2005.05.005 (2006).

146   Lind, M. V. *et al.* One-carbon metabolism markers are associated with cardiometabolic risk factors. *Nutr Metab Cardiovasc Dis* **28**, 402-410, doi:10.1016/j.numecd.2018.01.005 (2018).

147   McCarty, M. F., Barroso-Aranda, J. & Contreras, F. The low-methionine content of vegan diets may make methionine restriction feasible as a life extension strategy. *Med Hypotheses* **72**, 125-128, doi:10.1016/j.mehy.2008.07.044 (2009).

148   Le, L. T. & Sabate, J. Beyond meatless, the health effects of vegan diets: findings from the Adventist cohorts. *Nutrients* **6**, 2131-2147, doi:10.3390/nu6062131 (2014).

149   Dinu, M., Abbate, R., Gensini, G. F., Casini, A. & Sofi, F. Vegetarian, vegan diets and multiple health outcomes: A systematic review with meta-analysis of observational studies. *Crit Rev Food Sci Nutr* **57**, 3640-3649, doi:10.1080/10408398.2016.1138447 (2017).

150   Allen, A. E. & Locasale, J. W. Metabolomics: insights into plant-based diets. *EMBO Mol Med* **13**, e13568, doi:10.15252/emmm.202013568 (2021).

151   Parkhitko, A. A., Jouandin, P., Mohr, S. E. & Perrimon, N. Methionine metabolism and methyltransferases in the regulation of aging and lifespan extension across species. *Aging Cell* **18**, e13034, doi:10.1111/acel.13034 (2019).

152   Eisenberg, T. *et al.* Cardioprotection and lifespan extension by the natural polyamine spermidine. *Nat Med* **22**, 1428-1438, doi:10.1038/nm.4222 (2016).

153   Newman, J. C. & Verdin, E. Ketone bodies as signaling metabolites. *Trends Endocrinol Metab* **25**, 42-52, doi:10.1016/j.tem.2013.09.002 (2014).

154   Youm, Y. H. *et al.* The ketone metabolite beta-hydroxybutyrate blocks NLRP3 inflammasome-mediated inflammatory disease. *Nat Med* **21**, 263-269, doi:10.1038/nm.3804 (2015).

155   Moreno, C. L. & Mobbs, C. V. Epigenetic mechanisms underlying lifespan and age-related effects of dietary restriction and the ketogenic diet. *Mol Cell Endocrinol* **455**, 33-40, doi:10.1016/j.mce.2016.11.013 (2017).

156   Roberts, M. N. *et al.* A Ketogenic Diet Extends Longevity and Healthspan in Adult Mice. *Cell Metab* **26**, 539-546 e535, doi:10.1016/j.cmet.2017.08.005 (2017).

157   Newman, J. C. *et al.* Ketogenic Diet Reduces Midlife Mortality and Improves Memory in Aging Mice. *Cell Metab* **26**, 547-557 e548, doi:10.1016/j.cmet.2017.08.004 (2017).

158   Douris, N. *et al.* Adaptive changes in amino acid metabolism permit normal longevity in mice consuming a low-carbohydrate ketogenic diet. *Biochim Biophys Acta* **1852**, 2056-2065, doi:10.1016/j.bbadis.2015.07.009 (2015).

159   Bielohuby, M. *et al.* Induction of ketosis in rats fed low-carbohydrate, high-fat diets depends on the relative abundance of dietary fat and protein. *Am J Physiol Endocrinol Metab* **300**, E65-76, doi:10.1152/ajpendo.00478.2010 (2011).

160   Borghjid, S. & Feinman, R. D. Response of C57Bl/6 mice to a carbohydrate-free diet. *Nutr Metab (Lond)* **9**, 69, doi:10.1186/1743-7075-9-69 (2012).

161   Kennedy, A. R. *et al.* A high-fat, ketogenic diet induces a unique metabolic state in mice. *Am J Physiol Endocrinol Metab* **292**, E1724-1739, doi:10.1152/ajpendo.00717.2006 (2007).

162   Pissios, P. *et al.* Methionine and choline regulate the metabolic phenotype of a ketogenic diet. *Mol Metab* **2**, 306-313, doi:10.1016/j.molmet.2013.07.003 (2013).

163   Bueno, N. B., de Melo, I. S., de Oliveira, S. L. & da Rocha Ataide, T. Very-low-carbohydrate ketogenic diet v. low-fat diet for long-term weight loss: a meta-analysis of randomised controlled trials. *Br J Nutr* **110**, 1178-1187, doi:10.1017/S0007114513000548 (2013).

164   Paoli, A. Ketogenic diet for obesity: friend or foe? *Int J Environ Res Public Health* **11**, 2092-2107, doi:10.3390/ijerph110202092 (2014).

165   Miller, V. J. *et al.* A ketogenic diet combined with exercise alters mitochondrial function in human skeletal muscle while improving metabolic health. *Am J Physiol Endocrinol Metab* **319**, E995-E1007, doi:10.1152/ajpendo.00305.2020 (2020).

166   Gibas, M. K. & Gibas, K. J. Induced and controlled dietary ketosis as a regulator of obesity and metabolic syndrome pathologies. *Diabetes Metab Syndr* **11 Suppl 1**, S385-S390, doi:10.1016/j.dsx.2017.03.022 (2017).

167   Simm, P. J. *et al.* The effect of the ketogenic diet on the developing skeleton. *Epilepsy Res* **136**, 62-66, doi:10.1016/j.eplepsyres.2017.07.014 (2017).

168   Rosenbaum, M. *et al.* Glucose and Lipid Homeostasis and Inflammation in Humans Following an Isocaloric Ketogenic Diet. *Obesity (Silver Spring)* **27**, 971-981, doi:10.1002/oby.22468 (2019).

169   O'Neill, B. & Raggi, P. The ketogenic diet: Pros and cons. *Atherosclerosis* **292**, 119-126, doi:10.1016/j.atherosclerosis.2019.11.021 (2020).

170   Dixon, S. J. *et al.* Pharmacological inhibition of cystine-glutamate exchange induces endoplasmic reticulum stress and ferroptosis. *Elife* **3**, e02523, doi:10.7554/eLife.02523 (2014).

171   Sato, H., Tamba, M., Ishii, T. & Bannai, S. Cloning and expression of a plasma membrane cystine/glutamate exchange transporter composed of two distinct proteins. *J Biol Chem* **274**, 11455-11458 (1999).

172   Yang, W. S. *et al.* Regulation of ferroptotic cancer cell death by GPX4. *Cell* **156**, 317-331, doi:10.1016/j.cell.2013.12.010 (2014).

173   Skouta, R. *et al.* Ferrostatins inhibit oxidative lipid damage and cell death in diverse disease models. *J Am Chem Soc* **136**, 4551-4556, doi:10.1021/ja411006a (2014).

174   Linkermann, A. *et al.* Synchronized renal tubular cell death involves ferroptosis. *Proc Natl Acad Sci U S A* **111**, 16836-16841, doi:10.1073/pnas.1415518111 (2014).

175   Friedmann Angeli, J. P. *et al.* Inactivation of the ferroptosis regulator Gpx4 triggers acute renal failure in mice. *Nat Cell Biol* **16**, 1180-1191, doi:10.1038/ncb3064 (2014).

176   Lorincz, T., Jemnitz, K., Kardon, T., Mandl, J. & Szarka, A. Ferroptosis is Involved in Acetaminophen Induced Cell Death. *Pathol Oncol Res* **21**, 1115-1121, doi:10.1007/s12253-015-9946-3 (2015).

177   Yao, M. Y. *et al.* Role of ferroptosis in neurological diseases. *Neurosci Lett* **747**, 135614, doi:10.1016/j.neulet.2020.135614 (2021).

178   Seibt, T. M., Proneth, B. & Conrad, M. Role of GPX4 in ferroptosis and its pharmacological implication. *Free Radic Biol Med* **133**, 144-152, doi:10.1016/j.freeradbiomed.2018.09.014 (2019).

179   Jiang, X., Stockwell, B. R. & Conrad, M. Ferroptosis: mechanisms, biology and role in disease. *Nat Rev Mol Cell Biol* **22**, 266-282, doi:10.1038/s41580-020-00324-8 (2021).

180   Lu, B. *et al.* The Role of Ferroptosis in Cancer Development and Treatment Response. *Front Pharmacol* **8**, 992, doi:10.3389/fphar.2017.00992 (2017).

181   Stockwell, B. R., Jiang, X. & Gu, W. Emerging Mechanisms and Disease Relevance of Ferroptosis. *Trends Cell Biol* **30**, 478-490, doi:10.1016/j.tcb.2020.02.009 (2020).

182   Hangauer, M. J. *et al.* Drug-tolerant persister cancer cells are vulnerable to GPX4 inhibition. *Nature* **551**, 247-250, doi:10.1038/nature24297 (2017).

183   Jiang, L. *et al.* Ferroptosis as a p53-mediated activity during tumour suppression. *Nature* **520**, 57-62, doi:10.1038/nature14344 (2015).

184   Lin, W. *et al.* SLC7A11/xCT in cancer: biological functions and therapeutic implications. *Am J Cancer Res* **10**, 3106-3126 (2020).

185   Gao, M. *et al.* Role of Mitochondria in Ferroptosis. *Mol Cell* **73**, 354-363 e353, doi:10.1016/j.molcel.2018.10.042 (2019).

186   Zheng, J. & Conrad, M. The Metabolic Underpinnings of Ferroptosis. *Cell Metab* **32**, 920-937, doi:10.1016/j.cmet.2020.10.011 (2020).

187   Feng, H. & Stockwell, B. R. Unsolved mysteries: How does lipid peroxidation cause ferroptosis? *PLoS Biol* **16**, e2006203, doi:10.1371/journal.pbio.2006203 (2018).

188   Sullivan, L. B. *et al.* Supporting Aspartate Biosynthesis Is an Essential Function of Respiration in Proliferating Cells. *Cell* **162**, 552-563, doi:10.1016/j.cell.2015.07.017 (2015).

189   Zhang, F., Lau, S. S. & Monks, T. J. The cytoprotective effect of N-acetyl-L-cysteine against ROS-induced cytotoxicity is independent of its ability to enhance glutathione synthesis. *Toxicol Sci* **120**, 87-97, doi:10.1093/toxsci/kfq364 (2011).

190   Antoniewicz, M. R., Kelleher, J. K. & Stephanopoulos, G. Determination of confidence intervals of metabolic fluxes estimated from stable isotope measurements. *Metab Eng* **8**, 324-337, doi:10.1016/j.ymben.2006.01.004 (2006).

191   Mehrmohamadi, M., Liu, X., Shestov, A. A. & Locasale, J. W. Characterization of the usage of the serine metabolic network in human cancer. *Cell Rep* **9**, 1507-1519, doi:10.1016/j.celrep.2014.10.026 (2014).

192   Buescher, J. M. *et al.* A roadmap for interpreting (13)C metabolite labeling patterns from cells. *Curr Opin Biotechnol* **34**, 189-201, doi:10.1016/j.copbio.2015.02.003 (2015).

193   Gopalakrishnan, S. & Maranas, C. D. 13C metabolic flux analysis at a genome-scale. *Metab Eng* **32**, 12-22, doi:10.1016/j.ymben.2015.08.006 (2015).

194   Badur, M. G. & Metallo, C. M. Reverse engineering the cancer metabolic network using flux analysis to understand drivers of human disease. *Metab Eng* **45**, 95-108, doi:10.1016/j.ymben.2017.11.013 (2018).

195   Yuan, J., Fowler, W. U., Kimball, E., Lu, W. & Rabinowitz, J. D. Kinetic flux profiling of nitrogen assimilation in Escherichia coli. *Nat Chem Biol* **2**, 529-530, doi:10.1038/nchembio816 (2006).

196   Yuan, J., Bennett, B. D. & Rabinowitz, J. D. Kinetic flux profiling for quantitation of cellular metabolic fluxes. *Nat Protoc* **3**, 1328-1340, doi:10.1038/nprot.2008.131 (2008).

197   Munger, J. *et al.* Systems-level metabolic flux profiling identifies fatty acid synthesis as a target for antiviral therapy. *Nat Biotechnol* **26**, 1179-1186, doi:10.1038/nbt.1500 (2008).

198   Szecowka, M. *et al.* Metabolic fluxes in an illuminated Arabidopsis rosette. *Plant Cell* **25**, 694-714, doi:10.1105/tpc.112.106989 (2013).

199   Huang, L., Kim, D., Liu, X., Myers, C. R. & Locasale, J. W. Estimating relative changes of metabolic fluxes. *PLoS Comput Biol* **10**, e1003958, doi:10.1371/journal.pcbi.1003958 (2014).

200   Juvekar, A. *et al.* Phosphoinositide 3-kinase inhibitors induce DNA damage through nucleoside depletion. *Proc Natl Acad Sci U S A* **113**, E4338-4347, doi:10.1073/pnas.1522223113 (2016).

201   Bester, A. C. *et al.* Nucleotide deficiency promotes genomic instability in early stages of cancer development. *Cell* **145**, 435-446, doi:10.1016/j.cell.2011.03.044 (2011).

202   Hitosugi, T. *et al.* Phosphoglycerate mutase 1 coordinates glycolysis and biosynthesis to promote tumor growth. *Cancer Cell* **22**, 585-600, doi:10.1016/j.ccr.2012.09.020 (2012).

203   Vander Heiden, M. G. *et al.* Evidence for an alternative glycolytic pathway in rapidly proliferating cells. *Science* **329**, 1492-1499, doi:10.1126/science.1188015 (2010).

204   Vander Heiden, M. G. *et al.* Metabolic pathway alterations that support cell proliferation. *Cold Spring Harb Symp Quant Biol* **76**, 325-334, doi:10.1101/sqb.2012.76.010900 (2011).

205   Oslund, R. C. *et al.* Bisphosphoglycerate mutase controls serine pathway flux via 3-phosphoglycerate. *Nat Chem Biol* **13**, 1081-1087, doi:10.1038/nchembio.2453 (2017).

206   Liu, X., Ser, Z. & Locasale, J. W. Development and quantitative evaluation of a high-resolution metabolomics technology. *Anal Chem* **86**, 2175-2184, doi:10.1021/ac403845u (2014).

207   Shlomi, T., Benyamini, T., Gottlieb, E., Sharan, R. & Ruppin, E. Genome-scale metabolic modeling elucidates the role of proliferative adaptation in causing the Warburg effect. *PLoS Comput Biol* **7**, e1002018, doi:10.1371/journal.pcbi.1002018 (2011).

208   Antoniewicz, M. R., Kelleher, J. K. & Stephanopoulos, G. Elementary metabolite units (EMU): a novel framework for modeling isotopic distributions. *Metab Eng* **9**, 68-86, doi:10.1016/j.ymben.2006.09.001 (2007).

209   Endo, A., Hasumi, K., Sakai, K. & Kanbe, T. Specific inhibition of glyceraldehyde-3-phosphate dehydrogenase by koningic acid (heptelidic acid). *J Antibiot (Tokyo)* **38**, 920-925, doi:10.7164/antibiotics.38.920 (1985).

210   Liu, J., Wang, J. & Guo, Z.   (Google Patents, 2017).

211   Holohan, C., Van Schaeybroeck, S., Longley, D. B. & Johnston, P. G. Cancer drug resistance: an evolving paradigm. *Nat Rev Cancer* **13**, 714-726, doi:10.1038/nrc3599 (2013).

212   Sakai, K., Hasumi, K. & Endo, A. Inactivation of rabbit muscle glyceraldehyde-3-phosphate dehydrogenase by koningic acid. *Biochim Biophys Acta* **952**, 297-303, doi:10.1016/0167-4838(88)90130-6 (1988).

213   van Heerden, J. H. *et al.* Lost in transition: start-up of glycolysis yields subpopulations of nongrowing cells. *Science* **343**, 1245114, doi:10.1126/science.1245114 (2014).

214   Vander Heiden, M. G., Cantley, L. C. & Thompson, C. B. Understanding the Warburg effect: the metabolic requirements of cell proliferation. *Science* **324**, 1029-1033, doi:10.1126/science.1160809 (2009).

215   Pusapati, R. V. *et al.* mTORC1-Dependent Metabolic Reprogramming Underlies Escape from Glycolysis Addiction in Cancer Cells. *Cancer Cell* **29**, 548-562, doi:10.1016/j.ccell.2016.02.018 (2016).

216   Boudreau, A. *et al.* Metabolic plasticity underpins innate and acquired resistance to LDHA inhibition. *Nat Chem Biol* **12**, 779-786, doi:10.1038/nchembio.2143 (2016).

217   Hu, Z., Cha, S. H., Chohnan, S. & Lane, M. D. Hypothalamic malonyl-CoA as a mediator of feeding behavior. *Proc Natl Acad Sci U S A* **100**, 12624-12629, doi:10.1073/pnas.1834402100 (2003).

218   Loftus, T. M. *et al.* Reduced food intake and body weight in mice treated with fatty acid synthase inhibitors. *Science* **288**, 2379-2381, doi:10.1126/science.288.5475.2379 (2000).

219   Thupari, J. N., Pinn, M. L. & Kuhajda, F. P. Fatty acid synthase inhibition in human breast cancer cells leads to malonyl-CoA-induced inhibition of fatty acid oxidation and cytotoxicity. *Biochem Biophys Res Commun* **285**, 217-223, doi:10.1006/bbrc.2001.5146 (2001).

195

220   Gao, X. *et al.* Serine Availability Influences Mitochondrial Dynamics and Function through Lipid Metabolism. *Cell Rep* **22**, 3507-3520, doi:10.1016/j.celrep.2018.03.017 (2018).

221   Koves, T. R. *et al.* Mitochondrial overload and incomplete fatty acid oxidation contribute to skeletal muscle insulin resistance. *Cell Metab* **7**, 45-56, doi:10.1016/j.cmet.2007.10.013 (2008).

222   Owen, M. R., Doran, E. & Halestrap, A. P. Evidence that metformin exerts its anti-diabetic effects through inhibition of complex 1 of the mitochondrial respiratory chain. *Biochem J* **348 Pt 3**, 607-614 (2000).

223   Kornberg, M. D. *et al.* Dimethyl fumarate targets GAPDH and aerobic glycolysis to modulate immunity. *Science* **360**, 449-453, doi:10.1126/science.aan4665 (2018).

224   Yun, J. *et al.* Vitamin C selectively kills KRAS and BRAF mutant colorectal cancer cells by targeting GAPDH. *Science* **350**, 1391-1396, doi:10.1126/science.aaa5004 (2015).

225   Patra, K. C. *et al.* Hexokinase 2 is required for tumor initiation and maintenance and its systemic deletion is therapeutic in mouse models of cancer. *Cancer Cell* **24**, 213-228, doi:10.1016/j.ccr.2013.06.014 (2013).

226   Hosios, A. M. *et al.* Amino Acids Rather than Glucose Account for the Majority of Cell Mass in Proliferating Mammalian Cells. *Dev Cell* **36**, 540-549, doi:10.1016/j.devcel.2016.02.012 (2016).

227   Faubert, B. *et al.* Lactate Metabolism in Human Lung Tumors. *Cell* **171**, 358-371 e359, doi:10.1016/j.cell.2017.09.019 (2017).

228   Louie, S. M. *et al.* GSTP1 Is a Driver of Triple-Negative Breast Cancer Cell Metabolism and Pathogenicity. *Cell Chem Biol* **23**, 567-578, doi:10.1016/j.chembiol.2016.03.017 (2016).

229   Madhukar, N. S., Warmoes, M. O. & Locasale, J. W. Organization of enzyme concentration across the metabolic network in cancer cells. *PLoS One* **10**, e0117131, doi:10.1371/journal.pone.0117131 (2015).

230   Ponten, F., Jirstrom, K. & Uhlen, M. The Human Protein Atlas--a tool for pathology. *J Pathol* **216**, 387-393, doi:10.1002/path.2440 (2008).

231   Uhlen, M. *et al.* A human protein atlas for normal and cancer tissues based on antibody proteomics. *Mol Cell Proteomics* **4**, 1920-1932, doi:10.1074/mcp.M500279-MCP200 (2005).

232   Pacella, I. *et al.* Fatty acid metabolism complements glycolysis in the selective regulatory T cell expansion during tumor growth. *Proc Natl Acad Sci U S A* **115**, E6546-E6555, doi:10.1073/pnas.1720113115 (2018).

233   Singleton, K. R. *et al.* Melanoma Therapeutic Strategies that Select against Resistance by Exploiting MYC-Driven Evolutionary Convergence. *Cell Rep* **21**, 2796-2812, doi:10.1016/j.celrep.2017.11.022 (2017).

234   Liu, X., Ser, Z., Cluntun, A. A., Mentch, S. J. & Locasale, J. W. A strategy for sensitive, large scale quantitative metabolomics. *J Vis Exp*, doi:10.3791/51358 (2014).

235   DeRisi, J. L., Iyer, V. R. & Brown, P. O. Exploring the metabolic and genetic control of gene expression on a genomic scale. *Science* **278**, 680-686, doi:10.1126/science.278.5338.680 (1997).

236   Girotti, A. W. Mechanisms of lipid peroxidation. *J Free Radic Biol Med* **1**, 87-95, doi:10.1016/0748-5514(85)90011-x (1985).

237   Cheeseman, K. H. Mechanisms and effects of lipid peroxidation. *Mol Aspects Med* **14**, 191-197, doi:10.1016/0098-2997(93)90005-x (1993).

238   Barankiewicz, J. & Cohen, A. Impairment of nucleotide metabolism by iron-chelating deferoxamine. *Biochem Pharmacol* **36**, 2343-2347, doi:10.1016/0006-2952(87)90601-0 (1987).

239   Miotto, G. *et al.* Insight into the mechanism of ferroptosis inhibition by ferrostatin-1. *Redox Biol* **28**, 101328, doi:10.1016/j.redox.2019.101328 (2020).

240   Jitrapakdee, S., Vidal-Puig, A. & Wallace, J. C. Anaplerotic roles of pyruvate carboxylase in mammalian tissues. *Cell Mol Life Sci* **63**, 843-854, doi:10.1007/s00018-005-5410-y (2006).

241   Reid, M. A. *et al.* Serine synthesis through PHGDH coordinates nucleotide levels by maintaining central carbon metabolism. *Nat Commun* **9**, 5442, doi:10.1038/s41467-018-07868-6 (2018).

242   Mao, C. *et al.* DHODH-mediated ferroptosis defence is a targetable vulnerability in cancer. *Nature* **593**, 586-590, doi:10.1038/s41586-021-03539-7 (2021).

243   Tarangelo, A. *et al.* Nucleotide biosynthesis links glutathione metabolism to ferroptosis sensitivity. **5**, e202101157, doi:10.26508/lsa.202101157 %J Life Science Alliance (2022).

244   Lane, A. N. & Fan, T. W. Regulation of mammalian nucleotide metabolism and biosynthesis. *Nucleic Acids Res* **43**, 2466-2485, doi:10.1093/nar/gkv047 (2015).

245   Quijano, C., Trujillo, M., Castro, L. & Trostchansky, A. Interplay between oxidant species and energy metabolism. *Redox Biol* **8**, 28-42, doi:10.1016/j.redox.2015.11.010 (2016).

246   Lushchak, V. I. Glutathione homeostasis and functions: potential targets for medical interventions. *J Amino Acids* **2012**, 736837, doi:10.1155/2012/736837 (2012).

247   DeHart, D. N. *et al.* Opening of voltage dependent anion channels promotes reactive oxygen species generation, mitochondrial dysfunction and cell death in cancer cells. *Biochem Pharmacol* **148**, 155-162, doi:10.1016/j.bcp.2017.12.022 (2018).

248   Wang, H., Liu, C., Zhao, Y. & Gao, G. Mitochondria regulation in ferroptosis. *Eur J Cell Biol* **99**, 151058, doi:10.1016/j.ejcb.2019.151058 (2020).

249   Niu, B. *et al.* Application of glutathione depletion in cancer therapy: Enhanced ROS-based therapy, ferroptosis, and chemotherapy. *Biomaterials* **277**, 121110, doi:10.1016/j.biomaterials.2021.121110 (2021).

250   Ren, J. X., Sun, X., Yan, X. L., Guo, Z. N. & Yang, Y. Ferroptosis in Neurological Diseases. *Front Cell Neurosci* **14**, 218, doi:10.3389/fncel.2020.00218 (2020).

251   Piper, M. D. *et al.* A holidic medium for Drosophila melanogaster. *Nat Methods* **11**, 100-105, doi:10.1038/nmeth.2731 (2014).

252   Piper, M. D. W. *et al.* Matching Dietary Amino Acid Balance to the In Silico-Translated Exome Optimizes Growth and Reproduction without Cost to Lifespan. *Cell Metab* **25**, 1206, doi:10.1016/j.cmet.2017.04.020 (2017).

253   Davis, R. W., Botstein, D., Roth, J. R. & Cold Spring Harbor Laboratory. *Advanced bacterial genetics*. (Cold Spring Harbor Laboratory, 1980).

254   Kodde, I. F., van der Stok, J., Smolenski, R. T. & de Jong, J. W. Metabolic and genetic regulation of cardiac energy substrate preference. *Comp Biochem Physiol A Mol Integr Physiol* **146**, 26-39, doi:10.1016/j.cbpa.2006.09.014 (2007).

255   Audet-Delage, Y. & St-Pierre, J. Food for Growth: Distinct Nutrient Preferences between Primary Tumors and Metastases. *Mol Cell* **81**, 220-222, doi:10.1016/j.molcel.2020.12.044 (2021).

256   Zamboni, N., Fendt, S. M., Ruhl, M. & Sauer, U. (13)C-based metabolic flux analysis. *Nat Protoc* **4**, 878-892, doi:10.1038/nprot.2009.58 (2009).

257   Dai, Z. & Locasale, J. W. Understanding metabolism with flux analysis: From theory to application. *Metab Eng* **43**, 94-102, doi:10.1016/j.ymben.2016.09.005 (2017).

258   Liu, S., Dai, Z., Cooper, D. E., Kirsch, D. G. & Locasale, J. W. Quantitative Analysis of the Physiological Contributions of Glucose to the TCA Cycle. *Cell Metab* **32**, 619-628 e621, doi:10.1016/j.cmet.2020.09.005 (2020).

259   Hui, S. *et al.* Quantitative Fluxomics of Circulating Metabolites. *Cell Metab* **32**, 676-688 e674, doi:10.1016/j.cmet.2020.07.013 (2020).

260   Hui, S. *et al.* Glucose feeds the TCA cycle via circulating lactate. *Nature* **551**, 115-118, doi:10.1038/nature24057 (2017).

261   Liao, C. Y. *et al.* Fat maintenance is a predictor of the murine lifespan response to dietary restriction. *Aging Cell* **10**, 629-639, doi:10.1111/j.1474-9726.2011.00702.x (2011).

262   Mitchell, S. J. *et al.* Effects of Sex, Strain, and Energy Intake on Hallmarks of Aging in Mice. *Cell Metab* **23**, 1093-1112, doi:10.1016/j.cmet.2016.05.027 (2016).

263   Tinsley, F. C., Taicher, G. Z. & Heiman, M. L. Evaluation of a quantitative magnetic resonance method for mouse whole body composition analysis. *Obes Res* **12**, 150-160, doi:10.1038/oby.2004.20 (2004).

Biography

Annamarie E. Allen received her Bachelor of Arts degree in Physiology from the University of Minnesota in May 2016. While there, she performed undergraduate research in the laboratory of Dr. Tom Hays under the supervision of postdoctoral associate Dr. Amanda Neisch, studying axonal transport in *Drosophila melanogaster*. In August 2016, Annamarie joined the Department of Pharmacology and Cancer Biology as a doctoral student in the Pharmacology program at Duke University. In the Spring of 2017, she joined the laboratory of Dr. Jason Locasale, where she worked on cancer metabolism and metabolic physiology.

During her time in Dr. Locasale's laboratory, Annamarie contributed work to several scientific papers including *Serine synthesis through PHGDH coordinates nucleotide levels by maintaining central carbon metabolism* and *Evolved resistance to partial GAPDH inhibition results in loss of the Warburg effect and in a different state of glycolysis*. She also worked to characterize metabolic alterations that occur during ferroptosis, helped write a comprehensive review article, *The Molecular Link from Diet to Cancer Cell Metabolism*, and two commentary articles: *Glucose Metabolism in Cancer: The Saga of Pyruvate Kinase Continues* and *Metabolomics: insights into plant-based diets*. Annamarie received a Predoctoral Fellowship Award (F31) from the NCI-NIH, and participated as a scholar in the NIH-sponsored Pharmacological Sciences Training Program (PSTP) during her first two years of study.